ORNL/TM-2007/41 C/ORNL 0596

CRADA Final Report
for
CRADA Number ORNL 0596

Assessment of Computer Simulation Software and Process Data for High Pressure Die Casting of Magnesium

prepared for:

USCAR/USAMP-AMD Project No. 111 & AMD 112

Structural Cast Magnesium Development

A. S. Sabau, E. C. Hatfield, R. B. Dinwiddie

Materials Science and Technology Division
Oak Ridge National Laboratory
Oak Ridge, TN 37831-6083

K. Kuwana, V. Viti, M.I. Hassan, K. Saito

Department of Mechanical Engineering
151 Ralph G. Anderson Building
University of Kentucky
Lexington, KY 40506

Date Published: September 2007

Table of Contents

ABSTRACT

Computer software for the numerical simulation of solidification and mold filling is an effective design tool for cast structural automotive magnesium components. A review of commercial software capabilities and their validation procedures was conducted. This project addressed five main areas: lubricant degradation, lubricant application, gate atomization, and heat transfer at metal mold interfaces. A test stand for lubricant application was designed. A sensor was used for the direct measurement of heat fluxes during lubricant application and casting solidification in graphite molds. Spray experiments were conducted using commercial die lubricants. The results show that the sensor can be used with confidence for conditions specific to the die lube application. The data on heat flux is suitable for use in High-Pressure Die Casting (HPDC) simulation software.

Severe jet breakup and atomization phenomena are likely to occur due to high gate velocities in HPDC. As a result of gate atomization, droplet flow affects the mold filling pattern, air entrapment, skin formation, and ensuing defects. Warm water analogue dies were designed for obtaining experimental data on mold filling phenomena. Data on break-up jet length, break-up pattern, velocities, and droplet size distribution were obtained experimentally and was used to develop correlations for jet break-up phenomena specific to die casting gate configurations.

STATEMENT OF OBJECTIVES

This project is part of a larger DOE project “Structural Cast Magnesium Development” (SCMD). The objective of the ORNL effort was to investigate areas that lead to enhanced capabilities of commercial software used in High-Pressure Die Casting (HPDC).

The project goals were (a) to assess the commercial software capabilities for HPDC, (b) obtain more accurate experimental data for HPDC, (c) conduct measurements on phenomena that were not adequately considered in simulation software, and (d) perform experimental and computational investigation of mold-filling phenomena.

BENEFITS TO DOE OFFICE’S MISSION

This project addresses DOE mission in the following ways. The SCMD project focused on resolving critical issues that limit the large-scale application of magnesium castings in automotive components. At ORNL, the project activities are focused towards the science of the processing technology necessary for Mg alloys. Expected DOE and U.S. industry benefits will include vehicle mass savings for ground and air transportation, leading to reduction in fuel consumption, emissions, and less dependence on foreign oil. The North American auto industry currently uses approximately 70,000 MT/year of magnesium, which is equivalent to some 3.5 kg per vehicle. The ability to significantly increase magnesium usage will help the auto industry meet future Federal CAFE targets and reduce exposure to CAFE penalties. Health and environmental issues for workers are also reduced during light-metal casting operations when compared to ferrous foundries.

1 Executive Summary

The objective of the tasks at ORNL was to enhance capabilities of commercial software used in High-Pressure Die Casting (HPDC). The activities involved the following subtasks:

- Review of commercial software capabilities and their validation procedures.
- Identify gaps in software capabilities and formulate areas of development.
- Obtain data that can be used for software validation.
- Conduct measurements on phenomena that were not adequately considered in simulation software.
- Experimental and computational investigation of mold-filling related phenomena.

The report is divided into six chapters: Software Review, Thermal Degradation of Die Casting Lubricants, Die Cooling Due to Lubricant Application, Jet Flows in High Pressure Die Casting, and Heat Flux at Metal-Mold Interface During Casting Solidification.

1.1 SOFTWARE REVIEW

Four software companies participated in the program. Their capabilities were reviewed in order to identify areas of development that will help improve the analysis capabilities of the HPDC community. A survey on the validation data used by software developers was conducted. As the die casting process is very transient, with the filling time of tens of milliseconds, it is very difficult to obtain experimental data for model development. The following areas were found to be scarce or of low accuracy (or low time resolution) that limit their use for software development for HPDC process:

(1) lubricant application, and
(2) atomization phenomena near by the gate.
(3) Lack of transient experimental data for model validation

For example, lubricant application effects are taken into account by using a heat transfer coefficient. Atomization phenomena are likely to occur due to high gate velocities in HPDC. Different patterns of mold filling are expected when atomization occur. More accurate data on cooling effects during lubricant application is needed. It was found that experimental data for model validation or development is scarce.

1. 2 THERMAL DEGRADATION OF DIE CASTING LUBRICANTS

Thermal degradation of lubricants is important as the liquid metal comes in direct contact with the lubricant. The lubricant degrades under the effect of the high temperature of the molten metal. Lubricant degradation characteristics are important to the HPDC. For example, if the lubricant decomposes too quickly during mold filling, the decomposition compounds can be carried into the casting cavity, increasing the probabilities for defect formation.

DilucoTM 135, a lubricant used in die casting industry, was used in this study1. Based on the information provided by the manufacturer, this lubricant is formulated with refined oils, natural and synthetic polymers, natural and synthetic waxes, wetting agents and emulsifying agents in order to aid in the mold release process.

The TA Instruments SDT 2960 module was used to perform both the thermogravimetric analysis, TGA, and differential thermal analysis, DTA, at the same time. The TGA/DTA experiments were conducted for heating rates of 5 and 10 ^{o}C/min. It was found that the sample started to volatize at about 250 ^{o}C. The lubricant degraded in five main stages. The first, second, and fourth stages occurred slowly over a temperature range of [250:345], [350:380], and [400:480] ^{o}C, respectively. The third and fifth stages occurred at single temperatures of approximately 390 and 485 ^{o}C, respectively. The amount of volatilization was approximately 20, 2, 30, and 43% for the first, second, third, and fourth stages, respectively. This information helps to identify the percent weight change and correlate the chemical structure, processing, and performance in HPDC.

1.3 DIE COOLING DUE TO LUBRICANT APPLICATION

Lubricants are sprayed in order to cool the dies and facilitate the ejection of the casting. In all previous studies, thermocouples were embedded into the heated plate and the heat transfer coefficients (or heat fluxes) were obtained using inverse heat transfer procedures. Simple, but less accurate, data extrapolation procedures were also used. In this section, a new technique for measuring the heat flux during lubricant application is presented.

In order to reproduce conditions similar to those encountered during lubrication of the dies, a heated plate was employed in this study (Figure 1.1). In order to avoid cumbersome analysis of the data, such as performing inverse heat transfer analysis or accounting for the thermocouple response time, a sensor was used in

[1] The lubricant was kindly provided by Gibbs Die Casting Corp.

this study for the direct measurement of heat flux. In addition to the heat flux data, the sensor provides data on the surface temperature.

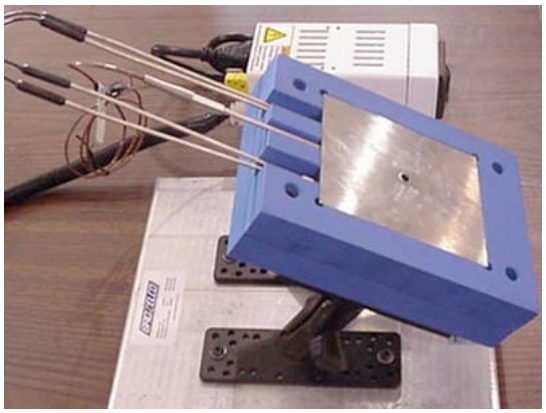

Figure 1.1 The test plate and temperature controller for lubricant application.

Lubricant spray experiments were conducted for different initial plate temperatures. The heat flux data shown in this study reproduced the expected temperature variation for water spray, validating the use of these sensors for the direct measurement of heat fluxes. The evolution of the heat flux and pictures taken using a high-speed infrared camera for static sprays revealed that lubricant application was a transient process. Pictures of the spray cone and lubricant flow on the die were also used to explain the heat flux evolution. It was concluded that the heat flux sensor was a useful tool to obtain heat flux data during lubricant application in the die casting process. The type of data obtained in this study can be used in the development of new lubricants and the selection of appropriate lubricant application techniques.

1.4 JET FLOWS IN HIGH PRESSURE DIE CASTING

Due to the high pressure, the liquid metal enters into the mold at high velocities. The liquid metal comes out through a slit-like opening into the die cavity (10 to 1 aspect ratio) and it is believed to undergo severe break-up and even atomize. These phenomena give rise to fragmented flows during mold filling, such as droplet-like flows, which are believed to yield inherent porosity defects and typical skin microstructures in HPDC. In collaboration with ORNL staff, both experimental and computational studies were conducted at the University of Kentucky on jet flows during the HPDC of magnesium alloys. The goals of this task were to (1) experimentally obtain the velocity distribution and, if applicable, the size distributions of atomized droplets, (2) examine the mold filling pattern using transparent dies, and (3) attempt to develop a computational model that can predict the jet break-up and atomization processes.

Since it is difficult to perform experiments with molten magnesium, an analog liquid was sought for conducting experiments. A scale analysis showed that the fluid dynamics in HPDC are governed by Weber number, We, and Reynolds

number, Re. The Weber number relates the dissipative effect of the surface tension to the de-stabilizing aerodynamic forces, while the Reynolds number relates the inertial to the viscous forces. Thirty two liquids were screened for the given gate conditions. The scale analysis indicated that warm water was the best candidate for the analogue liquid.

The flow visualization systems available at UKY-Lexington were used to characterize the jet flow through gates used in die casting processes. First, open die experiments were conducted in order to investigate the flow pattern, such as jet breakup and atomization, as the liquid exits the gate. The Phase Doppler Particle Analyzer (PDPA) and Particle image velocimetry (PIV) were used to measure the particle size and velocity of the liquid analogue at different distances from the gate (Figure 1.2). The data from open die experiments was used to develop correlation for jet break-up and atomization.

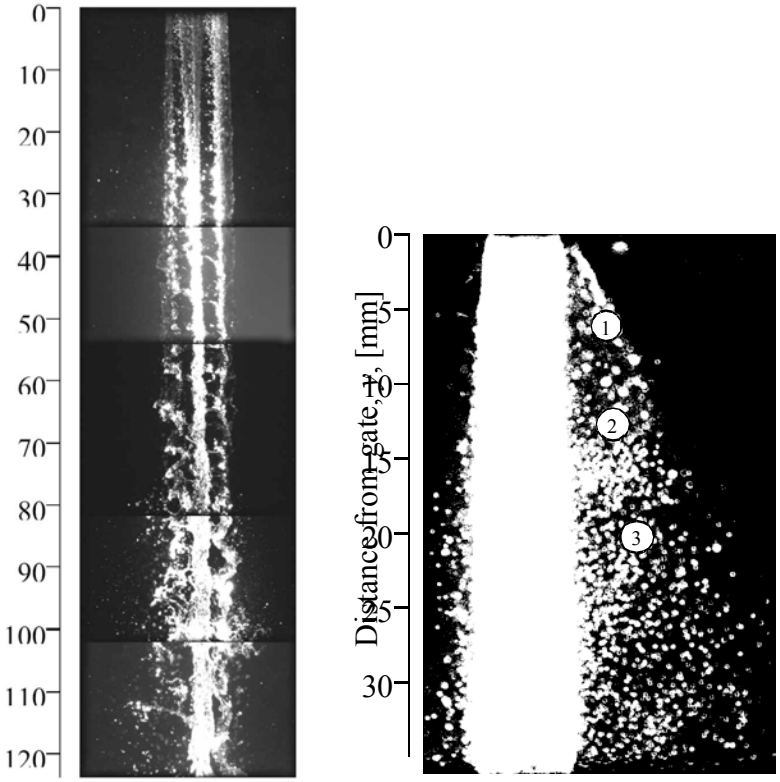

Figure 1.2 Acquired images of a typcal jet using the PIV system; (b) the locations of PDPA are marked with circles. (0 indicates the gate placement)

Numerical simulations were performed using the commercial CFD package Fluent™ since it includes fluid-gas interaction and droplet atomization features, such as Reitz model. The Reitz atomization model, which was developed for combustion applications, was used to simulate possible atomization effects. In the Eulerian approach, both the air and molten metal are modeled on a fixed grid, and Volume of Fluid (VOF) techniques are used to track the interface between

the two materials. A subgrid model was developed for the VOF methodologies based on open die experiments. The subgrid model was implemented in Fluent™. This approach was developed in order to enable mold filling simulations on coarse grids and still be able to predict the small-scale atomization process.

1. 5 HEAT FLUX AT METAL-MOLD INTERFACE DURING CASTING SOLIDIFICATION

The heat capacity of the mold material and thermal resistance at mold surfaces affect the alloy solidification and ensuing microstructure. The computational analysis of heat transfer and solidification of casting processes depends on materials properties, process parameters, and the heat transfer conductance between metal and mold (Ho and Pehlke, 1983). The interfacial heat transfer during solidification is usually quantified in terms of a heat transfer coefficient (HTC). All previous studies on interfacial heat transfer coefficients have been based on indirect methods for estimating the heat flux that employed either inverse heat transfer analysis procedures or instrumentation arrangements to measure temperatures and displacements near the metal-mold interface.

In this chapter, the heat transfer at the metal-mold interfaces was investigated using a sensor for the direct measurement of heat flux. The heat flux sensor (HFS) was rated for 700^{o}C and had a time response of less than 10 ms. Casting experiments were conducted using graphite molds for aluminum alloy A356 (Figure1.3). Several casting experiments were performed using a graphite coating and a boron nitride coating. The measurement errors were estimated. The temperature of the mold surface was provided by the HFS while the temperature of the casting surface was measured using a thermocouple. Results for the heat transfer coefficients were obtained based on measured heat flux and temperatures.

The use of a sensor for the direct measurement of heat flux and surface temperature was demonstrated for casting solidification. The heat flux data was used to obtain the heat transfer coefficient (HTC) at metal-mold interface. It was found that the HTC was determined very efficiently using a heat flux sensor and one additional thermocouple, avoiding cumbersome data post-processing and instrumentation arrangements. The variation of heat transfer coefficient agrees well with data from previous studies.

(a) 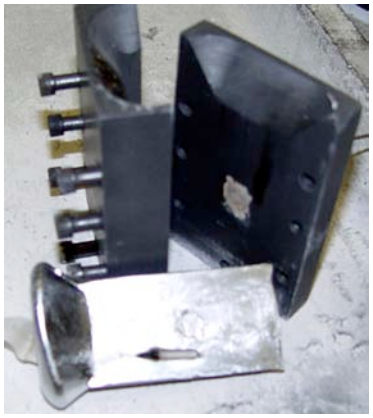 (b) 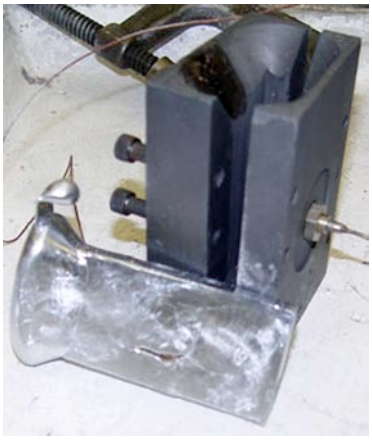 (c)

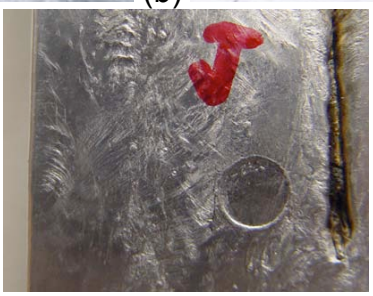

Figure 1.3 Pictures showing (a) and (b) casting, graphite mold, thermocouple at casting interface, and heat flux sensor; (c) the impression of the sensor surface on the casting and thermocouple placement at casting surface.

2 Software Review

ABSTRACT

Four software companies participated in this program. Their capabilities were reviewed in order to identify areas of development that would help improve the analysis capabilities of the HPDC community. A survey on the validation data used by software developers was conducted. As the die casting process is very transient, with the filling time of tens of milliseconds, it is very difficult to obtain experimental data for model development.

The following areas were found to be incomplete studies: lubricant application, atomization phenomena near by the gate, and lack of transient experimental data for model validation. For these areas, the experimental data was either of low accuracy or low time resolution that limits their use for software development for HPDC process. For example, lubricant application effects are taken into account by using a heat transfer coefficient. Atomization phenomena are likely to occur due to high gate velocities in HPDC. Different patterns of mold filling are expected when atomization occur. More accurate data on cooling effects during lubricant application is needed. It was found that experimental data for model validation or development is scarce.

2.1 SOFTWARE VALIDATION FOR HPDC

In developing computer simulation software for HPDC, the following steps are considered:

1. data is acquired for material properties,
2. constitutive equations are formulated for material properties,
3. data is acquired on temperature, microstructure, and fluid dynamics,
4. mathematical models are developed for fluid dynamics, heat transfer, and solidification phenomena

Thus, the simulation software would have the capabilities to model phenomena for which experimental data was acquired. Also, the accuracy of mold filling, solidification, and heat transfer would be at most that of the experimental data. A review has been conducted on measurements conducted for obtaining validation data or process information (Table 2.1).

Table 2.1 Measurement conducted for obtaining validation data or process information.

Measurement/ Validation data	Information	Notes	References
Short shots	Metal distribution at a given time	not reproducible if steady state has not reached if steady state is achieved, short shots could be useful less metal or piston stopped	Righi et al., 95 Flow Science, 2002 Flow Science, 2003
Water in transparent dies	Fluid flow	Solidification not included; Surface tension effects not well represented	Schuhmann et al., 2000
Thermocouple	Thermal conditions	Hard to use due to uncertainty of heat transfer coefficients; poor time response	
Solidification time	Thermal model	Qualitative parameter	
X-ray	Porosity	Quantitative parameter for end product. Information hard to use since it does not point to a specific problem i.e., heat transfer, solidification, filling, atomization, or gas entrapment.	
melt pressure at die surface	Gate freezing	Metal pressure at die surface; Not used yet for software validation	Hu, 2000, Hu et al. 2000; Tong et al., 2002
Direct imaging of lubricant-metal	Lubricant-metal interaction	Investigation on physical processes that lubricant undergo during casting	Kimura et al. (2002) for powder lubricants
IR camera pictures	Temperature distribution on the open die	Die temperature	
Air Pressure	Air flow	Proposed monitoring the back air pressure during casting	N/A
Air Flow Rate	Air flow through vents	Proposed for current program	N/A
Humidity		Considered at Gibbs, Inc.	N/A
Gas composition	Nature of gases in die cavity	Proposed for current program	N/A

As die casting process is very transient, with the filling time of tens of milliseconds, it is very hard to obtain good experimental data for model validation. Each of the measurements conducted to support, guide, and validate software has its own limitations. Short shots experiments are conducted by either injected less metal into the die or stopping the piston before reaches full displacement. This type of test would provide accurate information on mold filling provided that the die has previously warmed up, attaining its steady state. Water models are useful to study the fluid flow without including solidification effects. Further limitations are due to different viscosity and surface tension than those of the alloys. Insight in solidification can be gained by metallographic analysis, from which dendrite cell spacing can be measured and subsequently solidification time can be obtained. X-ray of parts provides useful defect information. However, the information obtained may be hard to use since it does not point to a specific problem i.e., heat transfer, solidification, filling, gate atomization, or gas entrapment.

2.2 SOFTWARE CAPABILITIES AND AREAS OF DEVELOPMENT FOR SOFTWARE ENHANCEMENT

Four software companies participate in the program. Their capabilities are shown in Table 2.2 along with the data used for model validation. With the exception of DieCAS, all the other software companies use fully 3D elements for the meshing the casting part. In DieCAS, the cavity in the die is represented as a shell. This shell approximation allows faster computations than any of the other software. However, the shell approximation is not appropriate for all die casting parts, being suitable for die casting parts of thin sections. It is very important to realize the each software was developed based on certain validation data.

Table 2.2 Validation data used by participant software vendors.

Software	Capabilities relevant to die-casting				Validation data used
	Geometry	Metal flow in Shot Sleeve	Air Flow	Porosity and Air Entrapment in metal	
DieCAS Powercast	Die cavity - shell	Available in Powercast	Vents, Vacuum	Shrinkage porosity from thermal results and gas porosity from filling analysis	Temperature sensors Average casting ejection temperature, die temperature, cooling line energy, dimensions
EKK	3D Unstructured FEM	Moving shot sleeve	Vents, Vacuum, Parting line	Yes	X-ray, Porosity in casting sections
Flow3D	Fractional Volume	Moving shot sleeve	Vents, Vacuum	Yes	X-ray, Short shots, Water in transparent dies
ProCAST	3D Unstructured FEM	Moving shot sleeve	Vents, Vacuum	Yes	X-ray, Surface inspection of flow traces at part surface

The following areas are not as mature in their software implementations as those capabilities shown in Table 2.1:

(1) lubricant application, and
(2) atomization phenomena near by the gate.

For example, lubricant application effects are taken into account by using a heat transfer coefficient. Atomization phenomena are likely to occur due to high gate velocities in HPDC. Different patterns of mold filling are expected when atomization occur. The inclusion of atomization phenomena using Volume of Fluid (VOF) method, would be very expensive computationally since due to small scale of atomized droplets, a very refined mesh has to be used. More accurate data on cooling effects during lubricant application is needed.

There are other process parameters that are not being considered in current software (Table 2.3).

Table 2.3 Process features not considered by current software vendors.

Software	Other process features					
	Lubricant properties	Lubricant application	Lubricant insulation	Gas Humidity	Gas Composition	Atomization
DieCAS						
EKK						
Flow3D						
ProCAST						

In order to enhance computer software for die casting, accurate experimental data must be gathered for guiding the software development and new phenomena must be incorporated into the software. By reviewing the software capabilities and their validation data, the following areas of development deal were identified:

- Use of pressure transducers to obtain data on melt pressure at die surface.
- Study of atomization phenomena.
- Measure humidity, gas composition, gas flow rate, and gas pressure at vent locations.
- Obtain data on die cooling during lubricant application.

2.2.1 Recommendation for Future Work

Based on the assessment of measurement types that can be conducted for die casting processes the following steps are being considered for obtaining experimental data for software model validation. The tasks will include obtaining new data on phenomena already considered in software or data on new phenomena not considered in the simulation software, such as measurement of air flow through vents and pressure measurement in the vent cavity. This type of data will aid in advancing the software models by providing new data on phenomena considered. Data on new phenomena will be used to account in forthcoming models for new phenomena. Possible sequence of tasks could include the following:

1). Experimental program to obtain typical validation data
1.1 obtain temperature data from thermocouple placed in the die
1.2 obtain die temperature from IR camera images of an open die.
1.3 two or three short shots, each after 10 cycles so that the die will have the same temperature and insure repeatability.
1.4 obtain X-ray data for two or three castings, in order to assess repeatability of porosity distribution.

2). Experimental program to obtain data new validation on phenomena considered in software models.
2.1 measurement of air flow through vents
2.2 pressure measurement in the vent cavity, air flow rate through the vents.
2.3 pressure measurement at the die cavity surface.

3). Experimental program to obtain data on new phenomena not considered in software models.

3.1 Humidity using gauges in the vents and gas composition that comes out through the vents
3.2 Lubricant insulation effects based on its properties, method of application, and die temperature.
3.3 Obtain visual data on jet atomization (droplet size, droplet flow) using a quartz window or other experimental setup.

2.3 REFERENCES

Banghong, H., 2000, “Development of a core Magnesium Die Casting Technology for Thin Wall Electronic Hardware Components,” Technical Report to Singapore Institute of Manufacturing Technology.

Flow Science, Inc., "Simulation Overcomes Challenges of Magnesium Diecasting", Foundry Management and Technology, October 2002, pp 13-15

Flow Science, Inc., "Flow-3D Provides Solutions for Tough Casting Problems,” Modern Casting, February 2003, pp. 47.

Hu BH, K K Tong, Niu Xiaoping, Y J Huang, Choy Chee Mun, Ian Pinwill “Development of Magnesium Casting Technology for Ultra-thin Walled Telecommunication Parts,” September, 2000, DIE Casting 2000

Hu BH, Tong KK, Niu XP, Pinwill I, “Design and optimisation of runner and gating systems for the die casting of thin-walled magnesium telecommunication parts through numerical simulation,” J MATER PROCESS TECH 105 (1-2): 128-133 SEP 7 2000

R. Kimura, M. Yoshida, G. Sasaki, J. Pan, H. Fukunaga, 2002, “Characterization of heat insulating and lubricating ability of powder lubricants for clean and high quality die casting,” Journal of Materials Processing Technology, Vol. 130-131, 289-293.

J. Righi, A. F. LaCamera, S. A. Jones, W. G. Truckner, T. N. Rouns, "Integration of Experience and Simulation Based Understanding in the Die Design Process," North American Die Casting Association, 1995, paper 23, pp. 41-52.

Schuhmann, R., Carrig, J, Nguyen, T., and Dahle, A. 2000, “Comparison of Water Analogue Modelling and Numerical simulation Using Real-Time X-Ray Flow data in Gravity Die Casting”, Paper 22, Australasian Die Casting Association, September 3-6, Melbourne, Australia.

Shawn Mahaney, Chung-Whee Kirn, 1999, “Reduction of Manpower in High-Accuracy Finite Element Die Casting Process Simulation,” Presented at the North American Die Casting Association, November 1-4, Cleveland, Ohio.

K. K. S. Tong, B. H. Hu, X. P. Niu and I. Pinwill, “Cavity pressure measurements and process monitoring for magnesium die casting of a thin-wall hand-phone component to improve quality,” JOURNAL OF MATERIALS PROCESSING TECHNOLOGY, 127 (2): 238-241 SEP 30 2002

3 Thermal Degradation of Die Casting Lubricants

ABSTRACT

The liquid metal comes in direct contact with lubricant. The lubricant degrades under the effect of the high temperature of the molten metal. Lubricant degradation characteristics are important to the HPDC. For example, if the lubricant decomposes too quickly during mold filling, the decomposition compounds can be carried into the casting cavity, increasing the probabilities for defect formation. Diluco^{TM} 135, a lubricant used in die casting industry, was used in this study. The TA Instruments SDT 2960 module was used to perform both the thermogravimetric analysis TGA and differential thermal analysis DTA at the same time.

The TGA/DTA experiments were conducted for heating rates of 5 and 10 ^{o}C/min. It was found that the sample started to volatize at about 250 ^{o}C. The lubricant degraded in five main stages. The first, second, and fourth stages occurred slowly over a temperature range of [250:345], [350:380], and [400:480] ^{o}C, respectively. The third and fifth stages occurred at single temperatures of approximately 390 and 485 ^{o}C, respectively. The amount of volatilization was approximately 20, 2, 30, and 43% for the first, second, third, and fourth stages, respectively.

3.1 INSTRUMENTS AND EXPERIMENTAL PROCEDURES

Klein and Bauer (1996) investigated the processes that take place during die casting with regard to the lubricant. Lubricants have the following roles:

- build a separation and lubrication layer between casting and mold that aids releasing the casting,
- insulate the molten metal
- protect the die from oxidation
- cool the wetted form areas via evaporation of the solvent water in between the shots.

Thickness of the lubricant film is an important parameter and could be determined by the lubricant application parameters, such as:

- spraying pressure and impact velocity of the spray,
- adhesion ability or wash-off effects,
- flow rates of cooling water and air.

Kimura et al. (2002) report direct observations of powder lubricants and molten alloys using high-speed video camera through transparent quartz glass. However, the insulating effect was evaluated for casting conditions that are very different from those in die casting processes.

Garrow and Mobley presented one of the most recent study on lubricant properties and assessment of die lubricant performance. Thermogravimetry Analysis (TGA) was used to measures weight percent of material that combusts or volatilizes as a function of temperature. Differential Scanning Calorimetry (DSC) to measure Specific Heat Capacity. Lubricant testing apparatus (LTA) consisting in a heated die and a spray nozzle. LTA was used to measure the cooling properties of the spray during lubricant applications and estimate the heat transfer coefficient based on thermocouple data.

The thermogravimetric analysis (TGA) is used to measure the weight loss of a material from a simple process such as drying, or from more complex chemical reactions that liberate gases, such as structural decomposition, carbonate decomposition, and sulfur oxidation. The TGA also measures the weight gain of a material from a simple process such as re-hydration, or from more complex surface reactions from gas atmospheres. The differential thermal analysis (DTA) identifies the temperature regions and the magnitude of critical events during a drying or firing process such as drying, binder burnout, carbon oxidation, sulfur oxidation, structural clay collapse, cristobalite transitions, alpha-beta quartz transitions, carbonate decompositions, recrystallizations and melting.

The TA Instruments SDT 2960 module performs both TGA and DTA at the same time. This unit measures the amount and rate of weight change in a material, either as a function of increasing temperature, or isothermally as a function of time, in a controlled atmosphere. It can be used to characterize any material that exhibits a weight change and to detect phase changes due to decomposition, oxidation or dehydration. This information helps to identify the percent weight change and correlate chemical structure, processing, and end-use performance.

3.2 ANALYSIS OF LUBRICANT DEGRADATION

Diluco^{TM} 135, a lubricant used in die casting industry, was used in this study[1]. Based on the information provided by the manufacturer, this lubricant is formulated with refined oils, natural and synthetic polymers, natural and synthetic waxes, wetting agents and emulsifying agents in order to aid in the mold release process. The samples have been dried out before TGA/DTA measurements have been performed. The measurements were performed in an air atmosphere. The TGA/DTA experiments are shown in Figures 3.1 and 3.2 for a heating rate of 5 and 10 ^{o}C/min, respectively.

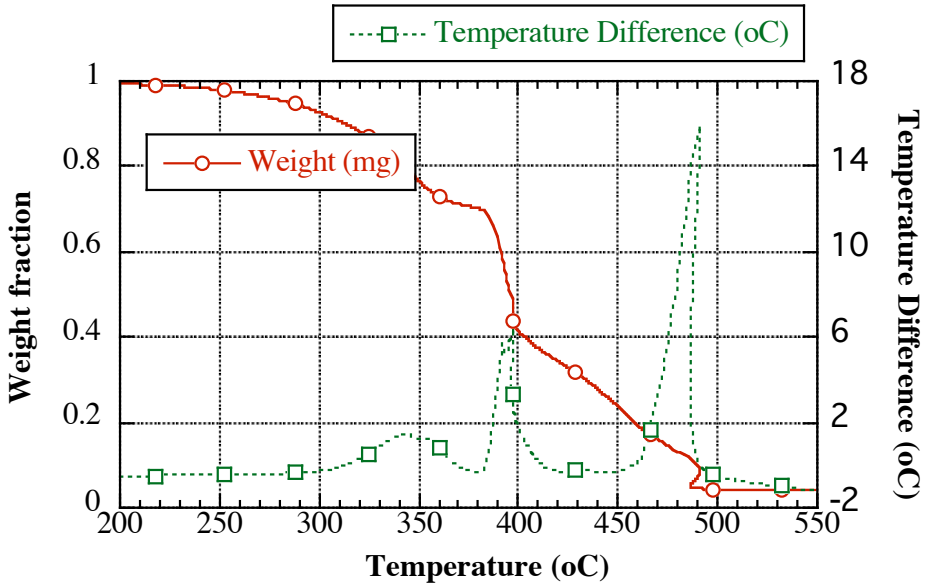

Figure 3.1 TGA (solid line) and DTA (dotted line) data for Diluco 135 for a heating rate of 5^{o}C/min.

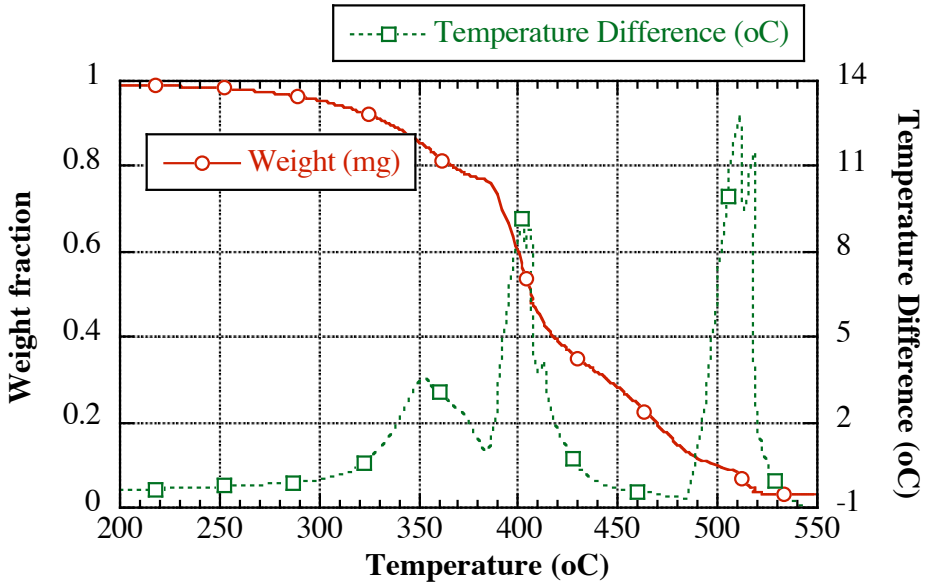

Figure 3.**2** TGA (solid line) and DTA (dotted line) data for Diluco 135 for a heating rate of 10oC/min.

[1] The lubricant was kindly provided by Gibbs Die Casting Corp., one of the project participant.

The TGA measures the change in mass of a sample as a function of temperature and time. Physical changes that do not involve a change in mass but do involve a change in energy, such as a phase change, are captured in the DTA curve. In order to assess if there are such phenomena, DTG, (i.e., -dw/dt) data were constructed. The transition points identified from DTA and DTG are the identical. Since DTA and DTG show the same transitions, then DTA signals was used to characterize the degradation of the lubricant.

The sample started to volatize at about 250ºC. The lubricant degraded in three main stages at temperatures around 345, 390, and 485ºC. In the first and third transitions, the lubricant degraded slowly. In the first and second stages, about 30 and 40-50% of lubricant volatilized. The second transition was the fastest among all three. The data shows that at least 70% of the lubricant was not decomposed below 380ºC, indicating that there should be enough lubricant left on the die before the molten metal is injected into the die.

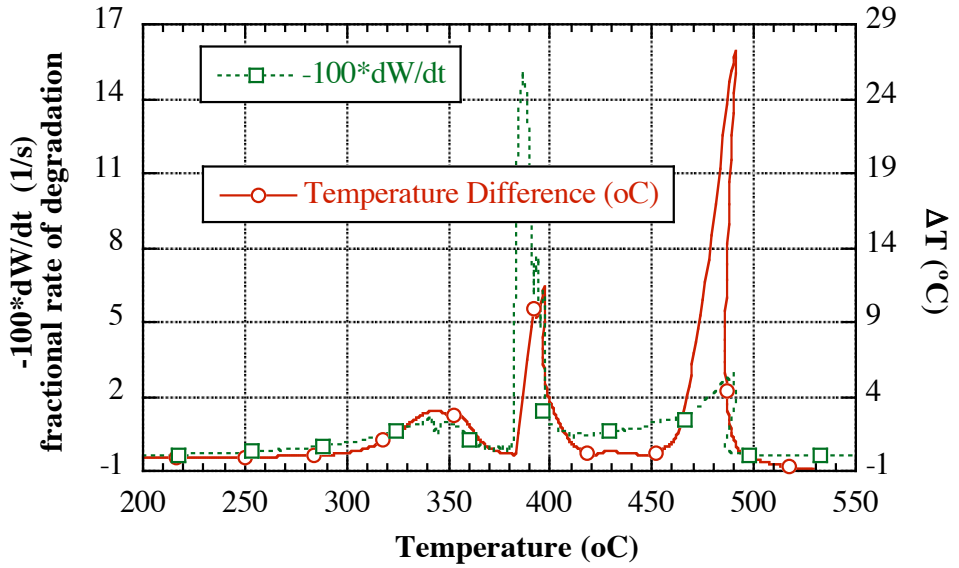

Figure 3.3 DTG (dotted line) and DTA (solid line) results for a heating rate of 5°C/min.

The lubricant is applied in the die casting process by spraying the diluted lubricant on the die surface. Thus, the lubricant experiences high heating rates during its application on the die and further contact with molten metal. Thus, the kinetics of the degradation events was important for our application. The TGA data was obtained at heating rates of 5, 10, 25, and 50ºC/min. The transition temperatures increase with heating rates. At high heating rates, the TGA curve shows less resolution than those at small heating rates. The results are presented in Figure 3.4. This TGA data at different heating rates can be used to determine the kinetic parameters (Kubicek and Lesko, 1979).

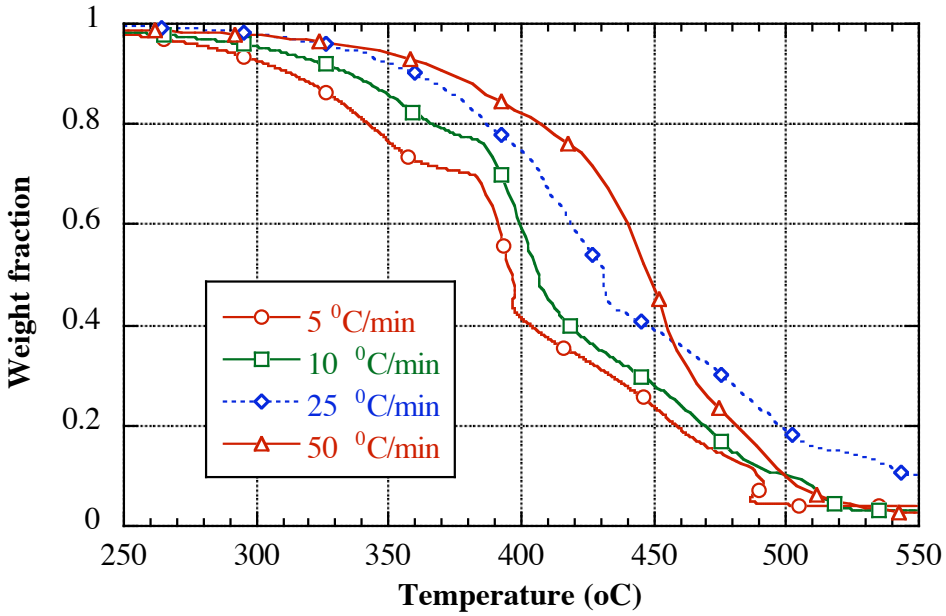

Figure 3.4 TGA data at different heating rates.

3.3 REFERENCES

Banghong, H., 2000, “Development of a core Magnesium Die Casting Technology for Thin Wall Electronic Hardware Components,” Technical Report to Singapore Institute of Manufacturing Technology.

Garrow, DM, and Mobley CE, Characterization of Die Casting Die Lubricants, Student project, Pdf presentation.

R. Kimura, M. Yoshida, G. Sasaki, J. Pan, H. Fukunaga, 2002, “Characterization of heat insulating and lubricating ability of powder lubricants for clean and high quality die casting,” Journal of Materials Processing Technology, Vol. 130-131, 289-293.

Kubicek P, Lesko J, Determination Of The Kinetic-Parameters From Nonisothermal Measurements With A General Temperature Program, Thermochimica Acta, Vol. 31, pp. 21-29, 1979

4 Die cooling due to lubricant application

ABSTRACT

During the die casting process, lubricants are sprayed in order to cool the dies and facilitate the ejection of the casting. In this study, the cooling effects of the die lubricant were investigated using heat flux sensors (HFS) and infrared imaging. Water and lubricant spray application experiments were conducted for the die casting process. The experiments were performed using commercial die lubricants. A first set of experiments was performed with deionized water in order to assess the applicability of the heat flux sensors for die lubrication studies. The evolution of the heat flux and pictures taken using a high-speed infrared camera for static sprays revealed that lubricant application was a transient process. Pictures of the spray cone and lubricant flow on the die were also used to explain the heat flux evolution. The short time response of the HFS allows the monitoring and data acquisition of the surface temperature and heat flux without additional data processing. Then, the lubricant was applied in pulsed, but static manner, by holding the nozzle over the same surface while it was turned on-and-off several times. In the last series of experiments, the lubricant was applied in a sweeping manner, in which the nozzle was moved along the die surface while it was held open. The experiments were conducted at several die temperatures and at several sweep speeds. The heat flux data was presented and discussed. It was concluded that the heat flux sensor was a useful tool to obtain heat flux data during lubricant application in the die casting process. The type of data obtained in this study can be used in the development of new lubricants and the selection of appropriate lubricant application techniques.

4.1 INTRODUCTION

During the die casting process, the dies are sprayed with a lubricant, dies are closed, and liquid metal is injected into the die cavity under high pressures. Net shape parts are produced after subsequent metal solidification and cooling, dies are opened, and parts are ejected. Lubricants facilitate the ejection of the finished product, reduce the soldering effects (Fraser and Jahedi, 1997), and cool the dies (Piskoti et. al., 2003). In order to minimize casting defects, the metal delivery and heating/cooling systems are designed based on the analysis of heat transfer and solidification phenomena. Heat transfer boundary conditions for spray cooling are required for the numerical simulation of the die casting process (Liu et al., 2000). Most of these studies were limited to the spray application technique in which the nozzle was held fixed. Chhabra et al (1993) reported that intermittent spray schedules might improve the lubricant utilization. However, the data for heat flux removed during various lubricant application techniques is almost nonexistent.

In most studies on the lubricant application effects, heated plate systems that mimic the die casting dies were employed and temperature data were obtained using thermocouples that were embedded into the plates (Lee et al., 1989; Garrow, 2001). The heat transfer coefficients (or heat fluxes) were obtained using either simple data extrapolation or inverse heat transfer procedures. In some of these studies, the data were recorded at low frequencies, e.g., only two data points per second were taken in Liu et al (2000). Due to the thermocouple response time, the temperature data could be very different than the actual temperature. However, no analysis that takes into account the thermocouple response time was presented in these studies.

In order to avoid cumbersome analysis of the data, such as performing inverse heat transfer analysis or accounting for the thermocouple response time, a sensor was used for the direct measurement of heat flux (Section 4.3). In addition to the heat flux data, the sensor provided data on the surface temperature, enabling the computation of the heat transfer coefficient. The temperature distribution of the average heat flux for water spray, which was presented by Sabau and Wu (2005), was similar to that for the well-known pool-boiling curve, validating the use of these sensors for the direct measurement of heat fluxes under conditions specific to the die casting process. These results for the water spray are presented in the Section 4.4. During the experiments, the distance between the spray nozzle and plate was held constant. All the experiments were conducted with the same spray flow parameters (i.e. air pressure, air flow rate, water pressure, water flow rate, and water temperature). Numerical simulation results confirmed that the initial abrupt temperature drop is not an artifact but illustrates the thermal shock experienced by the dies during the initial stages of lubricant application. The water spray data are compared with data from other studies in order to assess the accuracy of using a heat flux sensor.

In the next sections, results for several series of spray experiments were presented for the Diluco 135^{TM} lubricant, which was supplied by Cross Chemical Company, Inc. This Diluco lubricant was formulated for magnesium castings. A dilution ratio of 15:1 for the water: lubricant mixture was recommended by the manufacturer. In Section 4.5, results for the Diluco 135^{TM} lubricant are presented for the case in which the nozzle was held in

the same position for the entire spray application. This application was referred to static, or dwell spray technique. Pictures for the lubricant flow patterns were used to explain the distribution of the heat flux at various plate temperatures.

In Section 4.6, infrared imaging was used to provide information on the temperature variation within the spray cone. The region of the spray, which had a higher temperature than the ambient temperature, was referred to as heat affected zone (HAZ). Several pictures taken at the initial stages and at large times were shown and discussed. Although the results are presented for the case in which the nozzle was held in the same position for the entire spray application, the HFS and infrared imaging can be used for other spray application techniques, such as pulsing and sweeping. In Section 4.7, results for the pulse experiments, in which the nozzle was turned on and off, are presented. In Section 4.8, results were presented for the sweep experiments, in which the nozzle was moved across the die surface. In Section 4.9, the results for the average heat flux were compared and discussed for the three application techniques. The lubricant experiments show that the sensor can be successfully used for various lubricant application techniques used in the die casting process. The type of data obtained in this study can be used in the development of new lubricants and the selection of appropriate lubricant application techniques.

4.2 EXPERIMENTAL APPARATUS AND PROCEDURES

In order to reproduce conditions similar to those encountered during lubrication of the dies, a heated plate was employed in this study. The test plate was manufactured from H13 steel, which is a common material used to make dies. The test plate dimensions were 10x13x1.3 cm. Two Watlow GA70-GJ36 300 watt-heating elements and one thermocouple were embedded into the plate. The thermocouple provides feedback data to the power controller. The plate was insulated to reduce the heat loss from it and to ensure that heat was mainly conducted to the spray cooled surface (Liu et. al., 2000). The edges of the test plate were sealed with silicon to prevent water from penetrating the test plate assembly during spray cooling. The controller adjusted the power to the heating element so that the target temperature was reached quickly and it is subsequently held constant. The spray nozzle was placed 190 mm away from the test plate. The nozzle was oriented such that the liquid spray was perpendicular to the center of the plate. The nozzle was held by fixtures to eliminate the heat flux variation due to variability in the nozzle position and orientation.

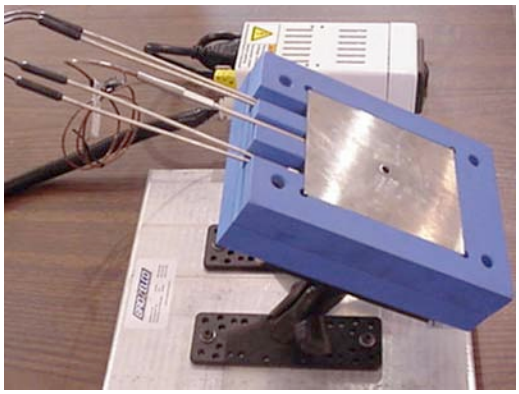

Figure 4.1 The steel test plate (front) and temperature controller (back).

An HFM-8E/H heat flux sensor, which was supplied by the Vatell Corporation, was used to acquire data on heat flux and surface temperature. The heat flux sensor was mounted in the center of the test plate. Information regarding the heat flux sensor was supplied by the manufacturer and is provided in this paragraph (Vatell Corporation, 2004). This sensor is rated for temperatures up to 700°C and has a sensitivity of $150 \pm 10\ \mu\mathrm{V/W/cm^2}$. The heat flux and temperature sensors are thin films deposited by proprietary techniques onto a substrate. The heat flux sensor is a differential thermopile. When heat flows into or out of the substrate surface, a small temperature difference is registered across the resistance elements of the thermopile, and each thermocouple pair produces a voltage proportional to the heat flux. The total voltage across the thermopile is the sum of the voltages in each thermopile, which indicates the direction and magnitude of the heat flux. A separate Type E thermocouple measures the temperature associated with the heat flux. The films that make up the HFM are less than 2 microns thick. Due to the thickness of these films, the response time for this heat flux sensor is approximately 6 microseconds. The sensor thermocouple and differential thermopile was calibrated using NIST traceable equipment. Through calibration, all sensor constants needed to obtain the heat flux (W/m^2) are provided.

A data acquisition provided by Dataq Instruments, Inc. was used to obtain data at a sample rate of 60 Hz. The plate surface temperature was considered to be that measured by the thermocouple in the heat flux sensor since the thermocouple is embedded very close to the surface.

4.3 MEASUREMENT VALIDATION FOR WATER SPRAY

The initial plate temperatures, at which experiments were conducted, were 150°C, 200°C, 250°C, 300°C, 350°C, and 400°C. The test cases were labeled with W#, where # indicate the initial plate temperature. The different runs that were performed for each test case were labeled with the test case notation followed by a letter. For example, the notation W150 refers to all the runs that were conducted at an initial plate temperature of 150°C, while runs W150A and W150B refers to the first and second run for case W150. These initial plate temperatures are representative of the temperature range that are usually experienced by the dies during the die casting process, including the hot spots regions.

The volumetric flow rate of water spray was measured. Liquid flow rate can be adjusted by a dial on the spray gun. The flow rate was determined by weighing the amount of liquid sprayed into a container in a given time. Water was sprayed after the nozzle was placed into the container to eliminate measurement errors due to water splashing out of the container. The average water spray flow rate was found to be 10.5 16.7, and 19.2 cm^3/s for dial positions of 2, 2.5, and 3 respectively. For lubricant spray experiments, the same flow rate as those for water spray experiments were used since the density of the lubricants is almost the same as that for water.

The results shown in Figure 4.2(a) indicate that the heat flux and surface temperature were well reproduced in case W150. This high degree of reproducibility provides confidence in the experimental setup. It was observed that the plate surface temperature dropped by 29°C and heat flux decreased by 350 KW/m^2. Altan et al (1991) indicated that for surface temperatures less than 165°C, only a small amount of liquid boils, and heat removal from the die surface is mainly due to convection. An average heat flux was computed from the original raw data using a smooth curve fit. The average heat flux obtained from the smooth curve fit is shown in Figure 4.2(b) along with the original heat flux evolution. A sharp decrease in surface temperature took place during the first 0.25 seconds after the spray started.

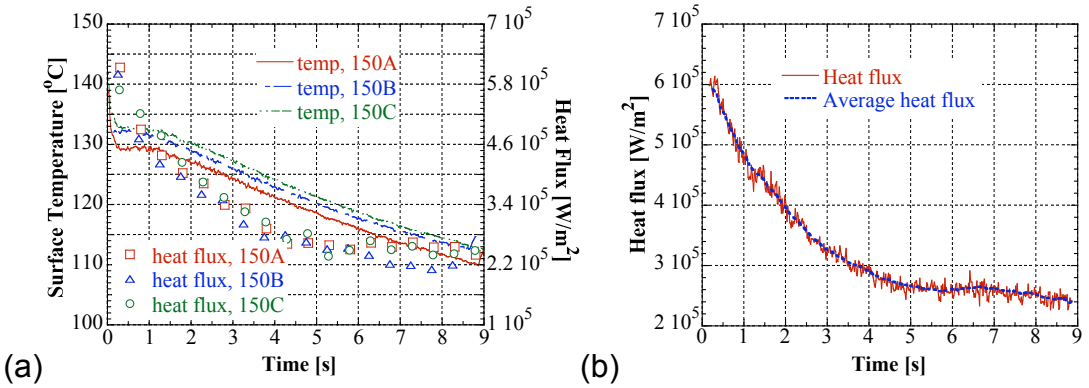

Figure 4.2(a) Evolution of heat flux and surface temperature for case W150. (b) Measured heat flux and average heat flux for run 150A.

Figure 4.3 shows the heat flux and surface temperature evolution for an initial plate temperature of 200°C. The maximum heat flux was approximately 300 KW/m^2 higher than that for case W150. Over the spray duration, the surface temperature of the plate decreased by approximately 45°C. The larger decrease in surface temperature observed for case W200 than that for case W150 is mostly due to more intense boiling of water droplets. Unlike case W150, the initial phase lasted about 2 seconds from the spray onset. The heat flux was almost constant at the maximum value during the period. However, as time proceeded boiling continued, and a vapor layer established over the plate surface and hinders water droplet impingement on the plate surface. Thus, the decrease in heat flux after two seconds of spraying was observed.

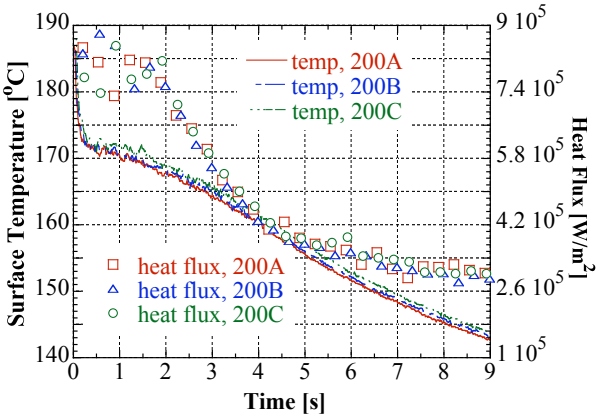

Figure 4.3 Heat flux and surface temperature for case W200.

A 2-dimensional mesh of the H13 steel test plate was created in ProCast™ to perform a numerical simulation of the cooling effects of water on this plate. As shown in Figure 4.4, the initial sharp decrease in the numerical simulation closely matches the sharp decrease due to the thermal boundary layer observed in the plots of the experimental data. Thus, the initial data is not due to an artifact in the experiment but to a thermal shock that the plate experiences due to high heat fluxes.
The temperature profile through the plate thickness is that of a boundary layer for large Biot numbers (Incropera and De Witt, 1981). From the experimental data for spray duration of 0 to 0.2 *s*, the Biot number was on average approximately 1.8.

At approximately 0.05 seconds, the computational surface temperature data started to diverge from the experimental data. This divergence of the computational data from the experimental data is due to the fact that the simulations were performed for the small region on the plate surrounding the sensor. Conducting the simulations for the entire plate system was precluded by the lack of heat flux distribution away from the center of the spray.

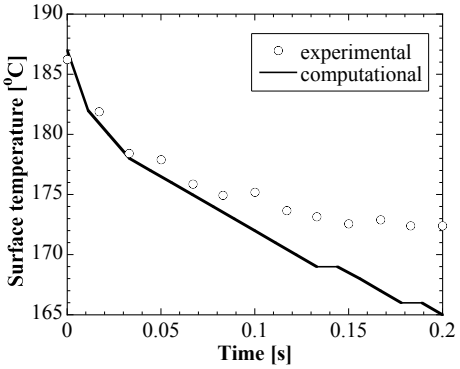

Figure 4.4 Numerical simulation results and experimental results for the evolution of surface temperature in the initial spray stages for an initial plate temperature of 200 ºC.

eWeitt (1981). The heat flux evolution does not show an inflection point as seen in case W200. The absence of this inflection point may be attributed to the fact that for case W250, the plate temperature did not drop to 165°C, where the inflection point occurred for case W200.

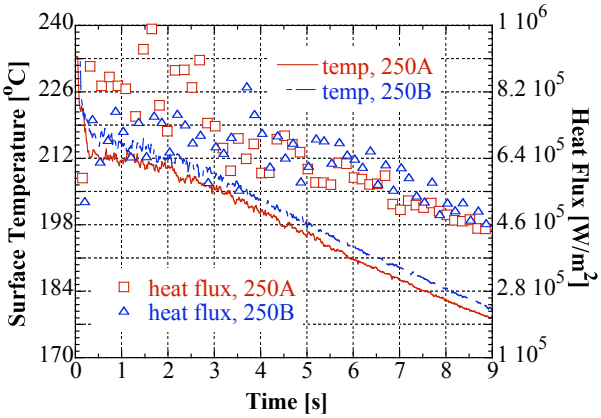

Figure 4.5 Heat flux and surface temperature for case W250.

The heat flux and surface temperature as a function of time for case W300 are shown in Figure 4.6 (a). Unlike cases W150, W200, and W250, the heat flux for case W300 shows a very small decrease from its initial maximum value. Since the evolution of the heat flux for case W300 changes from that of cases W150, W200, and W250, details of the uncertainty analysis performed for this case are also presented. Figure 5b shows a comparison between the average heat flux and the measured data for run 300A. Heat flux and surface temperature evolution behavior similar to those observed in case W300 were noted for cases W350 and W400 as shown in Figures 4.7 and 4.8.

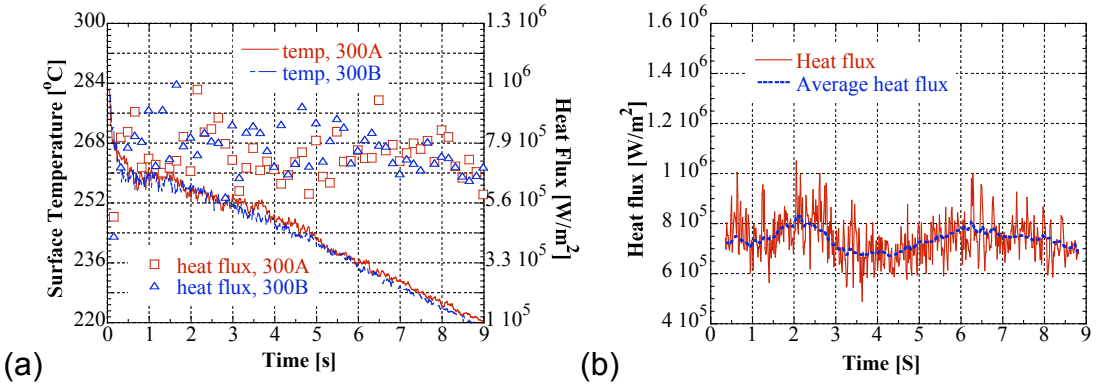

Figure 4.6 (a) Evolution of heat flux and surface temperature for case W300. (b) Measured heat flux and average heat flux for run 300A.

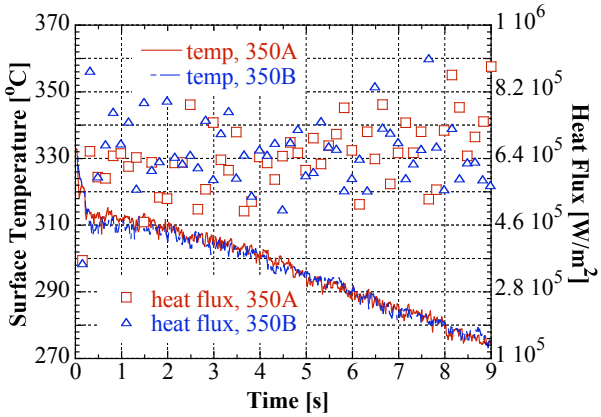

Figure 4.7 Heat flux and surface temperature data for case W350.

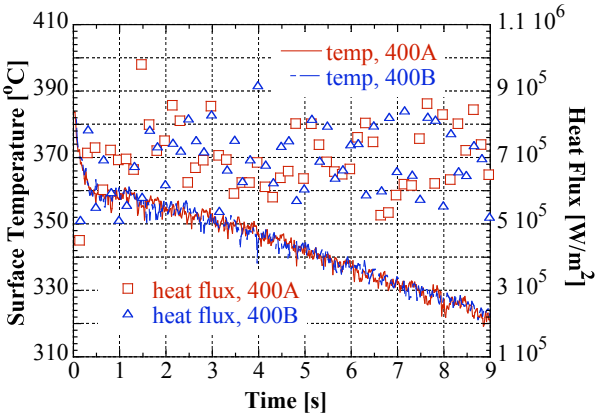

Figure 4.8 Heat flux and surface temperature data for case W400.

In order to quantify uncertainties of the heat flux measurements, standard deviations were estimated from the average heat flux and raw data. In Table 4.1, the standard deviation in percentage for each case is reported.

Table 4.1 Standard deviation of the difference in measured heat flux and average heat flux for each case tested.

Initial Plate Temperature (°C)	Standard Deviation
150	3
200	4
250	7.60
300	10
350	12.60
400	13

An important test for our measurements is to compare the distribution of average heat flux with other data. As shown in many studies, such as the one by Sozbir et al (2003), the temperature distribution of the heat flux for water sprays is similar to that of the well known pool boiling curve. The point of local minimum heat flux on the pool boiling curve, at temperatures higher than the burnout point, indicates the Leidenfrost temperature (Incropera and DeWitt, 1981). At the Leidenfrost point, the plate surface is covered by an insulating vapor blanket, making water impingement on the plate surface limited. As a result, the heat removal rate decreases to a local minimum. Sozbir et al (2003) found that the Leidenfrost temperature for water increases linearly with increasing mass flux. They also found that the Leidenfrost temperature at a fixed water mass flux increases as air velocity is increased. For example, at a mass flux of 6 kg/m^{2}s, Sozbir et al (2003) found that the Leidenfrost points were 515°C, 524°C, and 544°C for air velocities of 24.9m/s, 35.1 m/s, and 45.22 m/s respectively.

Figure 4.9 shows the average heat flux as a function of initial plate temperature. The maximum or critical heat flux occurred at a temperature of 250°C. The temperature distribution of the average heat flux was similar that for the well-known pool-boiling

curve, validating the use of these sensors for the direct measurement of heat fluxes under conditions specific to the die casting process. It is well known that the temperatures at which different pool boiling regimes take place vary with spray conditions (Sozbir et. al., 2003). For this work, the following regimes can be clearly identified: a) nucleated boiling, from 150°C to 250°C, b) transition boiling from 250°C to 350°C, and c) film boiling for temperatures larger than 350°C. At 350°C, the average heat flux reached a local minimum. Although the exact value for the Leidenfrost point is not available, since data was available at 50°C increments, the Leidenfrost point occurs somewhere between 350°C and 400°C.

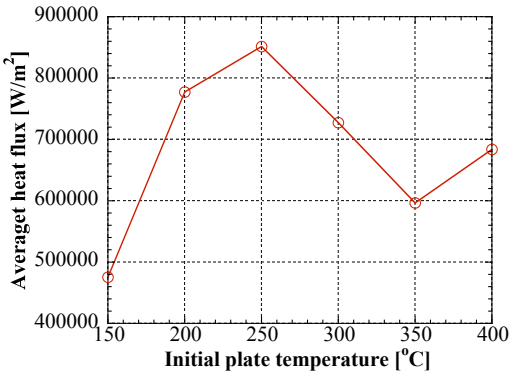

Figure 4.9 Average heat flux data for the first 2 seconds of spray as a function of initial plate temperature.

The data on heat flux can be used for die design (Herman, 1992). One parameter of interest to die casting engineers is the heat transfer coefficient, since most software packages, which are used in the die casting community use heat transfer coefficients as input rather than heat fluxes. The heat transfer coefficient, h, during water spray application is computed using the following equation:

$$h = \frac{q''}{T_s - T_A} \tag{4.1}$$

In the equation above, q'' is the heat flux, T_s and T_A is the surface temperature of the plate and the ambient temperature (25°C) respectively. Figure 4.10 shows the heat transfer coefficient obtained for water at various initial plate temperatures.

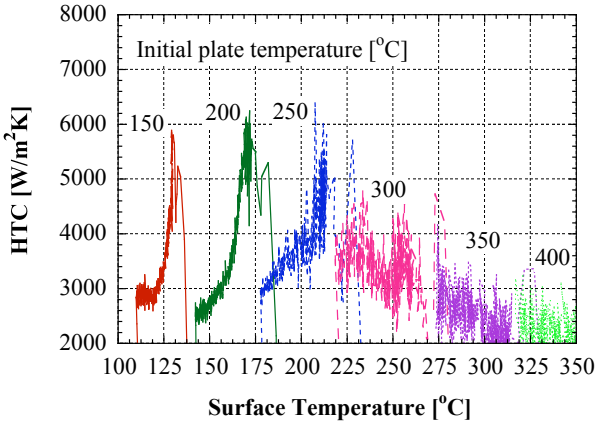

Figure 4.10 Heat transfer coefficient of water as a function of surface temperature for all cases.

4.3.1 Assessment of measurement technique

Measurements of heat flux during lubricant application are presented. A sensor is used for the direct measurement of heat flux. The heat flux data shown in this study reproduces the expected temperature variation for water spray, validating the use of these sensors for the direct measurement of heat fluxes.

4.4 STATIC SPRAY APPLICATION OF LUBRICANT

The initial plate temperatures, at which experiments were conducted, were 150^{o}C, 200^{o}C, 250^{o}C, 300^{o}C, 350^{o}C, and 400^{o}C. The test cases were labeled with L#, where # indicate the initial plate temperature. The different runs that were performed for each test case were labeled with the test case notation followed by a letter. For example, the notation L150 refers to all the runs that were conducted at an initial plate temperature of 150^{o}C, while runs L150A and L150B refers to the first and second run for case L150. Lubricant temperature was 25^{o}C. The lubricant reservoir pressure and air pressure were each set to 0.446 MPa (50 psi). The volumetric flow rate of lubricant spray was the same as that for the water , i.e., the total lubricant spray flow rate was found to be 10.5 cm^3/s. The liquid mass flow rate on the sensing area was not measured since it was not an engineering variable that can be measured easy during the die lubrication process. Most data on fundamental studies on spray cooling are reported as heat flux versus surface temperature. In die casting processes, the lubricant application seldom reaches a uniform steady state, as the lubricant is applied for fractions of second or few seconds. Thus, in this study most of the data is presented as heat flux versus time and surface temperature versus time. The wetting properties of the plate surface and sensor surface are important factors in boiling phenomena. The surface material of the sensor was made of pure nickel. Visual examination of the sensor surfaces and steel surface adjacent to the sensor surface did not reveal any surface effects on spray boiling.

The results shown in Figure 4.11 (a) indicate that the heat flux and surface temperature exhibited a high degree of reproducibility in case L150. It was observed that the plate surface temperature, T_S, decreased by 25^{o}C and heat flux decreased by a half, to almost 250 kW/m^2. The results for the L150 and L200 cases are similar in the features, although the maximum heat flux was approximately 300 kW/m^2 higher than that for case L150.

In the first 0.5s, the temperature dropped to 135 ^{o}C and then rose to 140 ^{o}C. This zigzag variation was observed for all three runs, for both L150 and L200 cases. From 0.5 to 2 s, the temperature exhibited very small variations, as the heat flux continued to decrease. In the last 5s of the spray, there was a low degree of superheat, small amount of liquid boiled, and the heat removal was mainly due to the liquid convection (Altan et al., 1991). The distribution of the heat flux and surface temperature changes for cases L250 and L300 (Figures 4.11 (c) and 4.11 (d). For these cases, the heat flux stayed constant at its maximum value for a relatively larger time. The initial constant heat flux stage lasted for 2.5 and 4s for L250 and L300 cases, respectively. Also, the zigzag variation of T_S, which was a characteristic of L150 and L200, had not been

observed for L250 and L300. Instead, T_S exhibited a sharp and linear decrease in the first 0.5s. Numerical simulation results for the evolution of surface temperature in the initial stage showed that the sudden temperature drop was due to high cooling fluxes (Sabau and Wu, 2005).

In order to gain insight into the differences between the L200 and L300, the patterns for the spray cone and lubricant flow on the die were investigated. Pictures taken for L200 and L300 cases were shown in Figure 4.12 (a) and 4.12 (b), respectively. The following differences can be seen between these two cases:

- lubricant was spread over a larger area for L200 than for L300,
- towards the edge of the spread area, the lubricant fingers were larger for L200 than for L300,
- lubricant fingers were thicker for the L200 than for L300,
- spray cone was continuous from the nozzle to the plate for L200, while it was shaped as mushroom for L300.

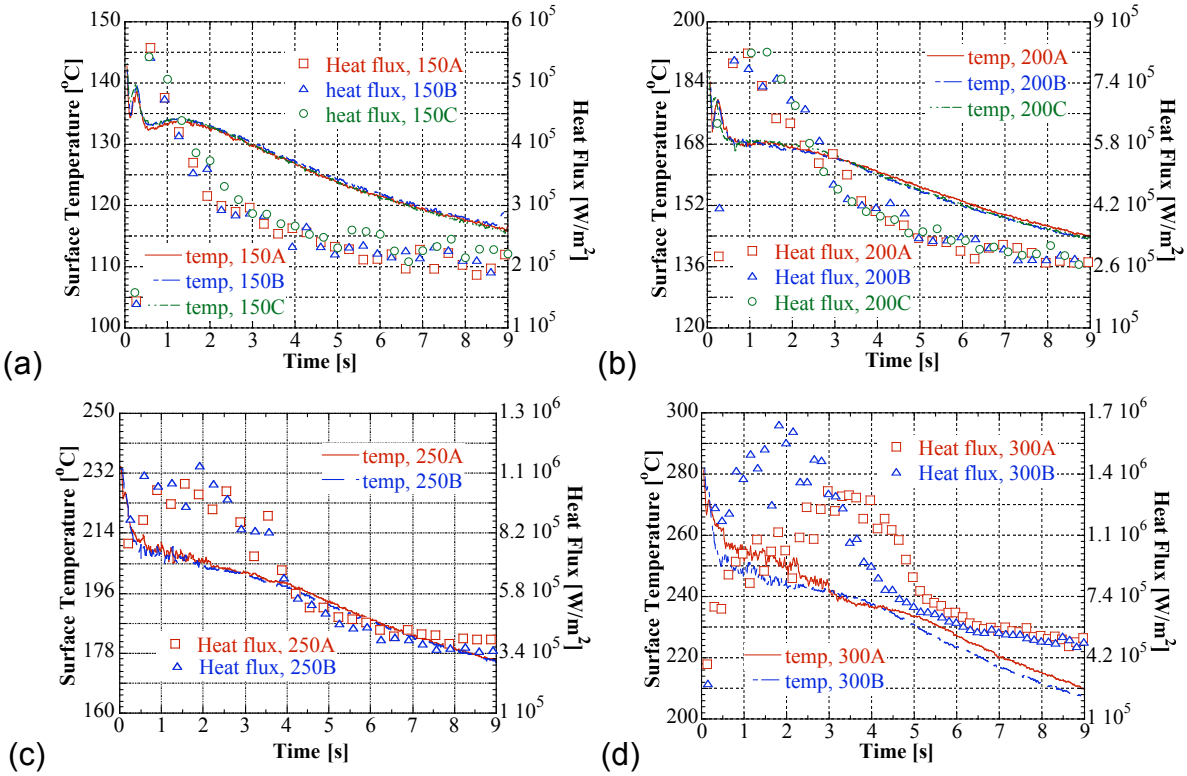

Figure 4.11(a) Evolution of heat flux and surface temperature for cases (a) L150, (b) L200, (c) L250, (d) L300.

The mushroom shape for the L300 spray cone was due to the convection of the vapor away from the plate. The higher rate of vaporization for L300 increased the convection of the vapor, which pushes away the lubricant droplets, hindering droplet impingement on the plate surface. This behavior was transient. Initially, the vapor layer was not established, all the droplets impacted the surface and vaporized upon contact with the heated surface, resulted in the highest heat flux. As the hot vapor layer was built near the plate surface, droplets partially vaporized before reaching the plate. Also, the droplets on outer surface of the spray cone were decelerated and deviated on paths toward the outer surface by the vapor that flowed away from the center region. These

vaporization effects combined with the decrease in surface temperature yield a decrease in the heat flux.

The distribution of the heat flux for cases L350 and L400 was different than those for L250 and L300 (Figures 4.13 (a) and 4.13 (b). For L350 and L400, the maximum heat flux was not recorded in the initial stages but after several seconds. It appeared that the instant of maximum heat flux increased with the plate temperature. Unlike previous cases, for which the maximum heat flux gradually increased from the previous case, for the L400, the maximum heat flux was lower that that for L350. These results indicate that the Leidenfrost temperature for the spray lubricant was larger than 350 ^{o}C.

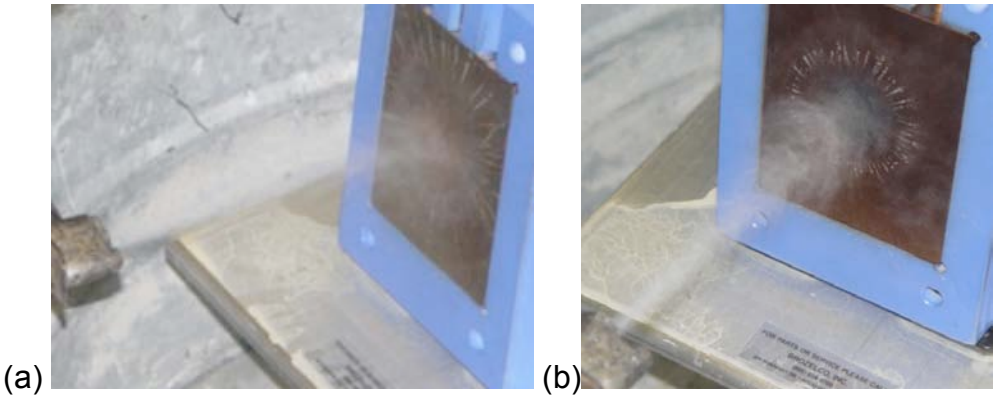

(a) (b)

Figure 4.12 Pictures showing liquid convection on the plate for cases (a) L200 and (b) L300. Water vapors preclude an effective cooling at large times.

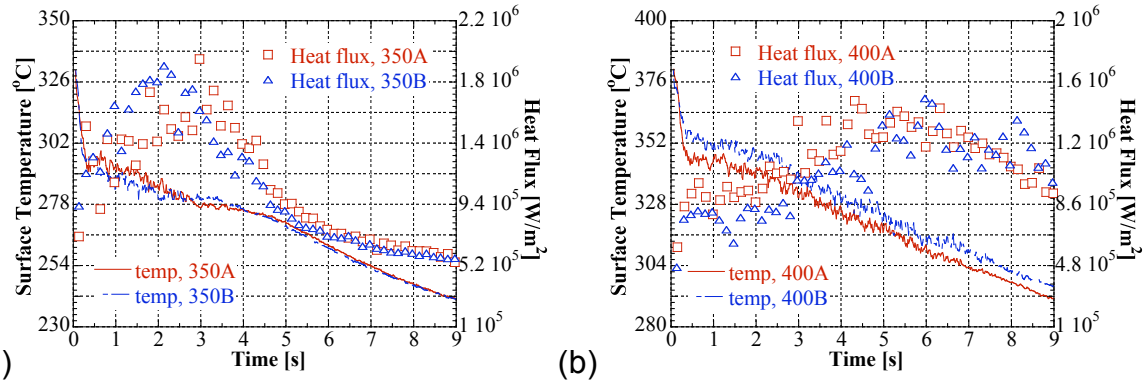

(a) (b)

Figure 4.13(a) Evolution of heat flux and surface temperature for cases (a) L350, (b) L400.

The data on heat flux removed during lubricant application is necessary for die design (Herman, 1992). Most commercial software packages, which are used in the die casting community, use heat transfer coefficients, h, as input rather than heat fluxes, q''. The heat transfer coefficient, *h*, during spray application was computed using the following equation:

$$h = \frac{q''}{T_s - T_A} \qquad (4.1),$$

where T_s and T_A is the surface temperature of the plate and the ambient temperature (25^{o}C) respectively. Figure 4.14 shows the heat transfer coefficient obtained for all cases at various initial plate temperatures. Although the heat flux varied by a relatively large amount for L350 and L150 cases (Figure 4.11(a) and 4.13 (a), the heat transfer coefficient exhibited a lower variation, i.e., $h_{\max}(350) = 1.25\, h_{\max}(150)$.

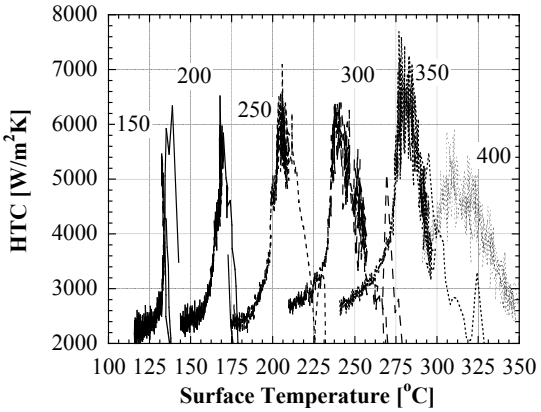

Figure 4.14 Heat transfer coefficient of water as a function of surface temperature for all cases.

4.5 INFRARED VISUALIZATION

In order to gain insight on the spray mechanisms, the temperature distribution of the spray cone was monitored using high-speed infrared camera. Images were acquired using the Amber Radiance-HS Midwave IR camera, with a 256 × 256 InSb focal plane array (FPA) detector. This FPA is sensitive to infrared wavelengths from 3000 to 5000 nm and operates in a snapshot mode where all pixels are sampled at the same time. Snapshot mode is useful in reducing blurring and distortions when imaging fast moving targets or scenes where temperature may be changing rapidly. The camera was equipped with a 50 mm germanium lens. The integration time (exposure time) was set to 1.0 ms. A total of 700 images were acquired at 140 Hz for each experiment. Each set of 700 images is referred to as a sequence and can be thought of as a short movie. No filters were required when the plate surface was set to 150ºC. However, 2 filters were used in series when the plate temperature was set to 300ºC. The filters were standard photographic 80A and cross polarizer filters mounted on the front of the IR lens. In the infrared region these filters basically act as low cost neutral density filters, reducing the overall radiance from the scene. In order to eliminate background clutter, the first image prior to the spray becoming visible was subtracted from the entire sequence. This insures that only the spray cone is visible in the infrared images. Time was set to zero when the spray first hits the plate. The image sequences were colorized, using a consistent color pallet, in order to clearly identify the temperature distribution within the spray cone. This color pallet or color map was set with an IR signal of 0 bit-count being represented by black and the IR signal of 2228 bit-count represented by yellow. Intermediate IR signals were represented by magenta, blue, cyan, green, red, and orange, listed in order on increasing intensity. The IR signal is a relative unitless number which is proportional to the temperature and emissivity of the object being imaged. Other factors that can affect the magnitude of the IR signal (i.e., distance, lens, filters, atmosphere, integration time, background temperature, etc.) were maintained constant, with the exception of filters as discussed above. Changing the filters between the L150 and L300 cases means that, for example, the green region of the L150 case is not the same temperature as the green region of the L300 case. However, when comparing all of the images within the L300 case, all regions represented by a particular color are of the same temperature range. Individual images were selected from each sequence for

comparison. These comparison images were acquired at time = 0.021, 0.057, 0.064, 0.086, 1.86, and 3.8 seconds.

The results obtained by the infrared camera were shown in Figure 4.15 and 4.16 for cases L150 and L300, respectively. The infrared imaging provided information on the relative temperature variation within the spray cone. This spray cone is referred to in the remainder of the paper as heat affected zone (HAZ). By eliminating the pixels with the lowest signal, the air and the spray region that had that lowest temperature were eliminated. The time at which the pictures were taken were shown on each frame. HAZ were inclined since the spray direction was slightly inclined.

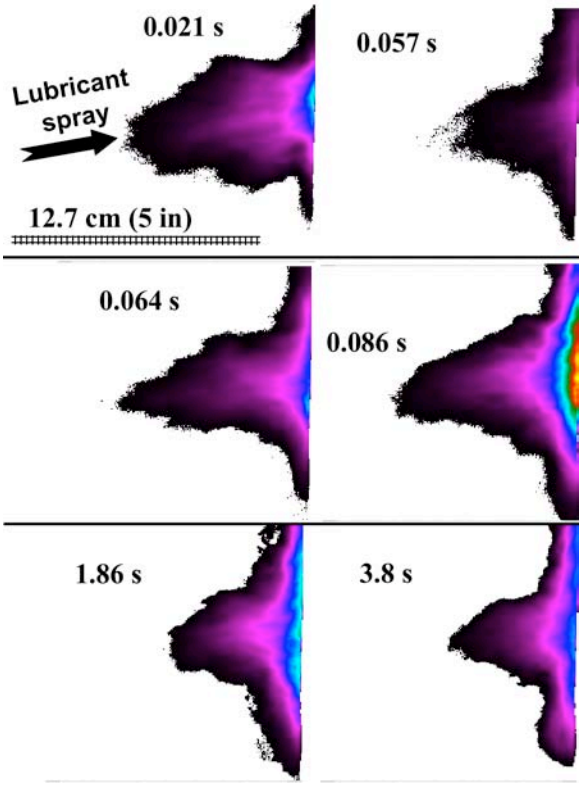

Figure 4. 15 Infrared pictures showing the temperature profile in front of the plate for case L150.

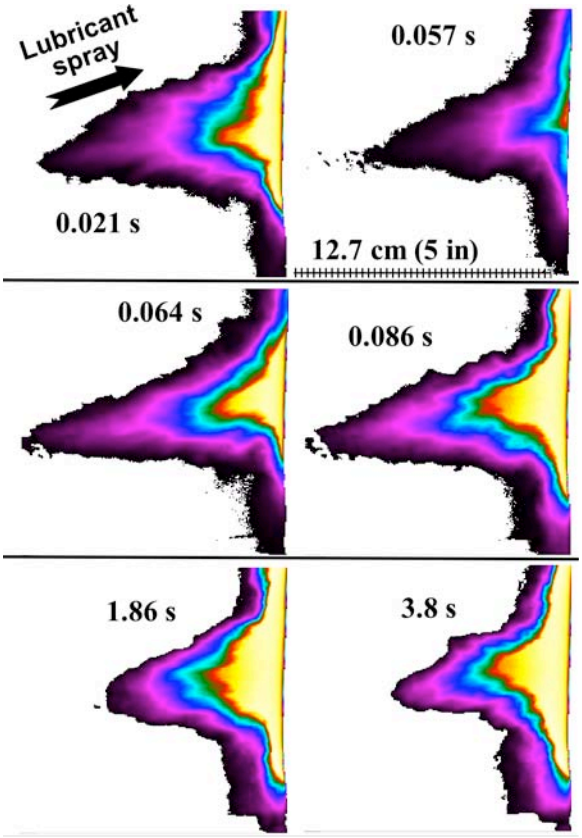

Figure 4.16 Infrared pictures showing the temperature profile in front of the plate for case L300.

For L150 case, the largest HAZ was recorded at 21 ms. The appearance of the largest HAZ at the initial times was consistent to the droplet movement and the convection of the vapors away from the hot plate. Initially, the plate surface had the highest temperature, the vapor blanket would not be established, the droplets would have a higher normal momentum and would get closer to the hot surface, the droplets would vaporize more effective, and the remaining droplets would bounce back with a higher velocity. Droplet bouncing and multiple droplet impact with the hot surface are expected, as showed by the droplet paths in a conical spray (Issa, 2003). For water sprays, a numerical method was presented in Issa (2003) that incorporated models for droplet spreading, droplet evaporation near the surface, pressure effect on the latent heat of vaporization, and multiple impact of the droplet. At 57 ms, the HAZ had a lower height near the plate center, but increased its height more uniformly on the plate surface, as compared to those at 21 ms frame. At 64 and 86 ms, the HAZ had a shape similar to that at 21 ms. At large times, the HAZ decreased in size as evidenced by the frames taken at 1.86 and 3.8 s. This evolution of the HAZ can be explained by considering the data on the surface temperature, data on heat flux, and effect of the vapor blanket that was established near the hot surface. As the spray continues, the surface temperature decreases, the water vapor slowed the incoming spray droplets, less heat was removed from the surface, and less vaporization took place.

For L300 case, HAZ evolution was similar to that for the L150 case. For the L300 case, there was more detail available as the color map was fully used, and the region of high temperature was fully seen near the hot surface. At 57 ms, it was noted that the maximum temperature in the HAZ was lower than that of the hot plate temperature. Although the HAZ had decreased in size, the HAZ of maximum temperature had stayed

the same from 64 ms till 3.8 s. Overall, HAZ was larger for the L300 than for the L150 case. This indicated that a large amount of vapor and droplets with high temperature were present in the L300 case. Thus, it has been demonstrated that Infrared imaging can be used to determine the relative temperature variation within the spray cone.

4.6 PULSE SPRAY APPLICATION OF LUBRICANT

The vapor barrier, which usually establishes in front of the die surface due to water vaporization or lubricant degradation, precludes an efficient deposition of lubricant on the die surface in the later stages of the spray. Several techniques have been proposed to overcome this effect. It was suggested that applying the spray in pulses by turning the nozzle on and off, or in sweeps by moving the nozzle across the die surface, would be more effective in lubricant application (Herman, 2003). It was believed that by stopping the spray after it was applied for a short period of time, the steam barrier would dissipate, the lubricant droplets would vaporize less in the steam barrier, and, the lubricant delivery to the die would be enhanced.

In Figure 4.17, results were presented for the pulse spray experiments conducted at initial plate temperatures of 250 ^{0}C (P250a and P250b) and 300 ^{0}C. Duration of the pulse and idle periods were slightly different for the two cases at 250 ^{0}C and the results for the heat flux were very close, indicating a good reproducibility for this experiment. For each pulse at 250 ^{0}C, the heat flux decreased and the amount of variation was smaller within the last pulses, while for each pulse at 300 ^{0}C, the heat flux variation was negligible. This variation was consistent with the results for the dwell experiments, in which the heat flux stayed almost constant for a larger interval of time for the L300 than for L250 case. The heat flux level decreased with each subsequent pulse. This decrease in heat flux from pulse to pulse was due to the temperature evolution of the plate surface. The surface temperature, shown in Figure 4.18, decreased within each pulse, then increased during the idle periods to a lower value than that for the previous pulse. Thus, the surface temperature decreased affecting the subsequent heat flux levels. The results for the heat transfer coefficients are presented in Figure 4.19. As expected, the variation of *h* mimics that of *q"*. The values for the h in the pulse case were larger than those for the dwell case (Figures 4.14 and 4.19). When the pulse was applied, the h varied from a high of 15 to 4kW/m^{2}K, while for the L250, the dwell case, h varied from 7 to 2kW/m^{2}K.

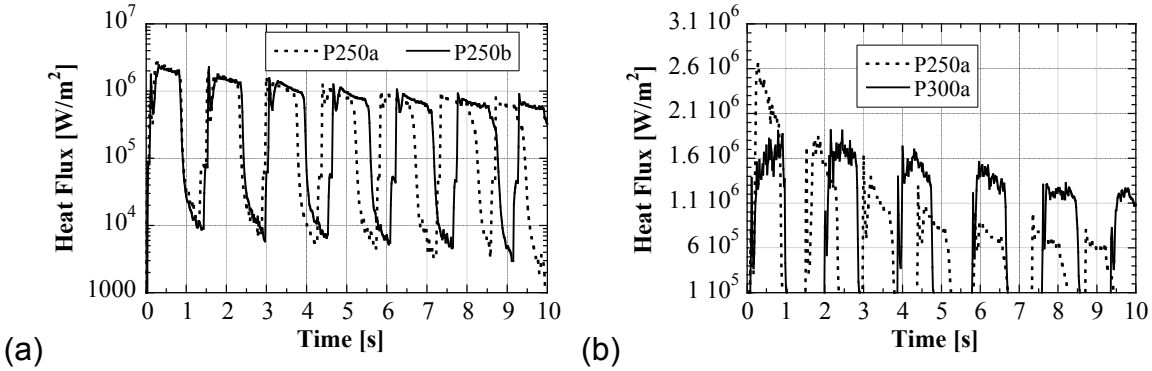

Figure 4.17 Heat flux evolution for pulse-spray experiments conducted at an initial plate temperature of (a) 250^{o}C and (b) 300 ^{o}C.

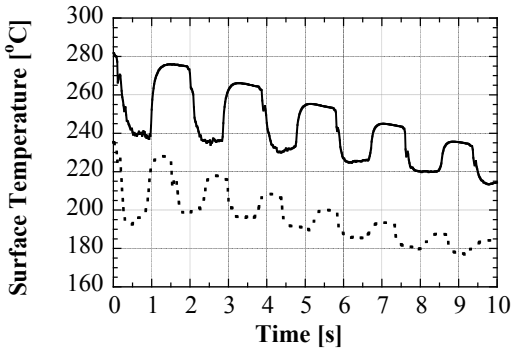

Figure 4.18 Surface temperature evolution for pulse-spray experiments conducted at an initial plate temperature of 250 and 300 °C.

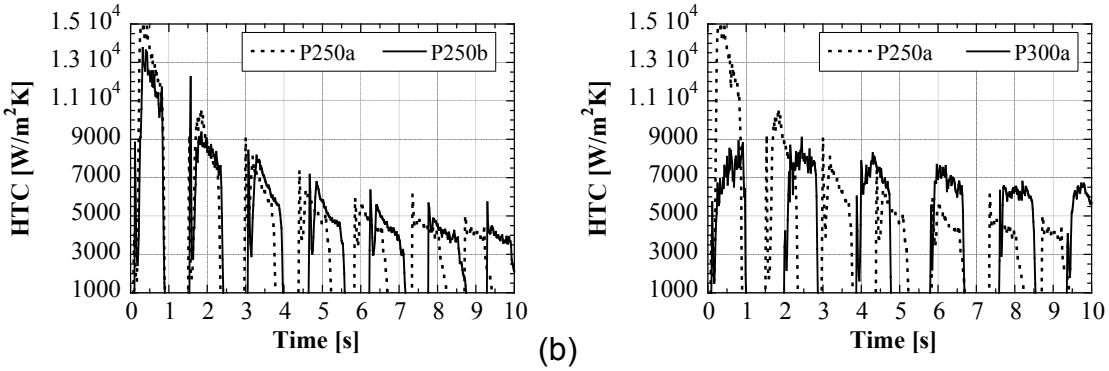

Figure 4.19 Heat transfer coefficient evolution for pulse-spray experiments conducted at an initial plate temperature of (a) 250°C and (b) 300 °C.

4.7 SWEEP SPRAY APPLICATION OF LUBRICANT

The application of lubricant by moving the nozzle across the die surface is very common for large dies. The sweep application technique was also believed to be more effective in lubricant application since after the nozzle moves away from an area, the steam barrier would dissipate and the lubricant can be applied more effective during the next sweep (Herman, 2003). To date, there is no data reported on heat flux for the sweep application technique.The experimental setup used for the sweep application experiments is shown in Figure 4.20 (a). A fixture was design such that the spray nozzle would move parallel to the plate. The sweep experiments were conducted by moving the spray nozzle from one side of the plate to the other side with velocity v_S. The center of the plate was sprayed six times as the spray nozzle was moved forth and back over the plate. On the plate, the area covered by the spray was a disk of diameter D_S=5.6 cm. The measured heat flux is shown in Figure 4.20 (b) for a nozzle velocity of 10 cm/s. For each sweep, the heat flux rose to a maximum value as spray cone moved over the sensor area and then decreased as the spray cone moves away from the sensor area. With the exception of the first sweep, the maximum heat flux was larger than those recorded for the dwell and pulse cases. One explanation of the higher heat rate removal in this sweep case would be that the radial steam flow at the edge of the spray cone aided in the dissipation of the steam barrier, effect that could not be possible for the dwell and pulse cases. This heat flux data can be used to obtain the distribution of the heat flux in the radial direction, i.e., away from the sensor surface towards the edges of the spray-affected area. The data for the surface temperature was presented in Figure

4.20 (c). As for the pulse cases, the surface temperature gradually decreased from sweep to sweep. The surface temperature decreased at a slower rate for the sweep case than for the pulse case, i.e., Ts was 210 and 180 ^{0}C for the sweep and pulse cases, respectively, after 10s of spray application. The results for the heat transfer coefficients are presented in Figure 4.20 (d). As time proceeded, the maximum value for the heat transfer coefficients was higher for the sweep than the pulse cases.

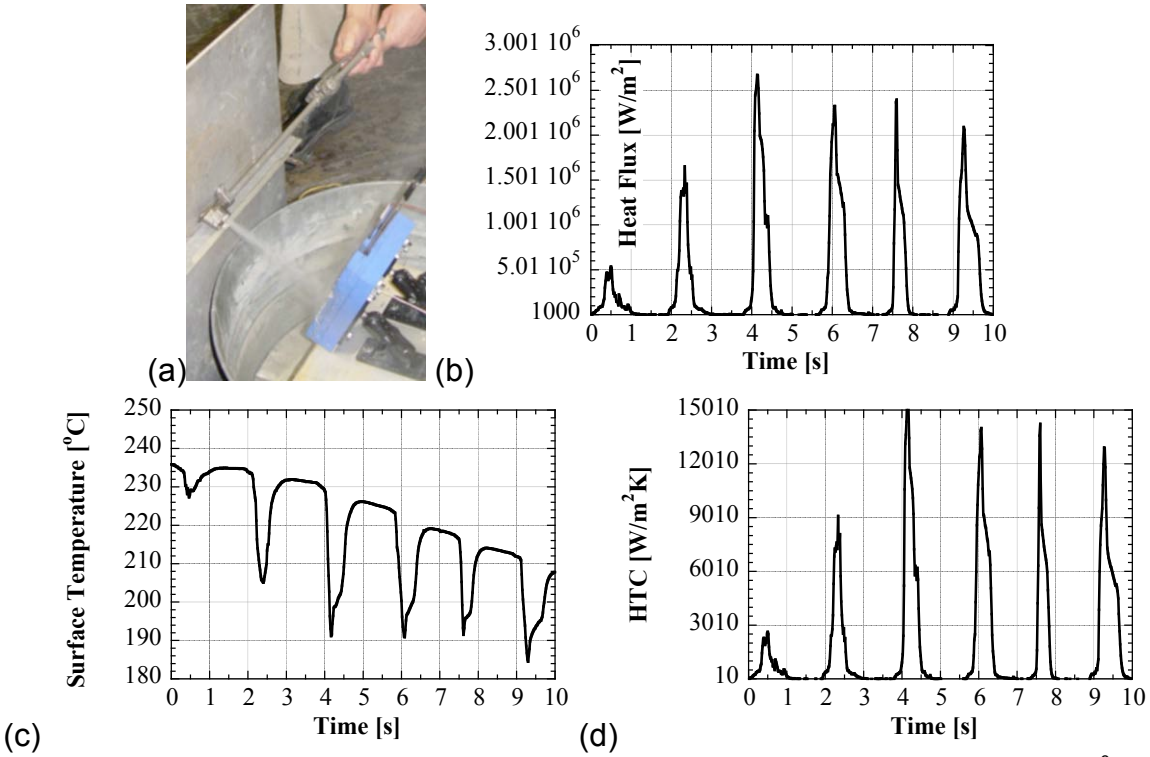

Figure 4.20 Results for the sweep-spray experiments conducted at an initial plate temperature of 250^{o}C: (a) experimental setup, (b) heat flux evolution, (c) surface temperature, and (d) heat transfer coefficient.

4.8 EFFICIENCY OF LUBRICANT APPLICATION TECHNIQUES

Several cases were run at different nozzle velocities. The results obtained at the other sweep velocities were summarized in Table 4.2 for the average heat flux. In order to compare the heat fluxes for the dwell, pulse, and sweep cases, the average heat flux was computed by considering the total spraying time, τ_t, and effective spray time, τ_e. The effective time represented the time that the lubricant was applied over the center of the plate where the heat flux sensor was located. The mass of fluid sprayed during the effective time period was also shown in Table 4.2. For the sweep cases, $\tau_e = D_S / v_S$, while for the pulse cases, the τ_e is given by the duration of all the pulse periods within the total time interval, τ_t, considered. The total amount of heat removed was defined as $q_t = \int_0^{\tau_t} q''\, dt$. The total and effective heat fluxes were defined as $q''_t = q_t / \tau_t$ and $q''_e = q_t / \tau_e$, respectively.

The heat flux results can be interpreted based on a productivity criterion, e.g., total amount of heat removed per unit time, q''_t, or cost effective criterion, e.g., total amount

of heat removed per unit mass of lubricant, q_t/m_t. From the productivity point of view, the highest heat flux, $q"_t$, was recorded for the pulse spray and the ten second dwell spray case. However, the pulse spray used only half of the amount of lubricant as the ten-pulse spray. The sweep spray at 20cm/s and 68 cm/s removed only half and a third of the heat flux removed by the pulse spray. From the point of view of lubricant consumption, the following conclusions can be drawn by examining the q_t/m_t data:

- the five-second dwell spray was more effective than ten-second one,
- the pulse application was more effective than the dwell applications,
- the sweep application at 20 cm/s was the most efficient case,
- the efficiency of the sweep application did not increase monotonically with nozzle velocity; the efficiency reached an optimum at a certain nozzle velocity. Increasing the velocity beyond the optimum one would not be effective.

Table 4. 2Average heat flux for the three application techniques obtained for an initial plate temperature of 250°C.

v_S **[cm/s]**	τ_t **[s]**	τ_e **[s]**	m_t **[g]**	m_e **[g]**	q_t **[J/m²]**	$q"_t$ **[W/m²]**	$q"_e$ **[W/m²]**	q_t/m_e **[J/m²g]**
*0	5	5	52.5	52.5	4.200e+6	4.200e+5	8.400e+5	8.000e+4
*0	10	10	105	105	5.941e+6	5.941e+5	5.941e+5	5.658e+4
**0	10	5.47	105	57.4	5.903e+6	5.903e+5	1.079e+6	1.028e+5
20	10	1.67	105	17.5	3.214e+6	3.214e+5	1.924e+6	1.833e+5
23	8.7	1.46	91.3	15.3	2.812e+6	3.220e+5	1.926e+6	1.834e+5
68	2.9	0.48	30.5	5.0	6.024e+5	2.077e+5	1.255e+6	1.195e+5

* static spray, ** pulse spray

4.9 RECOMMENDATION FOR FUTURE WORK

Data on heat flux during lubricant application are presented. A sensor was used for the direct measurement of heat flux. The heat flux data shown in this study reproduced the expected temperature variation for water spray, validating the use of these sensors for the direct measurement of heat fluxes. It was shown that for diluted lubricant sprays, the measured heat fluxes were different than those for pure water. This indicated that the sensitivity of the sensor was appropriate for measuring heat fluxes under conditions specific to the die casting process. The sensor can be used with confidence to investigate the effects of lubricant application for different dilution ratios or lubricants with different decomposition characteristics.

A sensor was used for the direct measurement of heat flux during lubricant application for the die casting process. It was found that the heat flux was time and temperature depended. The evolution of the heat flux was different for initial plate temperatures of 150 and 300 ^{o}C. Pictures of the spray indicated that the convection of the vapor spray away from the plate surface was very strong for the 300 ^{o}C case. Data for average heat fluxes indicated that for lubricant spray, the measured heat fluxes were different for the lubricant spray than those for deionized water. Due to the short time response of the sensor, data was obtained for various spray application techniques, such as sweep and pulse spray. It was found that for pulse spray, the heat flux decreases with each subsequent pulse. Considering the lubricant consumption, the pulse application was more effective than the dwell application while the sweep application at 20cm/s was the most efficient case. The data presented indicated that the heat flux sensor would be an important tool to evaluate lubricants, monitor the consistency of die lubrication process, and obtain useful process data, such as surface temperature, heat flux, and heat flux coefficients that can be used for die design.

4.10 REFERENCES

Altan, T., Bishop, S.A., Miller, R.A., Chu, Y.L., "A Preliminary Investigation on the Cooling and Lubrication of Die Casting Dies by Spraying", The 16th International Die Casting Congress and Exposition, 1991.

Chhabra, S., Chu, Y.L., and Altan, T., "An Investigation of Cooling and Lubrication of Die Casting Dies Using a Water/Lubricant Spray", *Die Casting Engineer*, vol 37(1), pp 24-27 (1993).

Fraser, D. and M. Z. Jahedi, "Die lubrication in high pressure die casting," *Die Casting and Toolmaking Technology*, Melbourne, 1997.

Garrow, D.M., "Characterization of Die Casting Die Lubricants", MSE 695 presentation, Ohio State University, 2001.

Garrow, D.M., "Characterization of Die Casting Die Lubricants", MSE 695 presentation, Ohio State University, 2001.

Herman, E.A., *Designing Die Casting Dies,* North American Die Casting Association, Rosemont, IL (1992).

Herman, E.A., "Die Spray, Die Cost and Die Life," *Die Casting Engineer*, pp. 34-36 (2003).

Incropera, F.P., De Witt, D.P., *Fundamentals of Heat and Mass Transfer*, 2nd edition, John Wiley & Sons, New York, NY (1981).

Issa, R.J., Numerical modeling of the dynamics and heat transfer of impacting sprays for a wide range of pressures, PhD Theses, University of Pittsburgh, Pittsburgh, PA, 2003.

Lee, I.S., Nguyen, T.T., Leigh, G.M., "Spray Cooling of Die Casting Dies", Australian Die Casting Association, pp 53-69 (1989).

Liu, G.W., Morsi, Y.S., Clayton, B.R., "Characterisation of the Spray Cooling Heat Transfer Involved in a High Pressure Die Casting Process", *International Journal of Thermal Science*, vol 39, pp 582-591 (2000).

Piskoti, C.R., "New Study Turns up the Heat on Die Spray Cooling", *Die Casting Engineer*, vol 47(1), pp 44-45 (2003).

Sabau, A.S. and Wu, Z., Evaluation of a Heat Flux Sensor for Spray Cooling for the Die Casting Processes, Submitted for publication to the Journal of Materials Processing Technology, November 2005.

Sabau, A.S. Measurement of Heat Flux and Heat Transfer Coefficient Due to Spray Application for the Die Casting Process, Submitted for publication to the ASME J. Heat Transfer, December 2005.

Sozbir, N., Chang, Y.W., Yao, S.C., 2003, "Heat Transfer of Impacting Water Mist on High Temperature Metal Surfaces", *Transactions of the ASME*, vol 125, pp 70-74 (2003).

5 High Pressure Die Casting

ABSTRACT

Due to the high pressure, the liquid metal enters into the mold at high velocities. The liquid metal comes out through a slit-like opening into the die cavity (10 to 1 aspect ratio) and it is believed to undergo severe break-up and even atomize. These phenomena give rise to fragmented flows during mold filling, such as droplet-like flows, which are believed to yield inherent porosity defects and typical skin microstructures in HPDC. In collaboration with ORNL staff, both experimental and computational studies were conducted at the University of Kentucky on jet flows during the HPDC of magnesium alloys. The goals of this task were to (1) experimentally obtain the velocity distribution and, if applicable, the size distributions of atomized droplets, (2) examine the mold filling pattern using transparent dies, and (3) attempt to develop a computational model that can predict the jet break-up and atomization processes.

Since it is difficult to perform experiments with molten magnesium, an analog liquid was sought for conducting experiments. A scale analysis showed that the fluid dynamics in HPDC are governed by Weber number, We, and Reynolds number, Re. The Weber number relates the dissipative effect of the surface tension to the de-stabilizing aerodynamic forces, while the Reynolds number relates the inertial to the viscous forces. Thirty two liquids were screened for the given gate conditions. The scale analysis indicated that warm water was the best candidate for the analogue liquid.

The flow visualization systems available at UKY-Lexington were used to characterize the jet flow through gates used in die casting processes. First, open die experiments were conducted in order to investigate the flow pattern, such as jet breakup and atomization, as the liquid exits the gate. The Phase Doppler Particle Analyzer (PDPA) and Particle image velocimetry (PIV) were used to measure the particle size and velocity of the liquid analogue at different distances from the gate. The data from open die experiments was used to develop correlation for jet break-up and atomization.

Numerical simulations were performed using the commercial CFD package Fluent™ since it includes fluid-gas interaction and droplet atomization features. The Reitz atomization model, which was developed for combustion applications, was used to simulate possible atomization effects. In the Eulerian approach, both the air and molten metal are modeled on a fixed grid, and Volume of Fluid (VOF) techniques are used to track the interface between the two materials. A subgrid model was developed for the VOF methodologies based on open die experiments. The subgrid model was implemented in Fluent™. This approach was developed in order to enable mold filling simulations on coarse grids and still be able to predict the small-scale atomization process.

5.1 EXPERIMENTAL INVESTIGATION

5.1.1 Scale Modeling Analysis

In the initial stages of the project, scale analysis was performed in order to assess which dimensionless groups govern the atomization process in high-pressure die casting. As the baseline case, the injection of liquid Magnesium at 923K through a 1.55x82 mm slot with an average injection velocity of 50 m/s exhausting in quiescent air at standard conditions was considered. The analysis showed that 2 dimensionless groups can describe the main dynamics of the process. The Weber number (We), which relates the dissipative effect of the surface tension to the de-stabilizing aerodynamic forces, and the Reynolds number (Re), that relates the inertial to the viscous forces in the flow. In order to perform meaningful experimental work through scale models of the injection nozzle, the We and Re of the experiment had to match those of the real process. For the baseline case, these two numbers were calculated to be:

$$We_{Mg} = \frac{\rho_{Mg} V_{inj} D_{Hydr}}{\sigma} = 22.7x10^3 \quad Re_{Mg} = \frac{\rho_{Mg} V_{inj} D_{Hydr}}{\mu_{Mg}} = 209.2x10^3 \quad Re_{Gas} = \frac{\rho_{Air} V_{inj} D_{Hydr}}{\mu_{Air}} = 10.6x10^3 \qquad (5.1)$$

Note that the ratio of We to Re produces a third dependent dimensionless group, the Capillary number (Ca), which relates the viscous forces to the surface tension. In the above calculations the properties of the liquid Magnesium and of the air at rest filling the cavity were taken to be as shown in

Table 5.1. Nominal properties of Magnesium and air used in simulations.

	Mg	**Air**
Initial Temperature, T (K)	923	300
Density, ρ (kg/m^3)	1700.0	1.2
Viscosity μ (Ns/m^2)	0.0012360	0.0000173
Surface Tension σ (N/m)	0.57	

For the experimental work, air was kept as the quiescent gas filling the mold before injection. The selection of the injection material involved the screening of the properties of 32 liquids and the calculation of the corresponding We and Re for the given injection conditions. Apart from matching the dimensionless groups, consideration was given to the practicality of using toxic or very expensive liquids. The selection process indicated that water at 90 deg C could match the We and Re of the injection process when the dimensional scale is 1 and the injection velocity is half that of the actual process.

According to the scale analysis, the injection of water could provide a model to study the atomization process of molten Magnesium. However, solidification patterns and mold-filling could not be measured through the use of water. Therefore, a wax was also considered to simulate the injection and filling process. However, measurements of the wax surface tension showed a high dependency of this property on the temperature

range of interest and made the proper scaling of the experiment impossible. These measurements were performed by a third-party specialized in the measurements of liquid properties, and the results are shown in Figure 5.1.

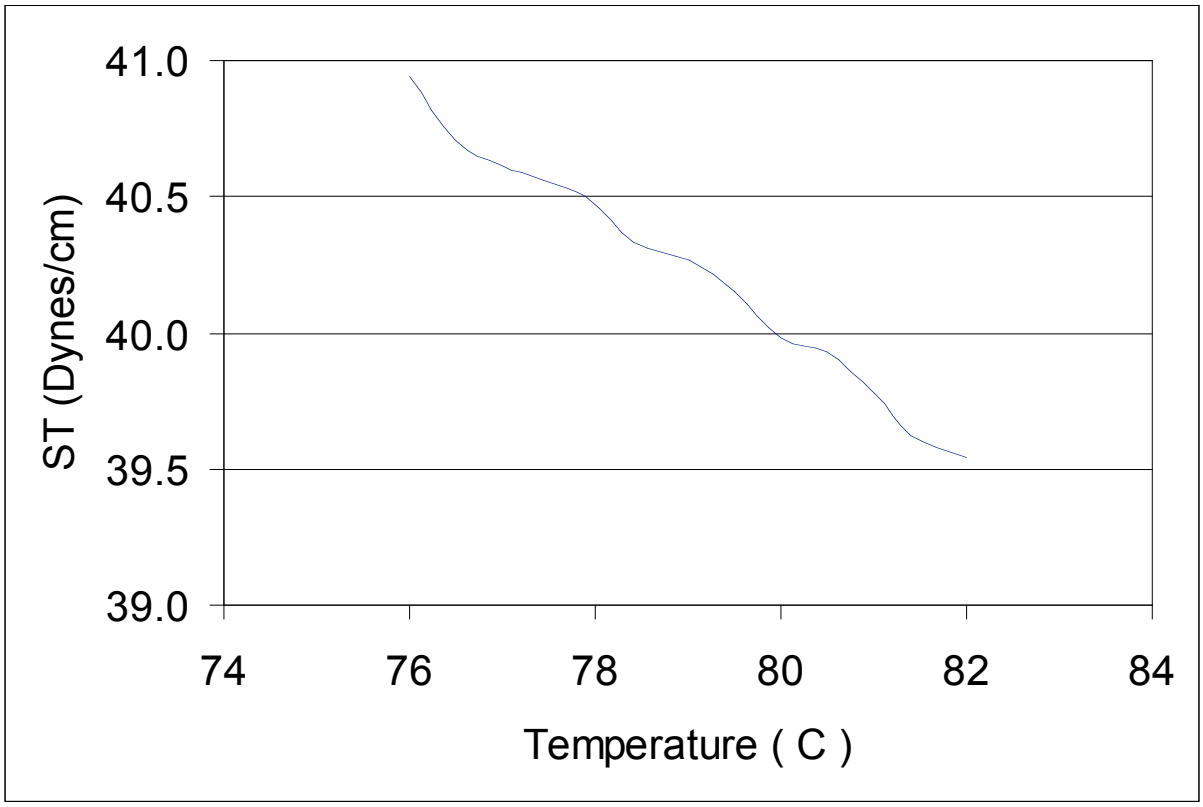

Figure 5.1. Variation of the surface tension of the considered with temperature. The large surface tension excursion over the temperature range of interest made it impracticable to use the wax for the experiments.

5.1.2 Scale Analysis

Important forces in the breakup and atomization of a liquid sheet are inertia (ρU^2), surface tension (σ/L), and viscous force ($\mu U/L$), where ρ, U, σ, L, and μ are respectively density [kg/m^3], velocity [m/s], surface tension [N/m], length [m], and viscosity [Pa s]. These three forces result in two dimensionless groups, i.e., Reynolds number (Re = $\rho UL/\mu$) and Weber number (We = $\rho U^2 L/\sigma$). Therefore, a prototype (an actual HPDC process in our case) and its scale model must have same Reynolds and Weber numbers:

$$\frac{\rho_1 U_1 L_1}{\mu_1} = \frac{\rho_2 U_2 L_2}{\mu_2}, \qquad (5.2)$$

and

$$\frac{\rho_1 U_1^2 L_1}{\sigma_1} = \frac{\rho_2 U_2^2 L_2}{\sigma_2}, \tag{5.3}$$

where subscripts 1 and 2 represent the prototype and its scale model, respectively. From equations (5.1) and (5.2), another scaling law can be obtained:

$$\frac{U_1 \mu_1}{\sigma_1} = \frac{U_2 \mu_2}{\sigma_2}. \tag{5.4}$$

Equation (5.3) states the equality of Capillary number (Ca), which becomes the quantity of interest when the viscous force has more influence on the system than the inertia (i.e., Re << 1). On the other hand, Weber number is the quantity of interest for Re >> 1, which is the case in most HPDC processes.

Equations (5.1) and (5.2) yield

$$\frac{L_2}{L_1} = \left(\frac{\rho_1}{\rho_2}\right)\left(\frac{\sigma_1}{\sigma_2}\right)\left(\frac{\mu_2}{\mu_1}\right)^2 \tag{5.5}$$

and

$$\frac{U_2}{U_1} = \left(\frac{\sigma_2}{\sigma_1}\right)\left(\frac{\mu_1}{\mu_2}\right). \tag{5.6}$$

Equations (5.4) and (5.5) enable us to determine the dimension and the liquid sheet velocity of a scale model when a different liquid is used in the scale model experiment than its prototype. The flow rate, Q [m^3/s], of the scale model can be calculated by

$$\frac{Q_2}{Q_1} = \left(\frac{U_2}{U_1}\right)\left(\frac{L_2}{L_1}\right)^2 = \left(\frac{\rho_1}{\rho_2}\right)^2\left(\frac{\sigma_1}{\sigma_2}\right)\left(\frac{\mu_2}{\mu_1}\right)^3. \tag{5.7}$$

Table 5.2 lists the relative size (L_2/L_1), relative velocity (U_2/U_1), and relative flow rate (Q_2/Q_1) calculated from equations (5.4)–(5.6) for a variety of liquids. If mercury or ammonia were used as the liquid of our scale model experiment, only a small flow rate would be required, which is an advantage for a laboratory-scale experiment. However, these liquids were not chosen because of safety concern. The most convenient liquid, water, would require about 7.6 times greater flow rate than magnesium; a powerful pump would be needed for the scale model experiment.

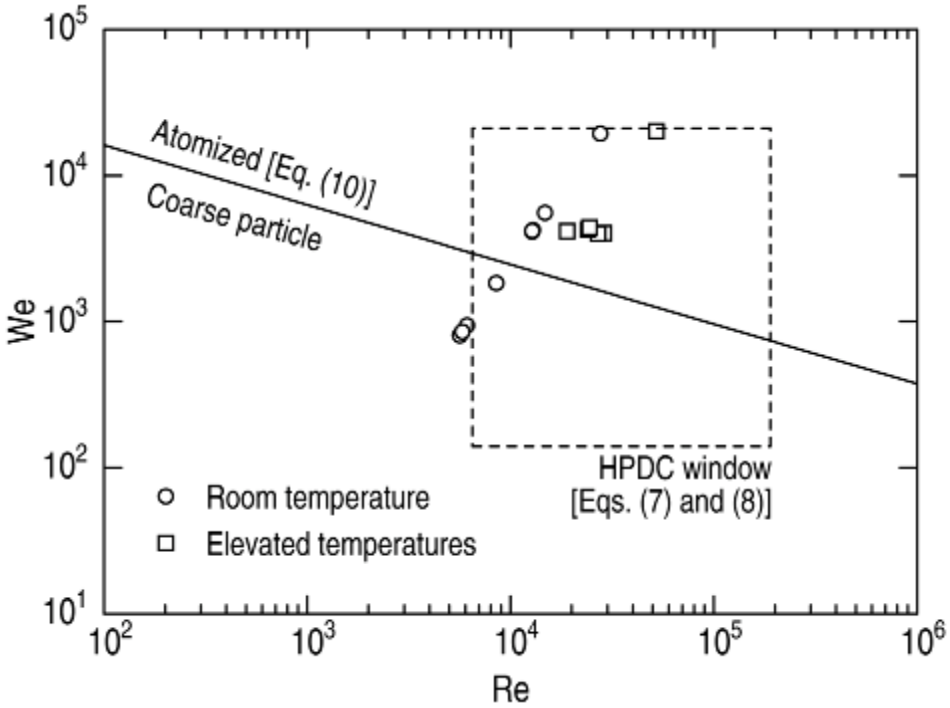

Figure 5.2. Re and We numbers of our scale model experiments.

The properties of water, however, are temperature-dependent. Consequently, the relative flow rate (Q_2/Q_1) also depends on its temperature as shown in Table II. If warm water at 60–70 °C is used in the scale model experiment, a high flow rate is not needed. Indeed, a flow rate lower than the prototype is enough at 70 °C or higher temperature. Based on these considerations, warm water was chosen as the liquid in our scale model experiment.

5.1.3 Re and We Numbers and Atomization Criterion

Because of the two-dimensional nature of the breakup of a liquid sheet (Lopez-Pages at al., 2004), the gate thickness rather than the gate width is the length scale of importance. Therefore, Reynolds and Weber numbers are computed based on the gate thickness and the liquid velocity at gate (gate velocity). Typical ranges of the gate thickness and the gate velocity in HPDC processes are 0.5–3.0 mm and 10–50 m/s, respectively. These ranges with the properties of magnesium yield the ranges of Reynolds and Weber numbers:

$$6.5 \times 10^3 < \mathrm{Re} < 1.9 \times 10^5, \tag{5.8}$$

and

$$1.4 \times 102 < \mathrm{We} < 2.1 \times 104. \tag{5.9}$$

Our scale model experiments are designed such that their Reynolds and Weber numbers are within these ranges as explained below. Herman et al. (1975) reviewed previous experimental data with molten metals and obtained the following criterion for atomization:

$$l u^{1.71} \rho \mu^{-0.29} \sigma^{-0.71} > 3700 \,[\text{SI units}]\,, \tag{5.10}$$

where *l* and *u* are the gate thickness and the gate velocity, respectively. In writing equation (5.9), it was assumed that the gate width is usually much larger than the gate thickness. It is important to note that equation (5.9) can be rewritten in terms of Reynolds and Weber numbers as

$$\mathrm{Re}^{0.29}\,\mathrm{We}^{0.71} > 3700 \quad \text{or} \quad \mathrm{We} > \left(\frac{3700}{\mathrm{Re}^{0.29}}\right)^{1/0.71}. \tag{5.11}$$

Figure 5.2 shows the atomization criterion [equation (5.10)] as well as Reynolds and Weber numbers of our scale model experiments (whose detail is given below). It can be seen that the scale model experiments cover a wide range of conditions within equations (5.7) and (5.8) by using various water temperatures.

Table 5.2. Relative Size, Relative Velocity, and Relative Flow Rate of a Scale Model with Different Liquids.

Liquid	Density [kg/m^3]	Viscosity [Pa s]	Surface tension [N/m]	Relative size L_2/L_1 [–]	Relative velocity U_2/U_1 [–]	Relative flow rate Q_2/Q_1 [–]
Mercury	1.35×10^4	1.52×10^{-3}	4.74×10^{-1}	0.21	0.68	0.03
Ammonia	6.03×10^2	1.35×10^{-4}	1.98×10^{-2}	0.91	0.32	0.26
Carbon disulfide	1.26×10^3	3.65×10^{-4}	3.15×10^{-2}	2.00	0.19	0.75
Sulfur dioxide	1.37×10^3	3.50×10^{-4}	2.16×10^{-2}	2.45	0.13	0.81
Nitrogen	8.41×10^2	2.04×10^{-4}	1.05×10^{-2}	2.79	0.11	0.87
Diethyl ether	7.08×10^2	2.24×10^{-4}	1.65×10^{-2}	2.55	0.16	1.04
Acetone	7.85×10^2	3.04×10^{-4}	2.27×10^{-2}	3.08	0.16	1.54
Bromine	3.10×10^3	9.50×10^{-4}	4.00×10^{-2}	4.31	0.09	1.71
Acetonitrile	7.77×10^2	3.41×10^{-4}	2.85×10^{-2}	3.12	0.18	1.77
Chloroform	1.48×10^3	5.40×10^{-4}	2.66×10^{-2}	4.39	0.11	2.07
Hexane	6.55×10^2	2.92×10^{-4}	1.79×10^{-2}	4.31	0.13	2.48
Triethylamine	7.24×10^2	3.41×10^{-4}	2.01×10^{-2}	4.74	0.13	2.88
Ethyl acetate	8.95×10^2	4.26×10^{-4}	2.32×10^{-2}	5.19	0.12	3.19
Nitric acid	1.51×10^3	7.49×10^{-4}	4.12×10^{-2}	5.34	0.12	3.41
Nitromethane	1.13×10^3	6.27×10^{-4}	3.62×10^{-2}	5.69	0.13	4.07
Toluene	8.62×10^2	5.52×10^{-4}	2.78×10^{-2}	7.54	0.11	6.23
Hydrogen peroxide	1.44×10^3	1.14×10^{-3}	7.97×10^{-2}	6.70	0.15	6.84
Water	9.97×10^2	8.91×10^{-4}	7.20×10^{-2}	6.56	0.18	7.57
Benzene	8.74×10^2	6.03×10^{-4}	2.82×10^{-2}	8.75	0.10	7.80
Helium	1.43×10^2	3.85×10^{-5}	2.56×10^{-4}	23.97	0.01	8.31
Methanol	7.87×10^2	5.45×10^{-4}	2.21×10^{-2}	10.13	0.09	9.06
Heavy water	1.11×10^3	1.10×10^{-3}	7.19×10^{-2}	9.04	0.14	11.59

Table II. Relative Size, Relative Velocity, and Relative Flow Rate at Various Temperatures of Water

Water temperature [°C]	Density [kg/m^3]	Viscosity [Pa s]	Surface tension [N/m]	Relative size L_2/L_1 [–]	Relative velocity U_2/U_1 [–]	Relative flow rate Q_2/Q_1 [–]
10	1.00×10^3	1.31×10^{-3}	7.42×10^{-2}	13.72	0.12	23.20
20	9.98×10^2	1.00×10^{-3}	7.28×10^{-2}	8.16	0.16	10.55
30	9.96×10^2	7.98×10^{-4}	7.12×10^{-2}	5.33	0.19	5.51
40	9.92×10^2	6.53×10^{-4}	6.96×10^{-2}	3.66	0.23	3.11
50	9.88×10^2	5.47×10^{-4}	6.79×10^{-2}	2.65	0.27	1.89
60	9.83×10^2	4.67×10^{-4}	6.62×10^{-2}	1.99	0.31	1.22
70	9.78×10^2	4.04×10^{-4}	6.44×10^{-2}	1.54	0.35	0.82
80	9.72×10^2	3.55×10^{-4}	6.26×10^{-2}	1.23	0.38	0.58
90	9.62×10^2	3.14×10^{-4}	6.08×10^{-2}	1.00	0.42	0.42

5.1.4 Experimental Setup

The nozzle used in the experiments was designed from inverse-engineering of a die-cast part produced with the actual die-casting equipment. While the actual gate had a complicated geometry, with two curved surfaces intersecting and creating the gate area, the nozzle design used in the experiments was simplified as shown in Figure 5.3. The

simplification of the gate geometry insures that the observed atomization patterns are generated by a limited number of factors and not by the complicated nozzle geometry.

Figure 5.4 (a) shows a schematic and a photograph of a nozzle used in this study. A cavity in an aluminum plate was replicated from an actual gate design. The nozzle is designed in such a way that the gate thickness can be varied by inserting thin plates as shown in the figure. A high-pressure hose was attached to the nozzle for the delivery of water. The flow rate of water was varied using a reciprocating pump. The water temperature was controlled using a thermostatic bath. The experimental apparatus used for the production of the desired flow rate is shown in Figure 5.4 (b), which includes the nozzle, its support structure, the reciprocating electric pump and the high-pressure hoses.

In the experiments reported here, the gate thickness was fixed at 0.5 mm. To vary the gate velocity with a constant flow rate, two nozzles with different gate widths were used: Nozzle 1 with the gate width of 11 mm and Nozzle 2 with the gate width of 5 mm. The experimental conditions of 12 runs are summarized in Table III (see also Figure 5.1). The average gate velocity was estimated from the total flow rate of water and the gate area.

The breakup and atomization phenomena were monitored using a 2-D particle image velocimetry (PIV) system. Since general theory and procedures for PIV system are detailed in Raffel et al. (1998) and Hassan et al. (2005), only a summary of the PIV system is provided here. Our PIV system consists of three main units: two Nd:YAG (532 nm wavelength) pulse lasers, an image capturing unit, and a computing and display unit. The laser light reflected by the liquid sheet was recorded using a 30-frame-per-second cross-correlation CCD camera on a two-frame straddle, one frame for each pulse. In addition to the PIV system, a 2-D component phase Doppler particle analyzer (PDPA) system was used to measure the diameter and the velocity of droplets during breakup and atomization.

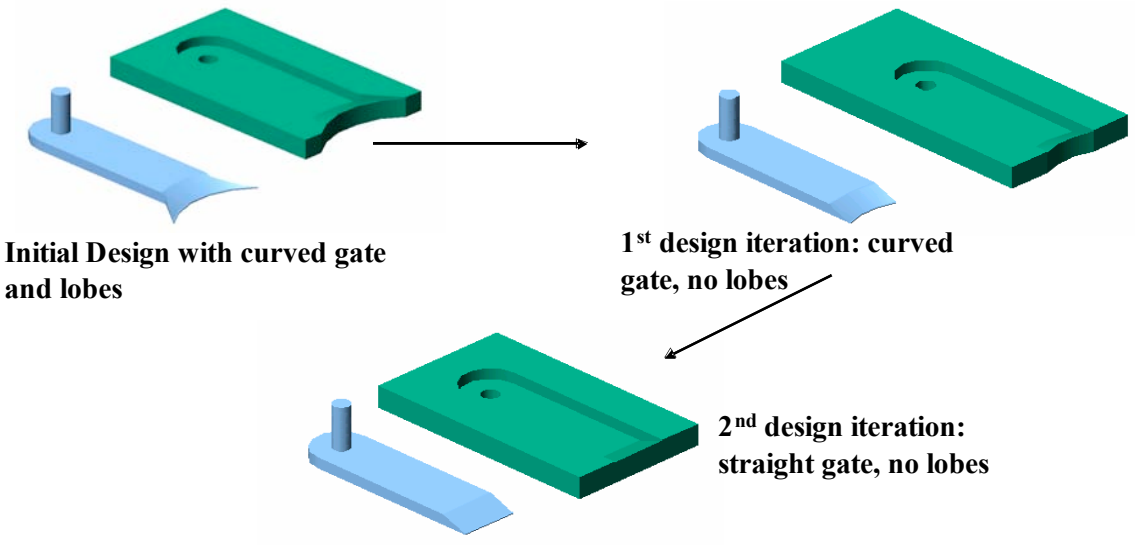

Figure 5.3. Inverse-engineering design of the gate used in the experiment from actual die-cast part. The gate geometry was simplified to isolate the different physical phenomena that participate in the atomization of the injected liquid.

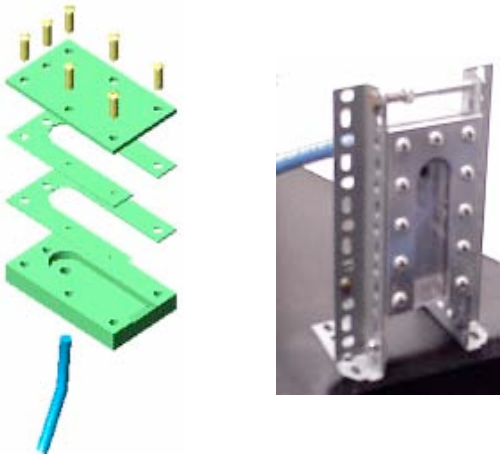

(a)

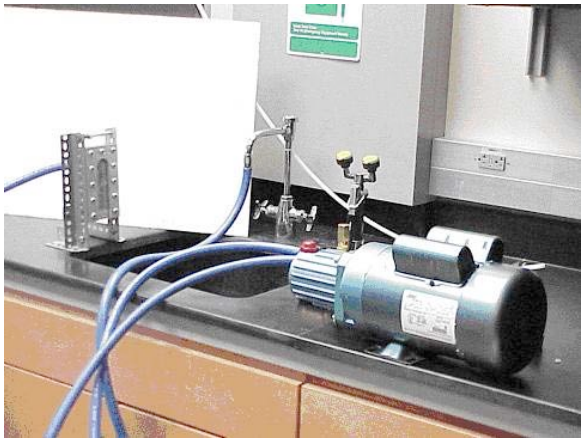

(b)

Figure 5.4. A schematic and a photograph of a nozzle used in the experiments. (a) Nozzle-gate assembly. (b) The nozzle assembly next to the reciprocating pump.

Table 5.3. Experimental conditions

Run	T [°C]	u [m/s]	Re [–]	We [–]
1	22	10.8	5.64×10^3	8.05×10^2
2	22	11.1	5.80×10^3	8.50×10^2
3	22	11.7	6.11×10^3	9.44×10^2
4	22	16.4	8.53×10^3	1.84×10^3
5	22	24.8	1.29×10^4	4.23×10^3
6	22	28.4	1.48×10^4	5.54×10^3
7	22	53.1	2.77×10^4	1.94×10^4
8	44	24.2	1.90×10^4	4.17×10^3
9	60	24.4	2.45×10^4	4.42×10^3
10	60	52.0	5.22×10^4	2.01×10^4
11	65	23.1	2.70×10^4	4.01×10^3
12	74	23.0	2.88×10^4	4.04×10^3

5.1.5 Experimental Results and Discussion

The Weber numbers of Runs 1–4 are well below the critical value suggested by Herman et al. (1975) [equation (5.10)]. In accordance with their criterion, no atomization of the water sheet was observed under these conditions. The liquid sheet did not breakup within the distance of measurement (about 200 mm).

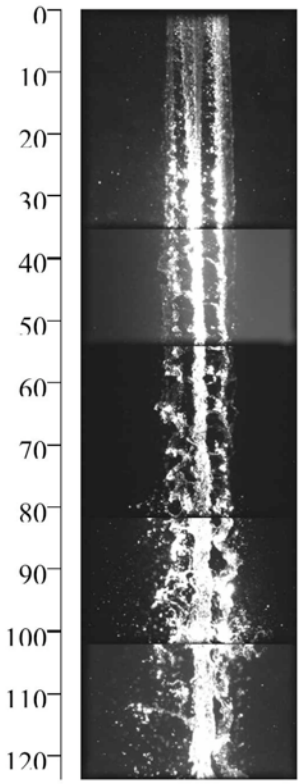

Figure 5.5. PIV image of run 9. Distance from gate is shown in [mm].

Figure 5.5 shows an image obtained by the PIV system under the condition of Run 9 of Table 5.3. The Weber number of Run 9 is slightly above the critical value. The breakup was not observed until $y \sim 80$ mm under the condition of Run 9 (y is the distance from gate). The formation of droplets was observed for $y > 80$ mm although the continuous liquid jet is still present as shown in Figure 5.3. Because of the low number density of the droplets and the presence of the continuous liquid jet, a PIV velocity map was not able to be obtained for Run 9. For $y < 80$ mm, on the other hand, little formation of droplets was observed although liquid sheet instability grew and the surface of liquid sheet was not smooth. The observed mechanism of droplet formation was similar to earlier studies (Squire ,1953, Fraser et al. 1962), i.e., the shearing instability mechanism. These liquid sheet behaviors may be thought of as a transition from the continuous liquid regime to the atomized liquid regime.

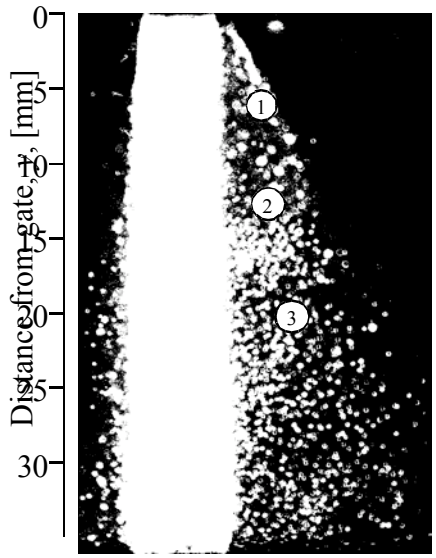

Figure 5.6. PIV image of run 10. The locations of PDPA are shown in circles.

Table 5.4. Measured Droplet Diameter and Velocity

	Units	Location 1[a]	Location 2[a]	Location 3[a]
x-velocity	[m/s]	2.80	2.87	2.95
y-velocity	[m/s]	16.43	15.08	15.01
x-velocity RMS	[m/s]	2.82	2.95	3.12
y-velocity RMS	[m/s]	6.02	5.92	6.13
Diameter	[μm]	11.82	11.95	12.6

[a] Locations are indicated in Figure 4.

Arai and Hashimoto (1985) studied the disintegration of liquid sheets injected into a co-flowing air-stream. In their experiments, the air velocity was 23–67 m/s and the liquid velocity was 0.5–2.0 m/s, yielding relative velocities between air and liquid that are similar to our experiments (11–53 m/s, see Table 5.3). Also, the liquid sheet thicknesses in their study were 0.4 and 1.0 mm, which are again similar to our experiments (0.5 mm). They determined breakup lengths by averaging values obtained from many photographs. They observed that the breakup length decreases with an increase in the relative velocity for a constant liquid sheet thickness. They obtained an empirical equation for dimensionless breakup length:

$$\frac{L_b}{l} = 0.97\left(\frac{l}{l_0}\right)^{-0.5} \mathrm{We_g}^{-0.5}\,\mathrm{Re}^{0.6}, \tag{5.12}$$

where L_b is breakup length, l is the thickness of liquid sheet, l_0 = 0.4 mm, and $\mathrm{We_g}$ is Weber number based on the air density:

$$\mathrm{We_g} = \frac{\rho_g U_R{}^2 l}{\sigma}, \tag{5.13}$$

where U_R is relative velocity between air and liquid. The Reynolds number in equation (5.11) is based on the liquid sheet thickness, the liquid sheet velocity, and liquid properties. Note that the water sheet is injected into quiescent air in our case; therefore, U_R is equal to the gate velocity. Equation (5.11) yields a breakup length of about 80 mm for Run 9, which reasonably agrees with our observation, suggesting that relative velocity is a rather important parameter than absolute velocity.

Figure 5.4 shows a PIV image of Run 10. Under the condition of Run 10, Weber number is much larger than the critical value. Consequently, atomization was observed at the gate exit. The PIV image clearly captured the liquid atomization as shown in the figure. However, the droplet distribution was not uniform enough to measure the velocity map by our PIV system. On the other hand, the PDPA system was successfully used to measure the local size and velocity of droplets; the PDPA results at three different locations indicated in Figure 5.4 are shown in Table IV.

The average diameter of droplets was slightly larger than 10 μm, which is much smaller than the gate thickness (0.5 mm). This is typical in liquid atomization. It was found that the droplet diameter slightly increased as they traveled downstream, possibly because of droplet growth due to the collision of droplets. The velocity of droplets was less than 20 m/s, which is less than half of the gate velocity (52 m/s). Furthermore, the velocity of droplets decreases as they travel downstream. This may indicate that droplets are decelerated due to the drag force from surrounding air.

5.2 NUMERICAL SIMULATIONS

Experimental investigations are capable of accurately reproducing the jet breakup that occurs in the actual process. Usually, for a non-cavitating jet, it is necessary to match the Reynolds and the Weber number as well as the density ratio of the real process in order to accurately reproduce the atomization under controlled conditions (see Lefebvre, 1989, Taylor et al. 1983, Wang et al., 1996, Youngs, 1982, and Sirignano, 1999). However, experiments tend to be expensive to perform and the data that can be extracted from them is often limited and physical insight can be inferred only indirectly. At the other end of the spectrum of the measuring techniques are numerical simulations of the atomization process. The simulations make use of the physical laws governing the atomization process or of their simplified models and solve them numerically over a discretized space. Numerical simulations offer the advantage of creating a continuous solution for the entire flowfield and, therefore, make it possible to sample the flow at any

location of interest. Further, simulations are relatively low-cost to perform and are well-suited for parametric and exploratory studies. However, simulations suffer from several deficiencies, primarily connected to the reliability and accuracy of the physical models and to the numerical characteristics of the discretization schemes. In general, simulations need some form of experimental validation to acquire a quantitative level of confidence. Also, improved accuracy often comes at a price in the form of higher computational costs. For the aforementioned reasons, applied researchers make widespread use of numerical simulations to optimize the injection process in die casting applications. Two general approaches exist: the Eulerian and the Lagrangian (Taylor et al., 1983, Fluent, 2003, Sirignano, 1999, Lin et al., 1998, Lin, 2003). In the Eulerian approach a fixed computational domain is used and conservation equations are solved over each computational cell. In the Lagrangian approach there is no need to have a fixed-in-space computational grid and the particle trajectory is calculated by integrating its equation of motion in discrete time steps.

Several computational methods exist within each of the two modeling strategies. For the Eulerian approach, the volume of fluid (VOF) model and variants (Taschl et al., 2002), the level-set method (Hirt et al., 1981) and the Moving-Particle Semi-implicit model (Pan et al., 2003)] have been extensively used in numerical simulations. However, if atomization of the injected liquid has to be captured, a very fine grid with cell sizes of the order of the atomization length-scale has to be used. This implies high memory usage and, often, prohibitively long computational times. In the Lagrangian-type family of models, we find the smooth-particle hydrodynamics (Nomura et al. 2001, Clearly et at., 2000 and 2002) model, the Reitz model (Reitz, 1987, Reitz et al. 1982, 1987), and several other numerical implementations (Thorpe et al., 1999) that use ad-hoc models for the particle drag and body forces.

The present numerical simulations were performed using the commercial CFD package Fluent v 6.1, and the open-source code OpenFoam. Fluent was chosen because of its widespread availability in industry and because of the wide range of physical modeling that it offers regarding fluid flows, fluid-gas interaction and droplet atomization. In this work, two approaches were used. (1) The first one used a mixed Eulerian-Lagrangian method in which the flow field was computed as a continuum phase (air) and the injected material was calculated as a discrete phase and its movement within the flowfield was computed by integrating an equation of motion. (2) The second approach used a fully Eulerian method: the air initially filling the mold and the injected material are simulated using conservation equations for each of the two phases are solved over a control-volume. This approach is referred to as the VOF-type simulation.

5.1.6 Discrete-phase simulations

Initially, the choice was made to use a combined Eulerian-Lagrangian approach to the study of the atomization process. Fluent offers a discrete-phase model that can compute the aerodynamic forces acting on liquid droplets moving through a gaseous flowfield. Further, two droplet break-up models are available. The Taylor Analogy Breakup, suitable for low-We breakup regimes, and the Reitz-wave model (Reitz, 1987, Reitz et al. 1982, 1987), more suited for high-We breakup regimes. Due to the high

Weber number involved in the injection molding of molten Magnesium, the Reitz model was selected to simulate the process.

5.1.6.1 Description of the Reitz model

The Reitz model was selected to simulate the atomization of the injected Magnesium mainly because of its capacity of predicting atomization for high-Weber number particle flows. At these regimes, the Kelvin-Helmholtz wave instability is believed to dominate particle break-up. One of the fundamental assumptions of the Reitz model is that atomization of the liquid and the subsequent breakup of drops are indistinguishable processes in a dense spray, i.e. there is not distinction between primary and secondary breakup. The primary breakup, in addition of being a function of the aerodynamic interaction with the continuum phase, is highly dependent on the conditions inside the injection nozzle, such as turbulence and cavitation. The secondary breakup, occurs further downstream of the nozzle and is mainly dependent on the aerodynamic interaction of the liquid particles with the continuous phase. In the Reitz model, the breakup itself is determined from the wavelength of the unstable waves on the surface of the blobs, the blobs being the discrete lumps of injected liquid.

The unstable wavelength is determined through a stability analysis of the surface of a cylindrical, viscous liquid jet. An initial infinitesimal perturbation is applied to the surface of the jet in the form of:

$$\eta = \eta_o e^{ikz+\omega t} \tag{5.14}$$

This ultimately leads to a dispersion equation that relates the growth rate, ω, to the initial perturbation η_o, to its wavelength λ plus the physical parameters of the jet and of the continuum. The dispersion equation can be solved numerically and its solution shows that there is a single maximum (or most unstable) in the wave growth rate. Reitz created several curve fits to the data obtained by the numerical solution for the maximum growth rate, Ω and the relative wavelength, Λ . These curve fits are given by:

$$\frac{\Lambda}{a} = 9.02\frac{\left(1+0.45Oh^{0.5}\right)\left(1+0.4Ta^{0.7}\right)}{\left(1+0.87We_2^{1.67}\right)^{0.6}} \tag{5.15}$$

$$\Omega\left(\frac{\rho_1 a^3}{\sigma}\right)^{0.5} = \frac{\left(0.34+0.38We_2^{1.5}\right)}{\left(1+Oh\right)\left(1+1.4Ta^{0.6}\right)} \tag{5.16}$$

The blob breakup and the resulting smaller droplets are calculated assuming that the breakup droplet radius, *r*, is proportional to the wavelength of the fastest-growing (i.e. most unstable) surface wave, i.e.

$$r = B_o\Lambda \tag{5.17}$$

Where *Bo* is a proportionality constant set to 0.61. Then, the rate of change of drop radius in a parent parcel due to drop breakup was described using the rate expression of Reitz and Diwakar:

$$\frac{da}{dt} = -\frac{(a-r)}{\tau}, \quad r \le a \tag{5.18}$$

Where a is the radius of the resulting droplets, and τ, the breakup time, is given by:

$$\tau = \frac{3.726 B_1 a}{\Lambda \Omega} \tag{5.19}$$

The constant B_1 depends on the nozzle conditions and therefore it varies from nozzle to nozzle. Values for B_0 and B_1 are given for a limited range of fuel injection conditions. In fact, the Reitz model itself was developed for fuel injection problems and currently, no other applications of the model have been found.

5.1.6.2 Two-dimensional simulations into L-Shaped closed-cavity

The airflow was calculated using the incompressible Reynolds-Averaged Navier-Stokes (RANS). Air fills up the mold before injection takes place and it is quiescent. Second-order accurate discretization schemes were used for the computation of the inviscid and viscous fluxes. A first-order discretization scheme was used for the time stepping. Since the code uses RANS, turbulence effects need to be simulated through the use of turbulence models. These effects were integrated in the calculations via a two-equation turbulence model, Menter's SST model. The SST model combines the strengths of the two most-widespread turbulence models, the *k*-ε and Wilcox's *k*-ω, and by doing so it is able to predict accurately both free-shear flows and wall bounded flows.

The droplets were injected as liquid blobs with the same diameter as the characteristic dimension of the nozzle. Once injected into the cavity, they interacted with the continuous phase, air. The major interaction between the continuous phase and the discrete phase is the displacement of the gas from the closed cavity by the injection of the discrete phase, and the atomization of the liquid phase. The gas, which is at rest before injection starts, is set in motion by the injection of the Magnesium. The pressure inside the mold increases and the gas is pushed out of the cavity through the vent. Other interactions between the gas and the molten material include atomization of the discrete phase particles through aerodynamic forces, and heat transfer.

The simulations involving the Reitz model were performed in two-dimensional closed cavities and three dimensional open cavities. The two-dimensional calculations were performed for a closed L-shaped cavity as shown in Figure 5.7. The main goal of these calculations was the study of the influence of the Reitz model parameters on the atomization. The two model parameters, B_0 and B_1, correspond to the influence of the unstable wavelength and to the nozzle conditions, respectively. The constant B_1 depends on the nozzle conditions and therefore it varies from nozzle to nozzle. Values for B_0 and B_1 are given for a limited range of fuel injection conditions since the Reitz

model itself was developed for fuel injection problems and currently, no other applications of the model have been found.

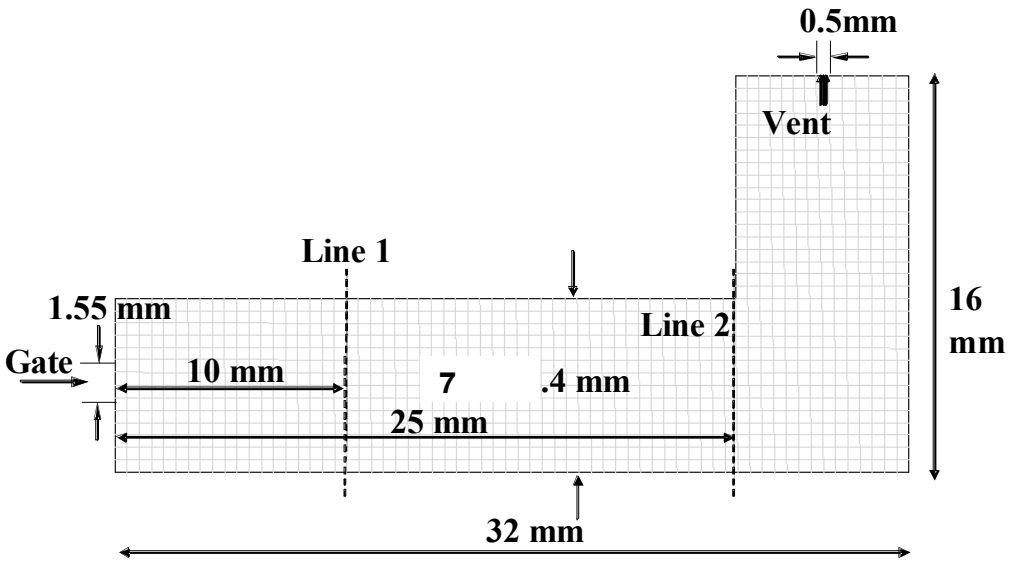

Figure 5.7 Computational domain for the 2D Reitz model calculations.

While the B_1 constant was not changed as it depends exclusively on the nozzle conditions, the constant B_0 was changed to test its effect on the atomization. The baseline case has a B_0 value of 0.61 while the high-atomization case has the constant set it to 0.12 and the low-atomization case has it set to 3.05. Changing the value of B_0 varies the diameter of the child particles formed by larger parent particles. The upper tested value, 3.05, is relatively high but it was used to highlight the sensitivity of the model to this constant. A general view of the effect of changing B_0 on the gas phase can be seen in Figure 5.8. Here the velocity contours of the gas phase are plotted for the three values of B_0 at three different injection times, nominally at *t=0.1ms, t=0.5ms*, and *t=1.0ms*. At *t=0.1ms* the three velocity fields are nearly identical, indicating that the dense jet near the injection location has not started to atomize yet. However, at *t=0.5ms* it is possible to observe the longer penetration generated when B_0*=3.05*. In this case, the particles of the molten metal do not atomize as fast as in the other cases and therefore the core of the jet remains compact and its inertia is better preserved by lower interaction with the gas. The differences between the other two cases are less accentuated. It is possible to notice that the velocity of the gas for the case with B_0 =0.61 is higher along the centerline of the cavity than for the case with B_0=0.12. This is probably the result of two phenomena: the first is the atomization of the liquid phase. The more atomization, the more particles in the flow, the more interaction with the gas phase due to the no-slip condition at the liquid-gas interface. Therefore the gas is accelerated more promptly when the atomization is greater. However, is the atomized particles are small, they will dissipate quickly their inertial energy through viscous interaction with the gas. For this reason the case for B_0=0.61 presents the core of the jet with a higher velocity than for B_0=0.12. In both cases it is visible an elongated region of high velocity that leads the penetration. It is not clear what this region depends on. The frontal boundary of the penetration or at least the extent of its effect is clearly visible in

the three cases. Looking at the cavity for t=1.0ms, we see the interaction of the solid wall of the cavity with the jet.

Again, for B_0=3.05, the effect of the jet appears more compact and concentrated. It appears that the case with the highest atomization presents the largest penetration in the vertical section. This can be explained by observing the boundary condition on the solid wall for the discrete phase. The boundary condition was set to reflect the molten liquid with a normal and tangential coefficient of restitution. So, if the liquid particles, at the moment in which they come in contact with the solid surface have a vertical (tangent to the vertical wall) component of velocity, a fraction of this velocity will be kept according to the restitution coefficient. With this in mind, we notice that the atomized particles have a larger vertical component of velocity than the non-atomized, primarily because of the transversal velocity component imparted during the atomization process. Therefore, it is expected that for the case with the lowest B_0 the penetration in the vertical section is higher than the other cases. More insight into the atomization as predicted by the Reitz model can be obtained by looking at the change in the average particle size over the whole domain.

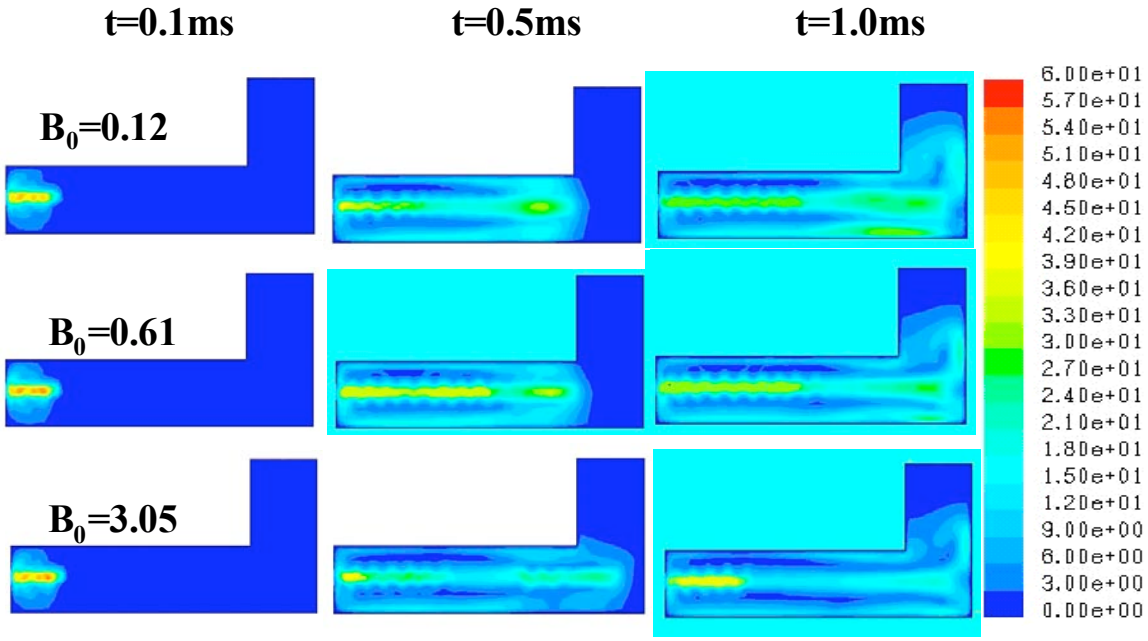

Figure 5.8. Effect of the B_0 parameter of the Reitz model on the gas phase. Contours show velocity magnitude.

Figure 5.9 shows the change of the mean particle diameter inside the closed cavity as well as the increase in total number of particles as a function of time for the case with B_0=*0.61*. The mean diameter is seen to approach asymptotically a constant value in the range of 1.2-1.3mm as injection continues. This is due to the steady decrease in relative velocity between the injected material and the gas. In the initial stages of the injection blobs of molten metal with the same diameter as the gate height are injected into the quiescent air at fixed speed. In these initial stages of the injection, the liquid Weber number is 2.2×10^4. However, as the gas is accelerated by the injected material, the Weber number between the liquid particles and the air decreases, as do the aerodynamic effects that generate the atomization. In the limit, assuming an open

cavity, the mean diameter would approach the size of the injected particles as the gas would be accelerated close to the injection speed. Figure 5.9 also shows the maximum and minimum droplet diameters. Notice that both are constant, the maximum being given by the diameter of the particles at the injection location (i.e. the gate height). The number of particles contained in the domain seems to increase almost linearly, especially after 1ms from the start of the injection. Figure 5.9 shows the change in particle mean diameter and particle count over the whole domain for the case with B_0=*0.12*. The mean diameter does not show such large variations as in the case with B_0=*0.61* and it stays relatively constant in the 0.1-0.2*mm* range.

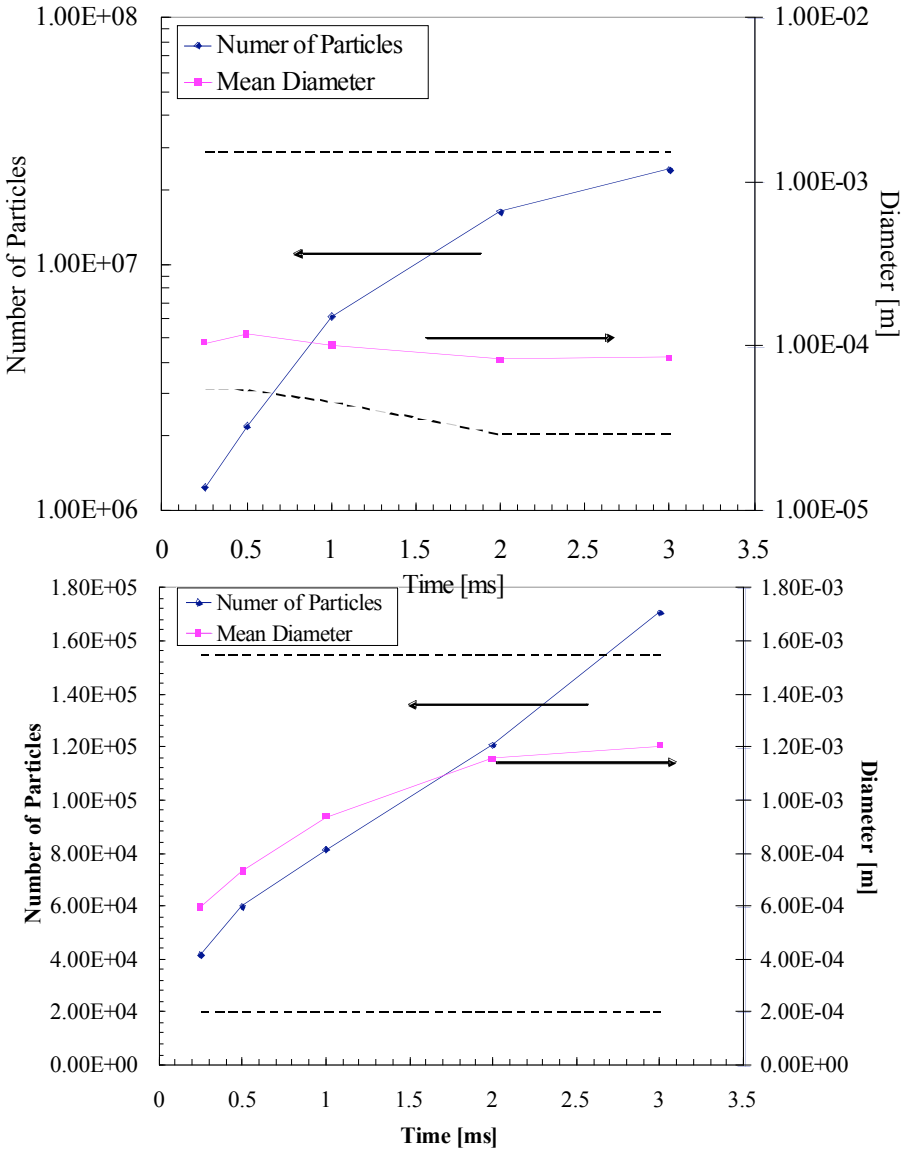

Figure 5.9. Effect of the B_0 parameter of the Reitz model on the droplet size. These two plots show the distribution of the number of particles and mean droplet diameter along the cavity centerline for B_0=0.12 (top) and B_0=0.61 (bottom), at t=1.0ms. No atomization was detected for B_0=3.05.

This much lower particle mean diameter is due to the larger rate of atomization that the Reitz model predicts with the lower B_0 value. Notice that in this case the mean diameter

decreases instead of increasing with time as in the case for B_0=*0.61*. Again, this is an indication of the higher degree of atomization obtained with the lower value of B_0 since it indicates that atomization takes place also when the gas is accelerated and the aerodynamic effects are not as strong as in the initial stages of injection. The maximum particle diameter is 1.55*mm* while the minimum diameter diminishes with time as the atomized particles undergo further atomization. The particle count for B_0=*0.12* is approximately two

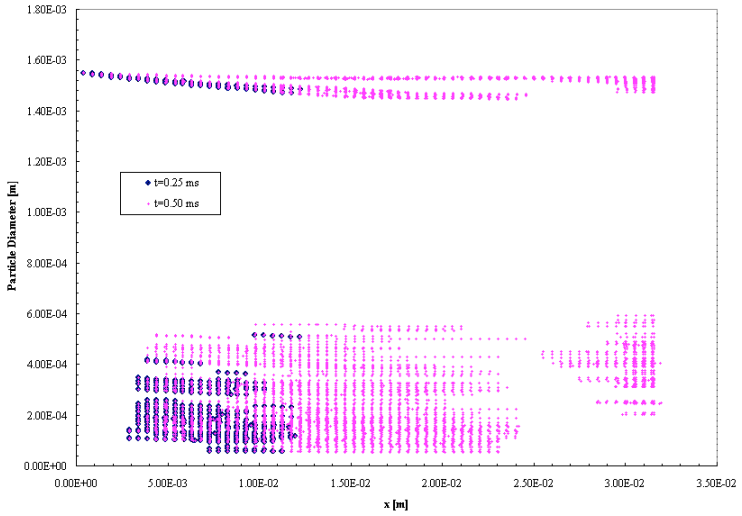

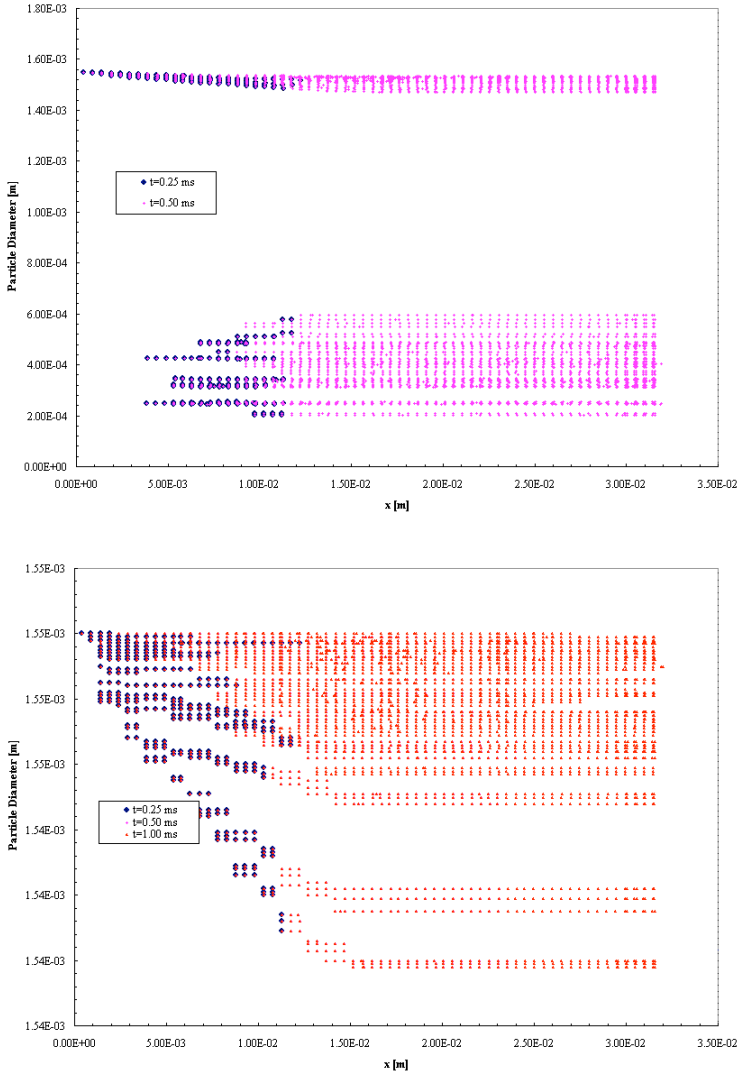

Figure 5.10. Variation of particle diameter along the centerline of the L-shaped cavity. Top graph is for B_0=0.12, center for 0.61 and bottom 3.05.

order of magnitude higher than for the other case. Also, it appears as if the particle count approaches asymptotically a maximum value that was not reached in the present study. This trend indicates the increased atomization created by the gas initially at rest.

More detailed information about the atomization patterns along the cavity centerline can eb inferred from Figure 5.10. The plots show the droplet size across the cavity as a function of the distance from the injection location. It is clear that for B_0=0.12 and 0.61 the injected droplets with the same diameter as the nozzle thickness, breakup into smaller droplets. However, the child droplets do not show a smooth variation in size but rather there is a region, between 1.55mm and 0.60 mm in which no particles appear to be. Obviously, this discontinuity in the droplet size distribution is a result of the assumption that the breakup is caused only by the fastest-growing wavelength. The characteristics of this discontinuity in particle size distribution are determined by the choice of B_0. Note that for B_0=3.5 no appreciable atomization occurs as it could have been predicted by looking at the Reitz theory.

The change in atomization patterns created by the different values of B_0 is evident in the cross sectional particle size distribution measured along line 1 and line 2 shown in Figure 5.11. The x-axis represents the vertical distance from the bottom wall of the closed cavity while the vertical axis represents the particle size at different injection times. For B_0=*0.12*, there is a noticeable atomization already at line 1 for all the injection times. As expected, the atomization decreases with increasing B_0 value. However, it appears as if the lateral spread of the particles is very similar for all the three cases. Also, the injection pattern appears clearly through the particle size distribution. In these calculations, three blobs of molten Magnesium were injected at the same time from the same injection location. However, two of the injected blobs had an opposite lateral component of velocity, calculated accordingly to the analysis conducted by Reitz (Reitz, 1987). One of the three blobs had only a longitudinal component of velocity. The concentration of particles with size of 1.55mm in the three vertical locations visible in all the plots is the result of such injection pattern. Also notice the lack of any measurable atomization along line 1 and 2 for the higher B_0 value. The same general comments for line 1 are valid for the particle size distributions along line 2 as shown in Figure 5.11. However, since line 2 is further from the injection location than line 1, there is a higher degree of atomization as well as a higher lateral spread than those observed at line 1 for all the cases. It is noteworthy the discontinuity of particle size distribution between the initial particle size, 1.55mm in diameter, and the largest breakup particle size given by the instability wave. As for line 1, atomization for B_0=3.05 at line 2 is virtually zero.

A qualitative view of the atomization process as described by the Reitz model is given by Figure 5.12. Here, the scaled size and the actual number of the parent and child droplets are shown. As discussed above, it is apparent that the child droplets do not form a continuous size distribution, but rather a large gap exist between the parent and child droplets.

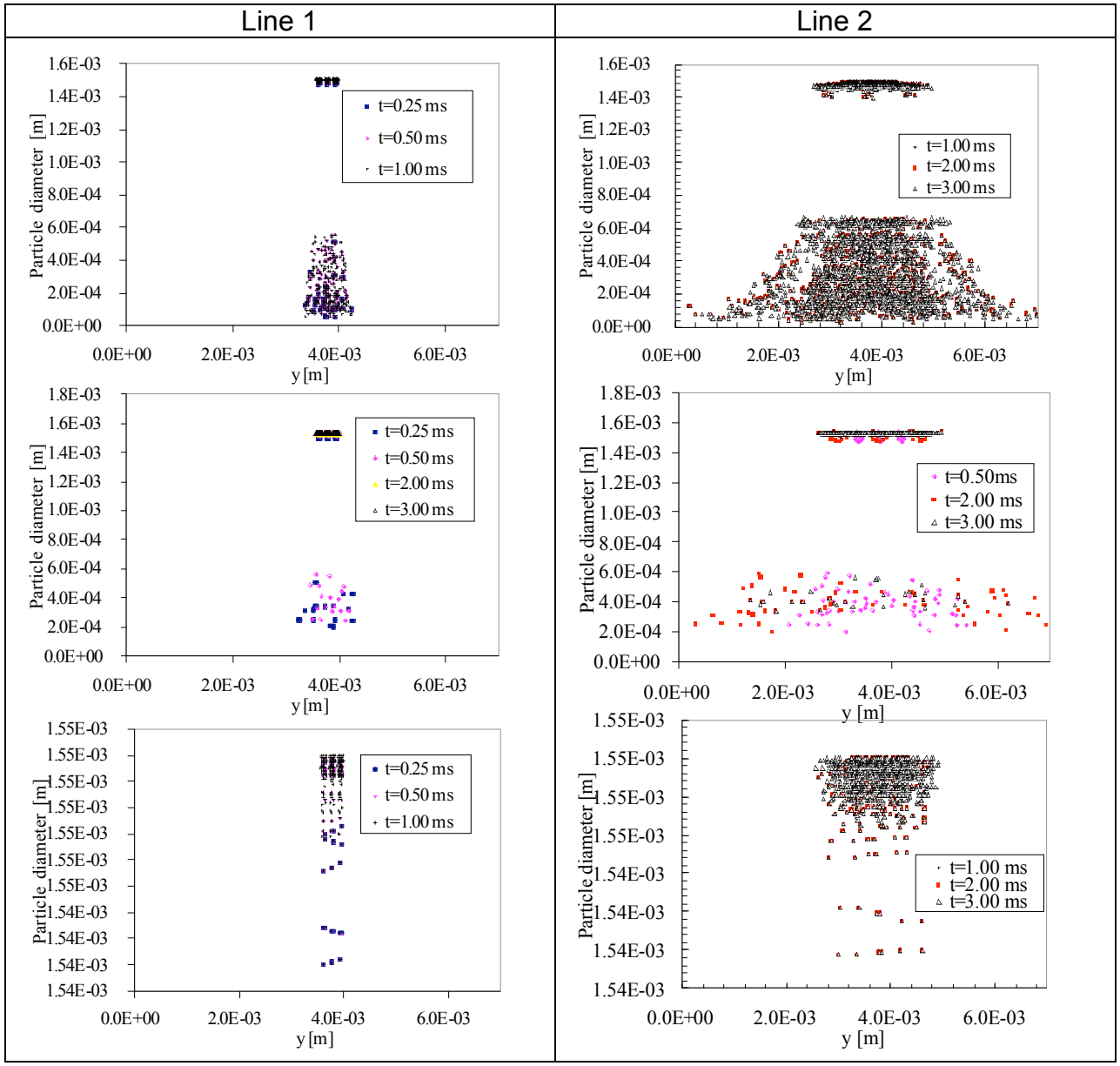

Figure 5.11. Variation of particle diameter across the channel at Line 1 and Line 2. Top graph is for B_0=0.12, center for 0.61 and bottom 3.05.

Figure 5.12. Visualization of particle breakup using the Reitz model. Injection speed=50 m/s, Mg into air, Initial particle diameter ($t=10^{-6}$ s) = 1.55 mm, $B_0=0.61$.

The same calculations were performed on a closed cavity with a 45deg inclined section for the standard B_0 and B_1 values of 0.61 and 10. The results are show in Figure 5.13

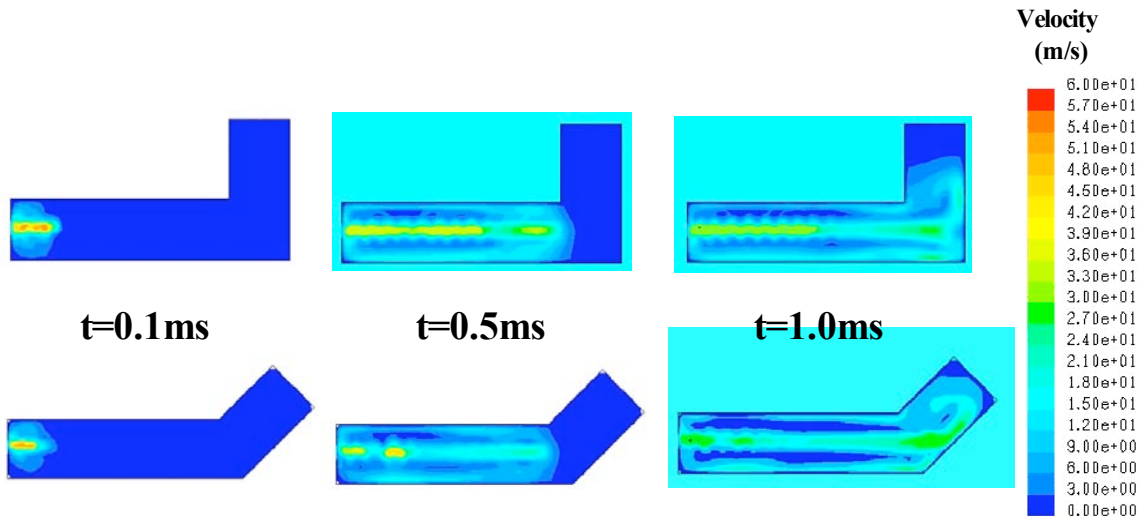

Figure 5.13. Effect of cavity geometry for the Reitz model. B_0 =0.61, B_1 =0.61. Contours show velocity magnitude.

In general, the Reitz model was not found to predict a credible atomization pattern. The atomization of the droplets occurs in discrete steps, the child droplet size being a strong function of the B_0 parameter. The B_0 parameter can be selected from experimental data for given injection conditions. However, it would appear that B_0 itself should probably be a non-linear function of the flow pattern and using a constant value does not allow for a realistic representation of the physics of the atomization process.

5.1.7 3D Calculations

Three dimensional open-cavity calculations were also performed using the Reitz model. The results are presented in
Figure 5.14 and Figure 5.15 for the injection of molten Magnesium into quiescent air with an injection velocity of 50 m/s through a gate 1.55mm thick. The 3D results show the same trend as the 2D results, with an intact sheet chore that penetrates deep into the open cavity while some dispersion can be observed to develop as the injection time increases. These calculations were not pursued further as the Reitz model did not appear to produce reliable atomization patterns.

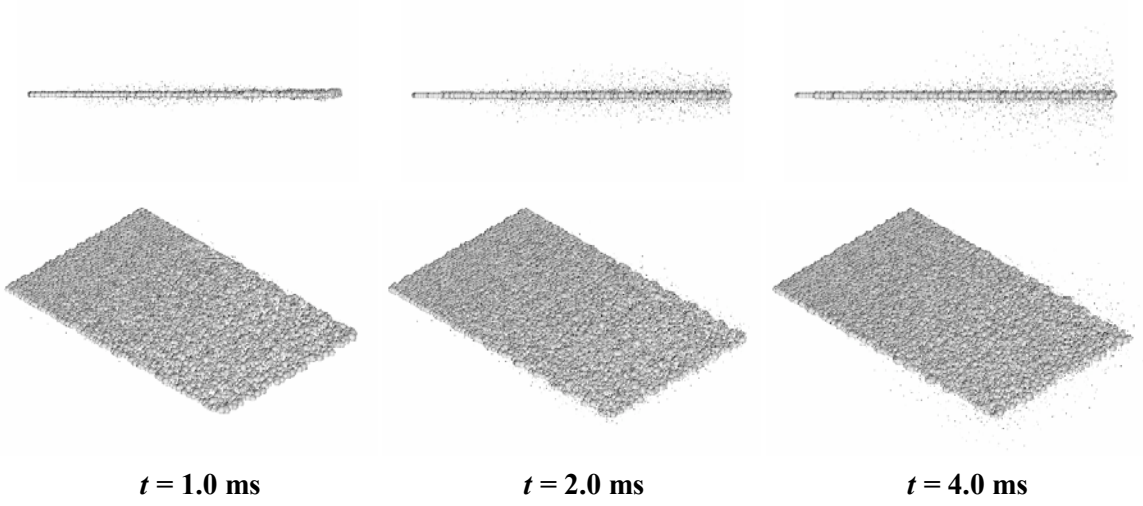

Figure 5.14. Sheet injection using the Reitz model into an open cavity.

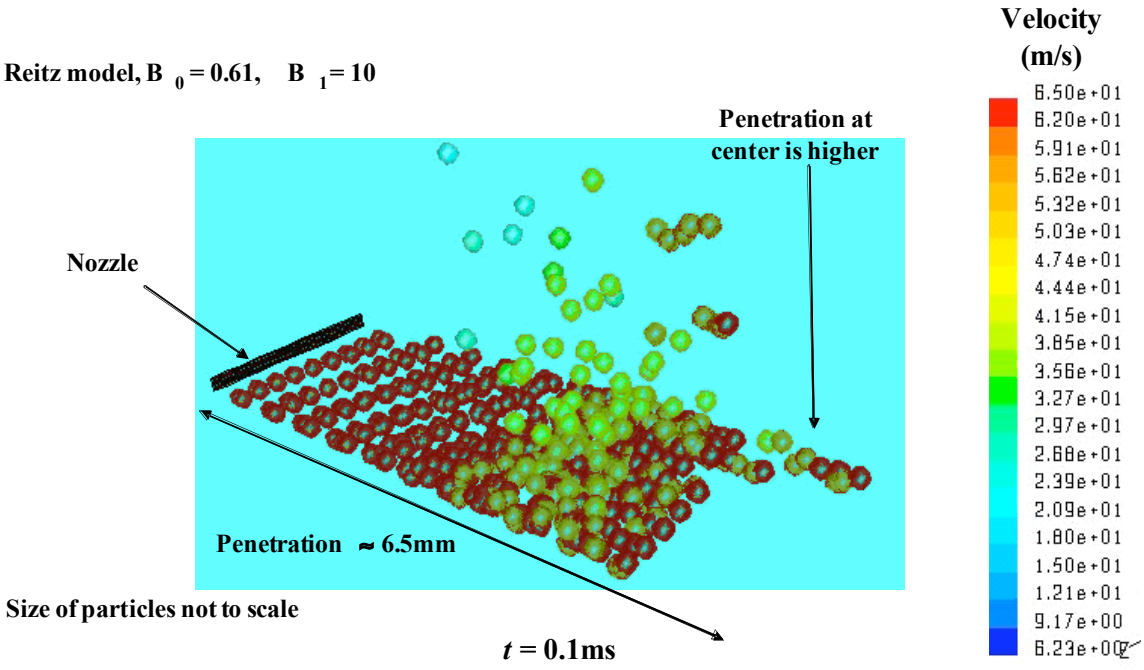

Figure 5.15. Sheet injection using the Reitz model into an open cavity.

5.1.8 VOF-type simulations

As for the discrete phase model, calculations were performed using Eulerian methods, here also called VOF-type methods for closed and open cavities. The Eulerian calculations can predict mold filling patterns, a capability that the discrete phase model does not have since it assumes a diluted phase. Further, VOF-type calculation, combined with a fine computational grid, can provide very accurate results about atomization and filling patterns. However, the computational costs associated with this approach are, at present, prohibitively high, and most of the industry-based research is performed using either Lagrangian methods, or Eulerian methods with coarser grid.

In the present work, we aimed at showing the capabilities and shortcoming of present-day modeling tools and software, when solving the two-phase flowfield into a closed and open cavity. Two software packages were considered for the Eulerian simulations: Fluent v 6.1 and OpenFoam. In the present calculations, we made use of two of the built-in multi-phase models: the Volume-Of-Fluid (VOF) model and the Mixture model. In the Mixture model the air and the injected material are simulated as inter-penetrating phases and the corresponding conservation laws are solved for each of the two phases (Wang et al., 1996). The Mixture model differs from classical VOF models in that it allows for the phases to be interpenetrating and to have a relative velocity at their interface.

Table 5.5. The governing equations for the VOF and Mixture models.

	VOF	Mixture Model
Continuity	N/A	$\frac{\partial \rho}{\partial t} + \nabla \cdot (\rho \mathbf{v}) = 0$ (5.20)
Momentum	$\frac{\partial \rho \mathbf{v}}{\partial t} + \nabla \cdot (\rho \mathbf{v}\mathbf{v}) = -\nabla p + \nabla^2 \left[\mu \mathbf{v} + \mu_T \mathbf{v}\right] + \rho \boldsymbol{g} + \boldsymbol{F}$ (5.21) Where $\boldsymbol{F} = \sigma_{ij} \frac{\rho r_i \nabla \alpha_i}{0.5(\rho_i + \rho_j)}$ $\boldsymbol{F} = \nabla \left(\sum_{i=1}^{n} \alpha_i \rho_i \mathbf{v}_{DR,i} \mathbf{v}_{DR,i} \right)$	
Energy	$\frac{\partial \rho E}{\partial t} + \nabla \cdot \left(\mathbf{v}(\rho E + p)\right) = \nabla \left[(k + k_T)\nabla T\right] + S$ (5.22)	
Volume Fraction	$\frac{\partial \alpha_i}{\partial t} + \nabla \cdot (\mathbf{v} \alpha_i) = 0$ (5.23)	$\frac{\partial \rho_i \alpha_i}{\partial t} + \nabla \cdot (\rho_i \alpha_i \mathbf{v}) = -\nabla \left(\rho_i \alpha_i \mathbf{v}_{DR,i}\right)$ (5.24)

The VOF model assumes that the two (or more) phases present in the computational domain are not interpenetrating, that is, a definite interface exists between the two phases. For this reason the surface tension is an important parameter in the VOF model as it determines the shape of the free-surface. In the present calculations, the interface between the liquid and the gas phases is calculated using the geometric reconstruction scheme of Youngs (Youngs, 1982). The volume fraction of phase *i* is denoted by α_i and, for continuity, the summation of the volume phases in each cell is unity. The VOF model

assumes that the two phases are moving with the same velocity, i.e. there is no shear at the interface between the two phases. On the other hand, the mixture model assumes that the two phases are interpenetrating and no definite boundary exists between them within a computational cell. Also, the mixture model allows the two phases to have different relative velocities, its value is given by the "slip velocity".
The governing equations for the two models are presented in the Table 5.5 side-by-side so as to highlight their differences.
In the table above, μ and μ_t represent the laminar and turbulent viscosity, k and k_t the laminar and turbulent thermal conductivity, σ_{ij} is the surface tension between phase i and phase j, r_i is the radius of curvature of the free surface, the total internal energy is given by $E=h-pv+v^2/2$, and $v_{DR,I}$ is the drift velocity of phase i. The drift velocity in the Mixture model is given by $v_{DR,i}=v_i-v$ i.e. the drift velocity is the difference between the velocity of phase i and the mixture velocity. However, since we do not know the i-phase velocity, we need to resort to modeling to quantify the drift velocity. One way to achieve this is to define the slip velocity between the two phases, $v_{ij}=v_i-v_j$ which is related to the drift velocity by $\mathbf{v}_{DR,i} = \mathbf{v}_{ij} - \sum_{k=1}^{n} \frac{\alpha_i \rho_i}{\rho} \mathbf{v}_{ik}$. The slip velocity is unknown and has to be modeled. In the present work, we use the slip velocity term to model a diffusion term for the volume of fluid. Notice that normally Fluent models the slip velocity v_{ij} algebraically as: $\mathbf{v}_{ij} = \frac{(\rho_j - \rho) d_p^2}{18 \mu_i f_D} \boldsymbol{a}$. In this equation f_D represents the drag force and a is an acceleration. The drag force and acceleration are then given by:

$$f_D = \begin{cases} 1 + 0.15\,\mathrm{Re}^{0.687} & \mathrm{Re} \le 1000 \\ 0.0183\,\mathrm{Re} & \mathrm{Re} \ge 1000 \end{cases} \qquad \boldsymbol{a} = \boldsymbol{g} - (\boldsymbol{v}\nabla)\boldsymbol{v} - \partial \boldsymbol{v} / \partial t \qquad (5.25)$$

More details regarding the numerical solver and the discretization schemes available in Fluent can be found in the code's user manual (Fluent ,2003).

In these calculations, turbulence modeling plays a crucial role, as the turbulent shear increases the atomization patterns. However, after several test runs, it appeared that Fluent could not properly predict the turbulent flowfield generated by the injection of a dense medium, such as water or molten Magnesium into air. On the other side, OpenFoam produced realistic results for the same case, as shown in Figure 5.16. OpenFoam offered the possibility of combining a Large-Eddy Simulation (LES) turbulence model with the two-phase flowfield. Fluent, is capable of modeling turbulence only through the k-ε eddy viscosity turbulence model when modeling two-phase flows.

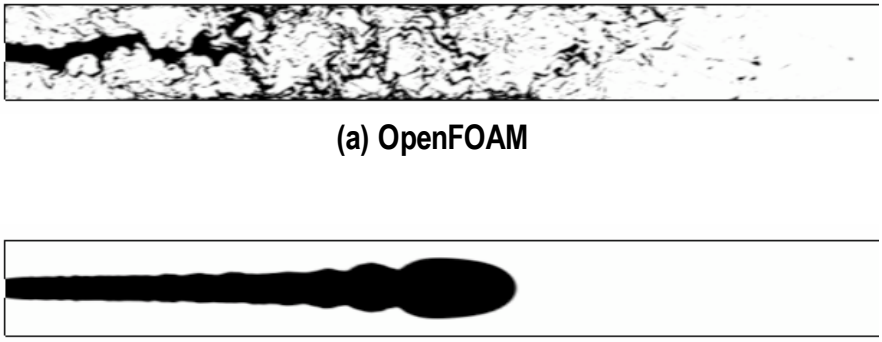

(a) OpenFOAM

(b) Fluent

Figure 5.16. Comparison of jet break-up using the VOF model implemented in OpenFoam with LES and the VOF model with the k-ε turbulence model implemented in Fluent. This picture is for t=1.0 ms.

Another goal of the present work is the development of a sub-grid model. A diffusive coefficient has been added to the Mixture model equation for the conservation of the volume of fluid. The diffusive coefficient acts in effect as a laminar diffusion term that "spreads" the volume of fluid into the surrounding cells. With this method, a VOF-type model should be able to capture the atomization process also when the cell size is coarse since the small-scale effects are not resolved but modeled.

5.1.9 2D L-shaped closed-cavity, Fluent Mixture model

Calculations with the Mixture model were run to simulate the filling pattern of the L-shaped closed cavity. The computational grid used for these calculations is the same as that for the discrete phase models shown in Figure 5.7. Because of the coarse grid used in these calculations, no atomization was observed, as it is evident by looking at the results shown in Figure 5.17. These results highlight the potential fro air entrapment and high-porosity in the mold region between the lower mold surface and the main injection stream.

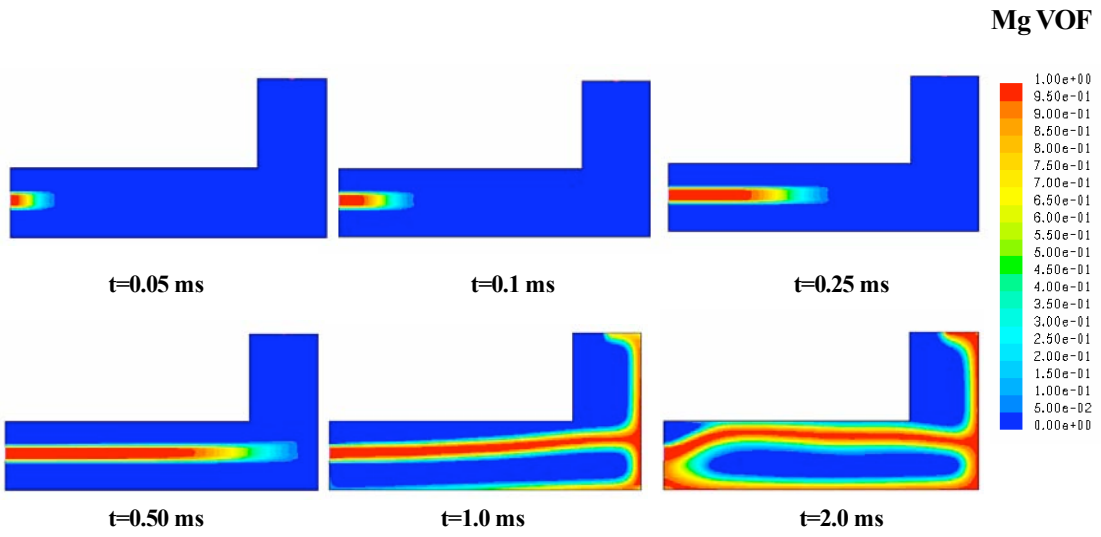

Figure 5.17. Results from the Mixture model in Fluent for the 2D L-shaped closed cavity. Magnesium in air, injection velocity of 50 m/s, no turbulence modeling.

5.1.10 Comparison of Fluent with OpenFoam Results, VOF simulations

These calculations were performed using the Mixture model implemented in Fluent. The calculations were performed to accomplish three primary goals:

1) Check the Mixture model implemented in Fluent and its capability of modeling jet breakup.
2) Compare the Mixture model results to those obtained through the Reitz model.

The first goal produced, at best, mixed results as no atomization has been observed when using the VOF model in Fluent. A 2D calculation of water injected into an open cavity with 50 m/s injection speed, no turbulence, showed jet instabilities at the gas-liquid interface but no breakup.

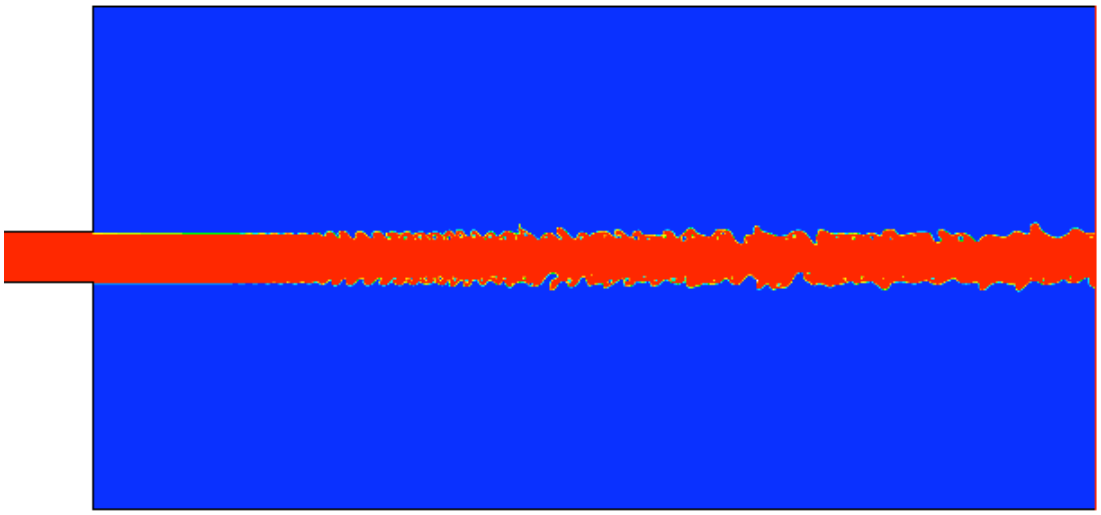

Figure 5.18. Results from the VOF model in Fluent. Axi-symmetric liquid jet in quiescent air.

Since the Fluent Mixture model did not predict any of the expected atomization patterns, another software package was tested using its VOF model. The chosen software is a free-ware called OpenFoam. Two preliminary calculations were run. One in an open cavity and a second one in a closed cavity. The results of the open cavity calculation are shown in Figure 5.19.

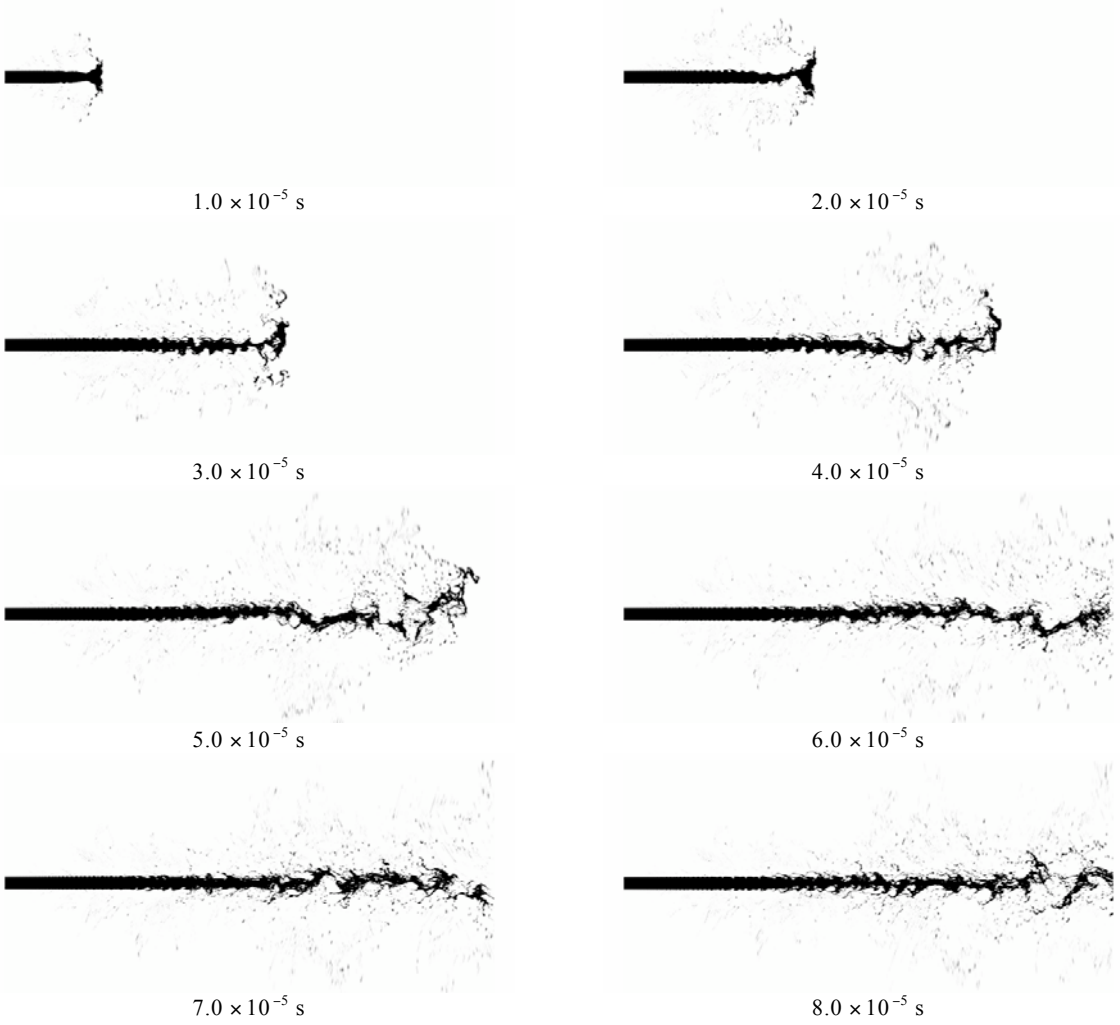

Figure 5.19. Results from the VOF model in OpenFoam. Liquid sheet injection in quiescent air.

The second goal lost its relevance as the Reitz model was found not to be appropriate for the prediction of the atomization patters.

5.1.11 Closed cavity, VOF model, Open Foam

Due to the encouraging results obtained with OpenFoam, the injection of a liquid into a quiescent gas was further analyzed using this software and its VOF model implementation. Turbulence was modeled using large eddy simulation (LES) model and the two-phase flow was modeled using volume of fluid (VOF) model with a relatively fine computational mesh. The simulation was able to capture the detail of the breakup process. The LES-VOF model is expected to help us correlate the operational conditions and the product quality.

These simulations made use of a combination of VOF and large eddy simulation (LES) following de Villiers et al., 2004. The detail of the model formulation is presented in (de Villiers, 2004), and only brief explanation of our simulation is given below.

We assumed that the flow is two-dimensional (2D), isothermal, and incompressible. The use of 2D model is justified by the 2D nature of the breakup of a liquid sheet (Lopez-Pages et al., 2004). The 3D effect may be important for the subsequent droplet formation; however, the 2D simulation at least provides us with a basic insight of the behavior of liquid metal inside the mold. Furthermore, the use of 2D model considerably reduces the computational time. We used a dual-processor PC for the simulation, and the computational time was about 4 days for the simulation of 1 ms with the time step $\Delta t \approx 1 \times 10^{-7}$ s. The size of our computational domain is 100 mm $\times$ 5 mm, and a gate (thickness, 1 mm) is located at the center of the left-hand side of the mold. The gate velocity is 50 m/s. The thermo-physical properties of magnesium at its melting point were used for those of the liquid phase. The ambient pressure is known to affect the breakup and atomization (Raffel et al., 1998). To consider the increase of air pressure during the casting process, the density ratio of $\rho_{liquid} / \rho_{air} = 80$ was used in our simulation. Under these conditions, Reynolds and Weber numbers based on the gate thickness and the gate velocity are Re = 64000 and We = 7000, ensuring the occurrence of breakup inside the mold. Since the purpose of this study is to demonstrate the capability of the LES-VOF model in simulating the breakup and atomization during HPDC, we chose these conditions.

Figure 5.20 shows the distribution of volume fraction of the liquid phase in the mold every 0.2 ms. Initially (t < 0.4 ms), the liquid jet, which is rather symmetric, enters to the mold in a continuous manner. The jet front is deformed and splits into small droplets, which flow backward. In addition, ripples on the surface of the liquid sheet are observed, which is qualitatively similar to the detailed photograph obtained by Taylor and Hoyt (Taylor et al., 1983). At 0.6 ms, sinuous (anti-symmetric) disturbances can be clearly seen. The sinuous disturbances are thought to play a major role in the breakup of a liquid sheet (Squire, 1953). The result indicates that a symmetric simulation cannot correctly predict the breakup behavior. The breakup of the liquid is observed at 0.8 ms. Interestingly, the breakup length (the distance between the gate and the breakup location) keeps decreasing after t = 0.8 ms. The breakup occurs just after the entrance to the mold at 1.4 ms, and a number of droplets are traveling inside the mold.

The LES-VOF model presented here can be extended to include heat transfer and solidification processes. It is expected that we will be able to use the LES-VOF model to study a HPDC process in detail.

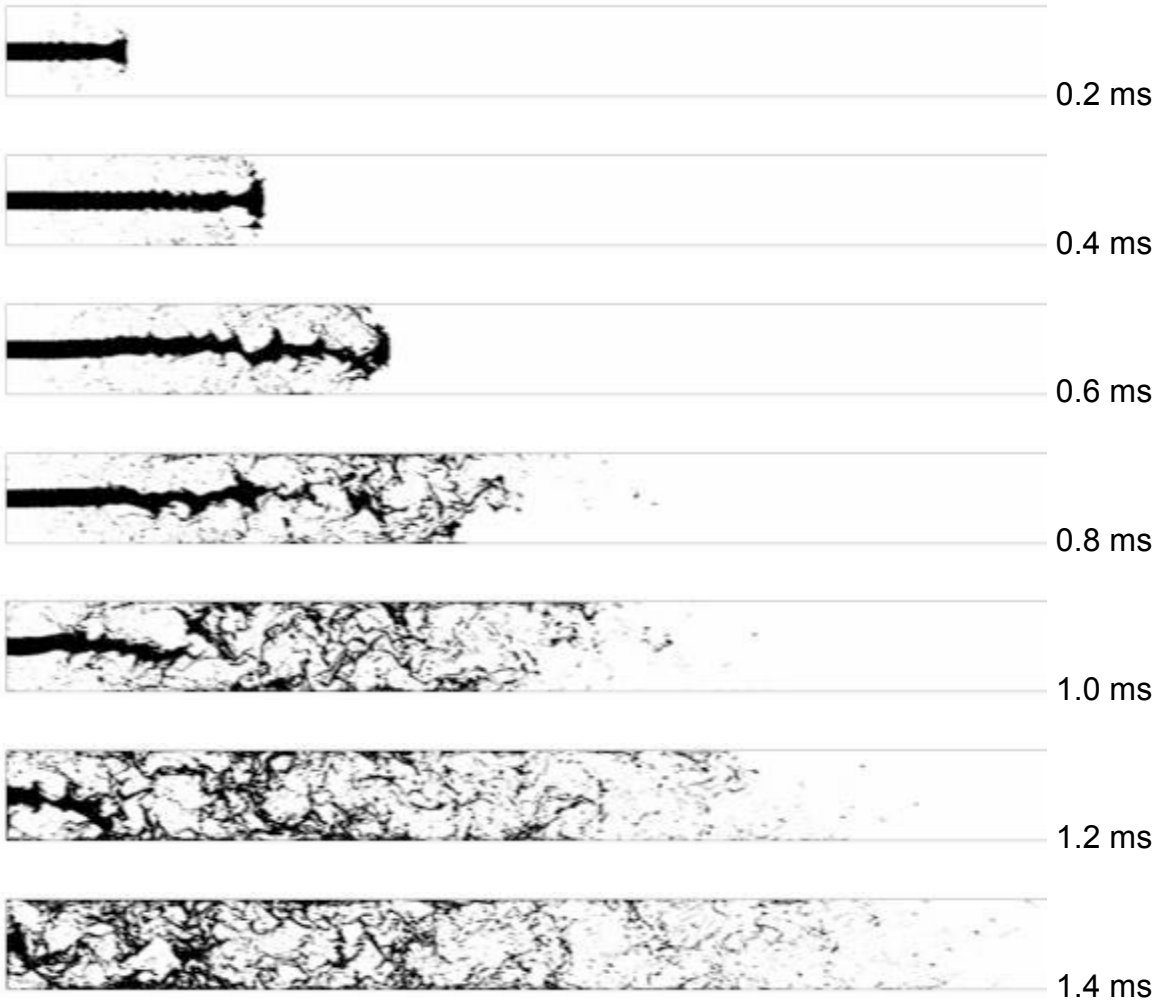

Figure 5.20. Jet break-up using the VOF model implemented in OpenFoam and LES turbulence model.

5.1.12 Subgrid scale Break-up model

A diffusive coefficient is added to the Mixture model equation for the conservation of the volume of fluid. The diffusive coefficient acts as a laminar diffusion term that “spreads” the volume of fluid into the surrounding cells. With this method, the mixture model should be able to predict the intensity of the atomization process also when the computational cell size is coarse. The modified transport equation for the volume of fluid in the Mixture model can be written as:

$$\frac{\partial \alpha_1}{\partial t} + \nabla \cdot \left(\mathbf{v} \alpha_1 \right) = -\nabla \cdot \left(\rho_1 D_B \nabla \alpha_1 \right) \tag{5.25}$$

where D_B is the breakup diffusion coefficient. The D_B coefficient can be set to a constant value or modeled as a sub-grid scale model. In the present work, D_B was set to two constant values, 1 and $1x10^4$ m^2/s, and the results so obtained were compared to the VOF results. Note that D_B can be modeled as a function of other local flow variables that can be correlated to the atomization pattern. This approach is currently being investigated in our computer model.

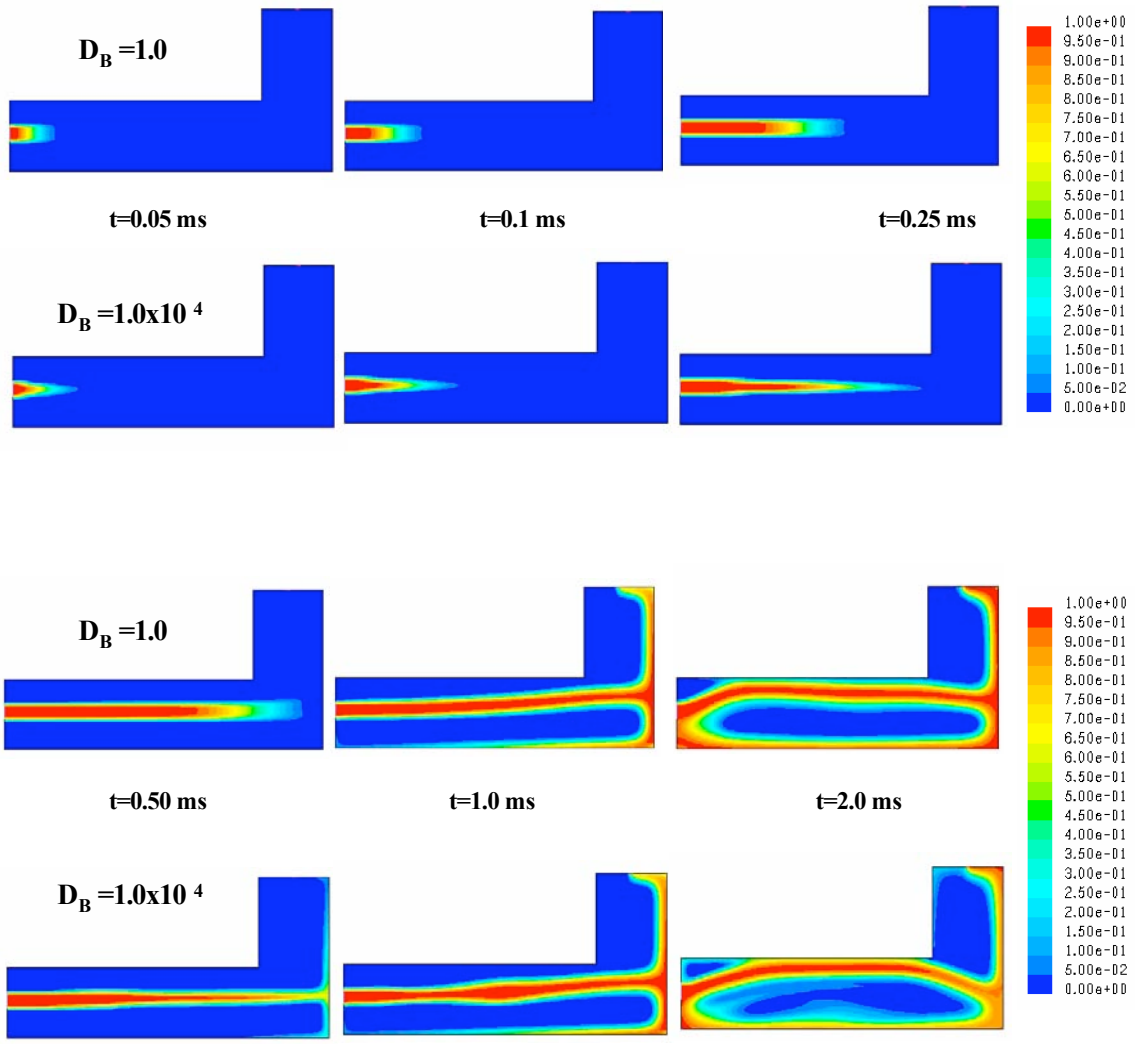

Figure 5.21. Results from the Mixture model in Fluent with variable diffusion coefficient

5.1.13 Subgrid model, 2D closed-cavity

In these closed-cavity calculations, the Mixture model was used in combination with the sub-grid scale break-up model. The injection conditions correspond to the injection of molten Magnesium into quiescent air. The gate is 1.55mm thick and the injection velocity is 50 m/s. The effects of changing the diffusion coefficient from 1 m^2/s to 10

m^2/s are compared in Figure 5.21. While the filling pattern is similar for the two cases, an increased dispersion of the liquid phase occurs in the case with the higher diffusion coefficient. The dispersion of the liquid phase corresponds to the intensity of the atomization process. Note that no detailed information about the atomization pattern, such as droplet size distribution and velocity, can be inferred form these calculations. Only bulk flow characteristics can be measured.

5.1.14 Subgrid model, open cavity

For the open cavity runs, water was injected vertically into q quiescent air atmosphere. In order to keep the comparison simple and reduce any grid-dependency effect, the computational grid used in these calculations is a structured two-dimensional grid. The test case simulates the two-dimensional injection of water through a slit nozzle (the gate) into an open cavity at standard atmospheric conditions. The structured grid is finer close to the injection location and it progressively becomes coarser away from the jet. As shown in Figure 5.22, the injector is 0.5mm

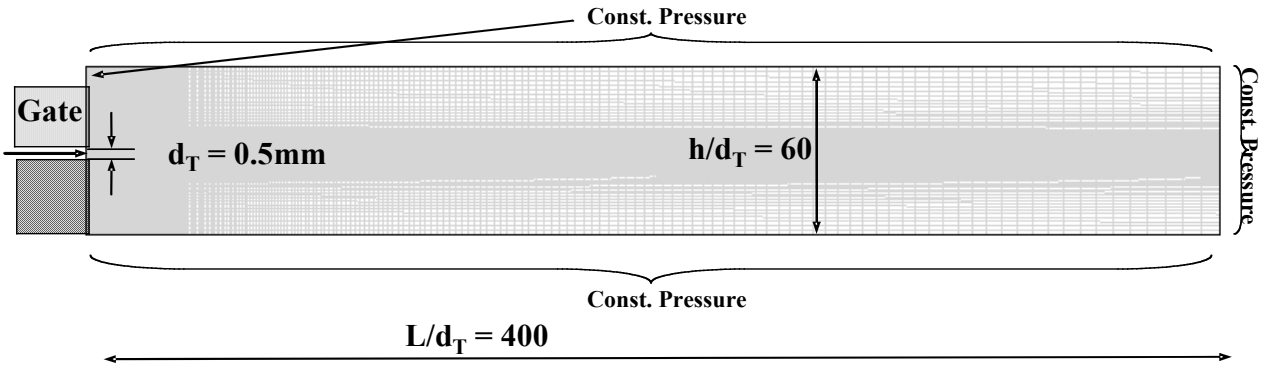

Figure 5.22. Computational grid for the open cavity simulations

in height and the computational domain is 400 gate-height long and 60 gate-height wide. The acceleration of gravity
vector points in the same direction as the injection velocity, i.e. in Figure 5.22 it points horizontal to the right. The domain is composed of 50,100 rectangular cells, with clustering around the injection location as shown in **Error! Reference source not found.** (a). For the Mixture model, a grid with the same topology as that of the VOF model was used. However, the number of cells was reduced to 7,670 since the sub-grid model would take care of the prediction of the atomization. The grid in the region around the injector is shown in **Error! Reference source not found.** (b) where the difference in grid-fineness between the two meshes is evident.
Constant pressure boundary conditions are imposed along the three sides representing the room environment. On the injection side of the computational domain, the nozzle

solid surface is simulated with wall boundary conditions while a velocity boundary condition is imposed at the injection location. The injected liquid is water at standard room conditions with bulk velocity of 25m/s. Due to the comparative nature of the present study, turbulence was not included in

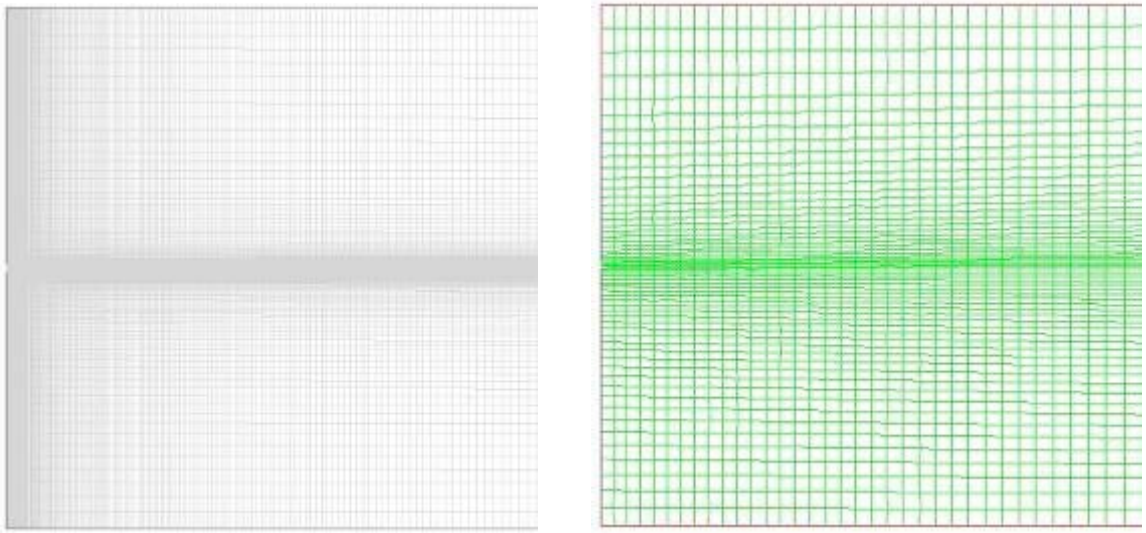

(a) (b)

Figure 5.23. Computational grid for the closed cavity simulations. (a) VOF simulations, (b) Mixture model with sub-grid atomization model.

the present calculations. The gaseous phase is considered to be barotropic, i.e. its density is a function of static pressure only. The liquid phase is assumed to be incompressible.

The results obtained from the VOF and Mixture model simulations are shown in Figure 5.24. The figure shows the volume-fraction of the injected water for injection times of 0.2, 0.5, 1.0, and 2.0 ms, with the injection starting at t=0 ms. The VOF model results are in the first column while the other two columns are for the Mixture model with sub-grid atomization modeling with a diffusion coefficient of 1 and 10^4 m^2/s, respectively. From the mappings of the water volume fraction it is evident that the VOF model combined with a very fine mesh can qualitatively predict the breakup and atomization phenomena of the liquid jet. For t=0.2 ms, the liquid jet presents an injection front where most of the breakup occurs due to the buildup of dynamic pressure in the quiescent gas. This is evidenced by the flat injection front that is sheared laterally, away from the jet centerline, by the aerodynamic forces. For t=0.5 ms wave instabilities are visible on the jet core behind the injection front. As expected, the instabilities grow with time and, for t=2.0 ms, they cause the jet to breakup. Notice the range of length-scales over which the breakup droplets are produced. The Mixture model (center and right column of Figure 5.24) is not able to predict the detailed breakup mechanism and to reconstruct the liquid-gas interfaces, as expected. The Mixture model is aimed at producing representative information about the local atomization pattern and intensity. The Mixture model with a diffusion coefficient of 1 m/s over-predicts the jet penetration length for all

the time steps. As the diffusion coefficient is increased to 10^4 m^2/s and the diffusion of the water phase is increased, the jet penetration length is decreased, thus making it more similar to that of the VOF model, as expected. For a particular case, it is possible to adjust the D_B coefficient so that the Mixture model correctly predicts the penetration length. However, this ad-hoc coefficient adjustment would destroy any predictive capability of the model. Ideally, the diffusion coefficient D_B should be self-adjusting according to the injection conditions (Reynolds and Weber number based on injection conditions and gate thickness) and the local flow conditions. However, also with the higher value of the diffusion coefficient, the Mixture models are not able to predict the droplet breakup and dispersion that is visible in the VOF model results. This is the result of the lack of an interface between the two phases and the loss of some of the basic physics that govern the jet breakup, first of all the propagation of surface instabilities due to the coupling of the aerodynamics forces with the surface tension and jet viscosity.

The above comments are confirmed by the analysis of the volume fraction of water at discrete locations along the domain. Figure 5.25 shows the distribution of the water fraction at two transverse locations downstream of the injection location, Line 1 and Line 2, at x=10 mm and x= 25mm downstream of the injection, respectively. The third column in Figure 5.25 shows the volume of water distribution along the longitudinal centerline of the gate. At t=0.2 ms, no liquid has reached Line 1 according to the VOF model and the Mixture model with $D_B=10^4$ m^2/s. However, as seen in the mappings of Figure 5.24, the Mixture model with the lower diffusion coefficient exhibits a longer penetration length, thus predicting the presence of water at Line 1 at t=0.2 ms. This is confirmed also by looking at the water distribution along the domain centerline in the right column of Figure 5.25 for t=0.2 ms where the Mixture model with the lower diffusion coefficient shows the higher penetration. Notice that at t=0.2 ms, no liquid has reached Line 2. At t=0.5 ms, again the Mixture model with the lower diffusion coefficient predicts the presence of water across Line 2 while the other two model show a shorter jet penetration length. At Line 1 and t=0.5 ms, both Mixture models predict the same water distribution. This distribution is somewhat different from that of the VOF model, the latter predicting a slightly narrower jet thickness with an intact core (volume of water equal to 1.0). As the injection proceeds, at t=1.0 ms, the gas is set in motion by the moving liquid thus reducing the aerodynamic shear between the two phases. This is important especially for the Mixture model as the interaction between the two interpenetrating phases is given by the slip velocity between the two phases. The effect of a lower shear is clear in the plot for t=1.0 ms and Line 1 where, differently from the plot for t=0.5, the Mixture models predict an almost-intact jet core, in agreement with the VOF model. However, the distribution of the liquid phase along Line 2 highlights the difference in prediction when the capability of predicting the phase interface is present: both Mixture models predict a broken jet core along the jet centerline (volume of water less than one) with some diffusion, while the VOF model shows the presence of only water droplets far from the centerline (the volume-of-water spikes at y=1.45, 1.55 and 1.65mm), preceding the intact jet core.

If we look at the centerline plots in the right column of Figure 5.25, the difference between the three models appears clear. The VOF model predicts a well-defined intact jet core proceeding at a speed close to the value used for the injection. The two Mixture models fail to predict a well-defined jet front, with both models showing a gradual transition from the jet core (volume of water equal to 1.0) to the undisturbed gas (volume of water equal to 0.0). Also, Figure 5.25 highlights, the effect of increasing the

diffusion coefficient for the sub-grid breakup model; the Mixture model with higher diffusion coefficient (a) predicts a shorter penetration length for all the time injection times and (b) it shows an injection front that is better defined.
At t=2.0 ms, the Mixture models predict almost identical volume-of-water distribution along Line 1; this can be explained by the established flow in the gas phase that creates minor shear with the liquid phase, thus reducing the diffusion of the phases.
At Line 2 the flow is not developed as at Line 2, and the solutions form the two Mixture models differ. The volume-of-water along the centerline highlights the discontinuity of the flowfield as predicted by the VOF model. For a location downstream of x=30mm, the core of the jet breaks up and liquid particles are dispersed while continuing to move downstream. Again, the Mixture models cannot simulate this process; but the Mixture model with the higher diffusion coefficient predicts the jet penetration very close to the VOF model, at x=60mm.

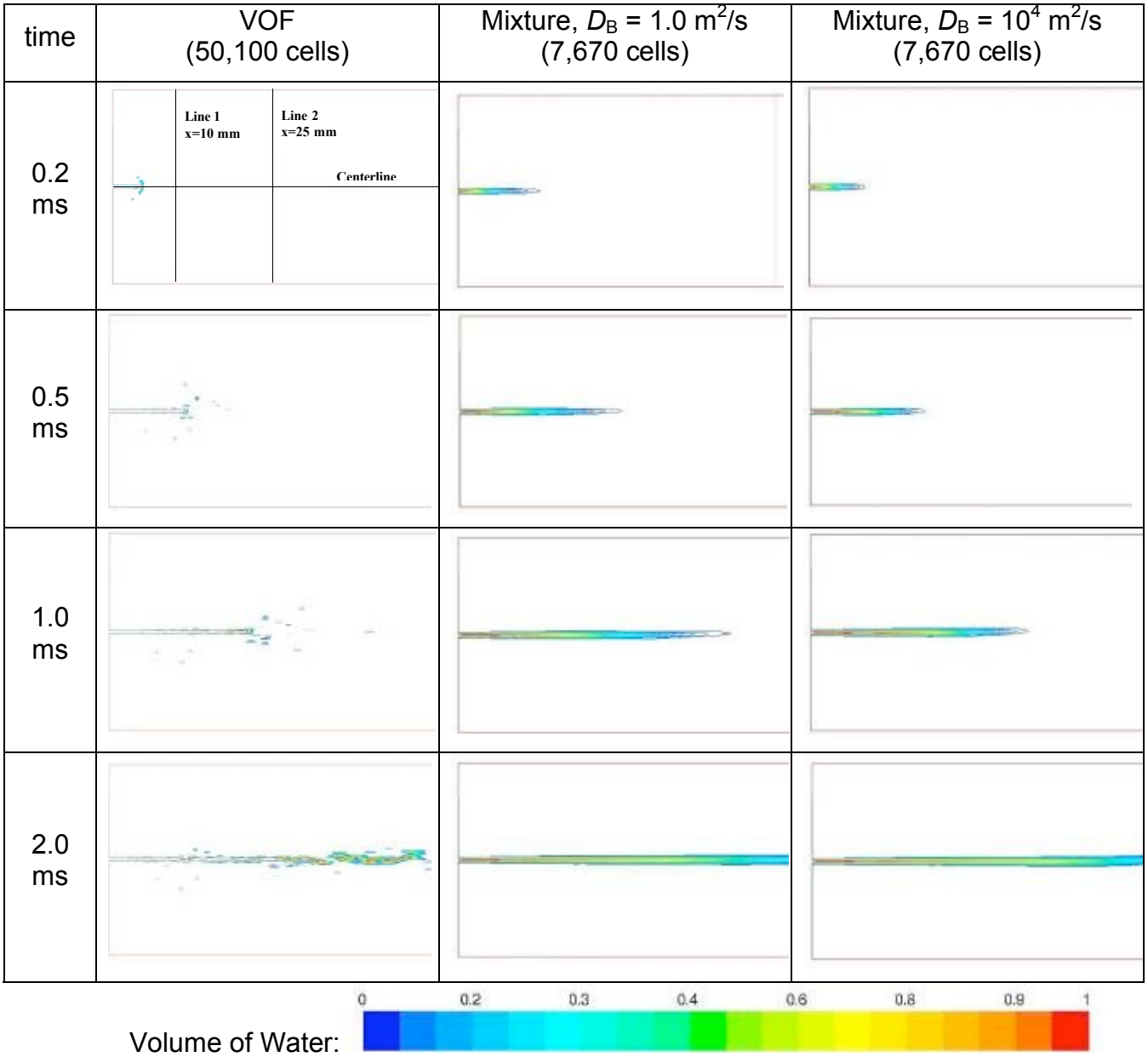

Figure 5.24. Comparison of the results for the three tested cases: the colors represent the volume-of-fluid for the injected water. Line is located at x=10 mm and Line 2 at x= 25 mm. The dimensions of the visible domain are approximately 50x30 mm.

While the Mixture models with a constant diffusion coefficient fails to accurately predict the instantaneous atomization patterns captured by the VOF model, the Mixture computations showed promising results. Also, while the Mixture results do not match the instantaneous VOF results, better agreement would be obtained when comparing time-averaged results.

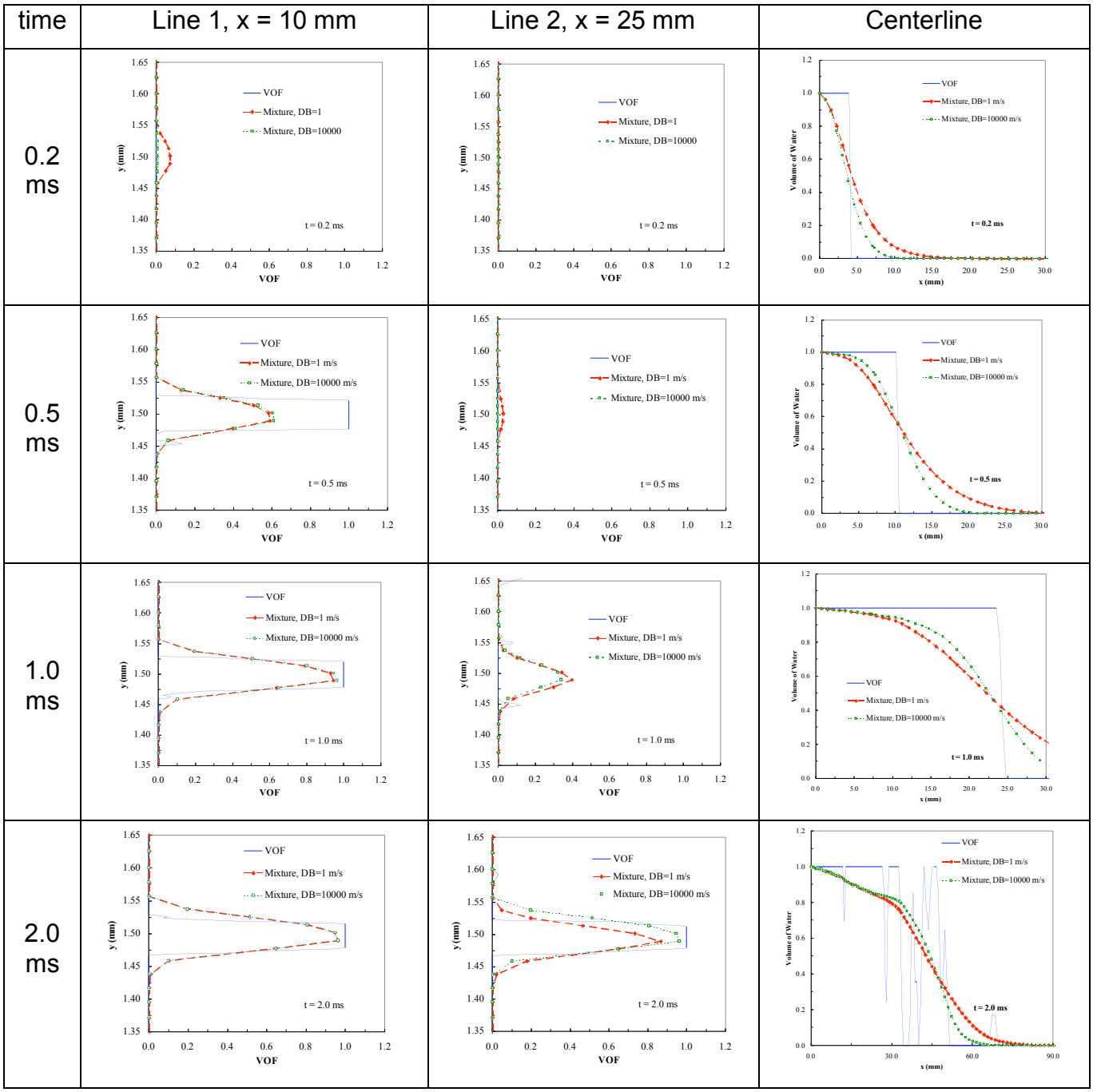

Figure 5.25. Comparison of the results for the three tested cases: line plots for the three simulations at different injection times.

Considering the computational expense, the Mixture calculations were three orders of magnitude less expensive than the VOF computations. One iteration of the Mixture model takes approximately 0.1s on a single HP Superdome CPU to run. For the VOF model it takes approximately 1.0s. The convergence criteria for the two models and the number of inner iterations per time step (400) are the same. The Mixture models show better stability and can be run with a time step of 10^{-5}.s, compared to 10^{-7} s for the VOF model.

5.3 REFERENCES

T. Arai and H. Hashimoto, “Disintegration of a thin liquid sheet in concurrent gas stream,” (Paper presented at 3rd International Conference on Liquid Atomization and Spray Systems, London, 1985), VIB/1/1-7.

P. Cleary et al., “Flow modelling in casting processes,” *Applied Mathematical Modelling*, 26 (2002), 171-190.

P. Cleary et al., “Modeling of cast systems using smoothed-particle hydrodynamics,” *JOM*, 56 (2004), 67-70.

P. Cleary, J. Ha, V. Ahuja, “High pressure die casting simulation using smoothed particle hydrodynamics”, *International Journal of Cast Metals Research (UK)*,12 (6) (2000), 335-355.

Fluent Users Manual, Version 6, (Published by Fluent Inc., Lebanon, NH, 2003).

R. P. Fraser et al., “Drop formation from rapidly moving liquid sheets,” *AIChE Journal*, 8 (1962), 672-680.

M. I. Hassan et al., “Flow structure of a fixed-frame type fire whirl,” *Proceedings of The International Association for Fire Safety Science*, 8 (2005), in press.

E. A. Herman, J.F. Wallace, and A.A. Machonis, *Copper alloy pressure die casting* (International Copper Research Association, Inc., 1975), Chap. 4.

C. W. Hirt and B. D. Nichols, “Volume of Fluid (VOF) Method for the Dynamics of Free Boundaries”, *Journal of. Computational. Physics*, 39 (1981), 201-225.

A.H. Lefebvre: *Atomization and Sprays*, Taylor & Francis, 1989, Chap. 2.

S.P. Lin, Breakup of *liquid sheets and jets*, (Cambridge University Press, 2003).
S. P. Lin, R. D. Reitz, “Drop and spray formation from liquid jet”, *Annual Review of Fluid Mechanics*, 30(1998), 85-105.

E. López-Pagés, C. Dopazo, and N. Fueyo, “Very-near-field dynamics in the injection of two-dimensional gas jets and thin liquid sheets between two parallel high-speed gas streams,” *Journal of Fluid Mechanics*, 515 (2004), 1-31.

K. Nomura, S. Koshizuka, Y. Oka, H. Obata, “Numerical analysis of droplet breakup behavior using particle method”, *Journal of Nuclear Science and Technology*, 38 (12) (2001), 1057-1064.

Y. Pan and K. Suga, “Simulation of liquid jet breakup by the level set method,” (Paper presented at 9th International Conference on Liquid Atomization and Spray Systems (ICLASS 2003), Sorrento, Italy, 12 July 2003).
Pan, Y., Suga, K. “Computation of laminar liquid pinch-off jets by the level set method”, *Transactions of the Japan Society of Mechanical Engineers, Part B (Japan),* 15 (6) (2003), 1321-1326.

M. Raffel, C. Willert, and J. Kompenhans, *Particle Image Velocimetry* (Springer, 1998).

R. D. Reitz, Mechanisms of Atomization Processes in High-Pressure Vaporizing Sprays. *Atomization and Spray Technology*, 3 (1987), 309-337.

R. D. Reitz and F. V. Bracco, Mechanism of Atomization of a Liquid Jet. *Physics of Fluids.*, 26(10), 1982.

R. D. Reitz and R. Diwakar, Structure of high-pressure fuel sprays, SAE Paper 870598, 1987.

W.A. Sirignano, *Fluid dynamics and transport of droplets and sprays*, (Cambridge University Press, 1999).

H.B. Squire, “Investigation of the instability of a moving liquid film,” *British Journal of Applied Physics*, 4 (1953), 167-169.

J.J. Taylor and J.W. Hoyt: *Exp. Fluid.*, 1983, vol. 1, pp. 113–120.

W. Thorpe, V. Ahuja, M. Jahedi, P. Clearly, J. Ha, N. Stokes, “Simulation of Fluid Flow Within the Die Cavity in High Pressure Die Casting Using Smooth Particle Hydrodynamics”, (Paper T99-014, presented at the World of Die Casting conference, Cleveland, OH, USA, 1999).

E. de Villiers, D. Gosman, and H. Waller: in *6th International Symposium on Diagnostics and Modeling of Combustion in Internal Combustion Engines (COMODIA 2004)*, Yokohama, Japan, 2004.

D. L. Youngs., “Time-Dependent Multi-Material Flow with Large Fluid Distortion”, *Numerical Methods for Fluid Dynamics*, ed. K. W. Morton and M. J. Baines, (Academic Press, 1982).

C.Y. Wang, P. Cheng, “A multiphase mixture model for multiphase, multicomponent transport in capillary porous media. I. Model development”, International Journal of Heat and Mass Transfer, 39 (17) (1996) 3607-3617.

C.Y. Wang, P. Cheng, “A multiphase mixture model for multiphase, multicomponent transport in capillary porous media II. Numerical simulation of the transport of organic compounds in the subsurface”, International Journal of Heat and Mass Transfer, 39 (17) (1996), 3619-3632.

6 Measurement of Heat Flux at Metal-Mold Interface during Casting Solidification

ABSTRACT

In this paper, the heat transfer at the metal-mold interfaces is investigated using a sensor for the direct measurement of heat flux. The heat flux sensor (HFS) was rated for 700°C and had a time response of less than 10 ms. Casting experiments were conducted using graphite molds for aluminum alloy A356. Several casting experiments were performed using a graphite coating and a boron nitride coating. The measurement errors were estimated. The temperature of the mold surface was provided by the HFS while the temperature of the casting surface was measured using a thermocouple. Results for the heat transfer coefficients were obtained based on measured heat flux and temperatures. Four stages were clearly identified for the variation in time of the heat flux. Values of the heat transfer coefficient were in good agreement with data from previous studies.

6.1 INTRODUCTION

The heat capacity of the mold material and thermal resistance at mold surfaces affect the alloy solidification and ensuing microstructure. The computational analysis of heat transfer and solidification of casting processes depends on materials properties, process parameters, and the heat transfer conductance between metal and mold (Ho and Pehlke, 1983). Unlike material properties used in casting processes, the heat transfer conductance at metal-mold interface is time dependent. The heat transfer at the metal-mold interface plays an important role especially for permanent mold casting, die casting, continuous casting, and squeeze casting processes, in which high thermal diffusivity of mold materials are used. At initial times when the metal contacts the mold, the thermal resistance posed by the metal-mold interface is lowest. Then, the thermal resistance decreases due to the appearance of an air gap between mold and casting as the casting contracts from the mold surface. The factors affecting the interfacial thermal resistance include the thermophysical properties of the contacting materials, casting and mold geometry, the roughness of the mold contacting surface, mold coatings, contact pressure, metal superheat, and initial temperature of the mold. In most studies, the interfacial heat transfer during solidification is quantified in terms of a heat transfer coefficient (HTC), h, which is given by the following relationship:

$$h\left(q'',T_C,T_M\right)=\frac{q''}{T_C-T_M} \tag{6.1}$$

where q'' is the heat flux through the interface. T_C and T_M are the surface temperature of the casting and mold, respectively. One of the most important parameters used in the analysis of casting solidification is the heat transfer coefficient at the metal-mold interfaces. Most programs in casting solidification have tasks for estimating the HTC. All previous studies on interfacial heat transfer coefficients have been based on indirect methods for estimating the heat flux that employed either inverse heat transfer analysis procedures or instrumentation arrangements to measure temperatures and displacements near the metal-mold interface (Krishnan and Sharma, 1996; Lee et al. 1998; Santos et al., 2001; Souza et al. 2004).

One way to estimate the HTC was based on the assumption that the interfacial thermal resistance is mainly due to conduction through the air gap (Engler, 1973). The air gap data was estimated by measuring the displacement of the mold surface and displacement of the casting surface. In this approach, the HTC is available only after the air gap forms. Values for the HTC before the air gap forms can only be obtained by extrapolation. Next, a series of models for the evolution of HTC were proposed. The most comprehensive models account for different phenomena that occur at solidifying interfaces, such as the surface roughness and the actual area of contact, which is a fraction of the overall surface area (Ho and Pehlke, 1984; Trovant and Argyropoulos, 2000). Representative methods for determining HTC for aluminum alloy castings is presented in Table 6.1.

Table 6.1 Heat transfer coefficients for aluminum alloy castings

HTC [W/m^{2}K]	Geometry	Alloy	Mold	Coating	Method	Dependent variables	Reference
700-200	Plate	A356	Bonded sand	N/A	Inverse	t	Hwang et al. (1994)
3000	Tube	A356 (Al, Al-Si)	Die steel	Graphite	Inverse	t	Kim and Lee (1997)
3000	Cylinder	A356	copper	N/A	Inverse	t, T	Ho and Pehlke (1983)
2000 3500	Cylinder	A356	graphite copper		Interpolation	T, a_g	Trovant and Argyropoulos (2000)

a_g – dimension of air gap between metal and mold, t is time.

The heat flux at the interface can be evaluated based on thermal gradient and thermal conductivity, k, as:

$$q'' = -k\left.\frac{\partial T}{\partial x}\right|_{\text{at interface}} \tag{6.2}$$

As seen from Equations 6.1 and 6.2, the thermal gradient and surface temperatures are used to determine h. In order to determine the temperature gradient, thermocouple location must be known also. Experimental setups for direct measurement of surface temperatures and temperature gradients are limited by the size and shape of the mold surface. Thus, post-processing of the experimentally measured temperature, T_{exp}, is required in order to estimate h (Table 6.2).

Table 6.2 Methods for estimating the heat transfer coefficient.

Method	Casting configuration	Experimental setup	Computations	Advantage/limitations
Interpolation	simple	thermocouples must be placed near each other and close to interface	$\partial T/\partial x\|_{\text{interface}}$, T_C and T_M from interpolation	Simple post processing/Low accuracy since thermocouple placement or assumed temperature profile
Inverse analysis	plates, cylinders	Thermocouples in the casting and mold	parameter estimation to minimize T_{comp}-T_{exp}	Computational efficient/2D analysis
Inverse analysis	Complex 3D geometries	thermocouples	parameter estimation to minimize T_{comp}-T_{exp}	Accurate/ computationally expensive 3D analysis

Usually, HTC is found by performing inverse heat transfer analysis. The inverse heat transfer analysis provides accurate results provided that the thermocouples can be placed in the cavity close to the mold surface, the accuracy increasing with the proximity of thermocouples to the surface. There are several factors that limit the temperature measurement for estimating HTC:

(1) the experimental arrangement of thermocouples in the cavity might alter the metal convection, heat transfer, and solidification.

(2) the thermocouple fixtures, which are necessary to either increase the stiffness of thermocouple or hold the thermocouple at fixed locations, may alter the heat transfer in the mold.

(3) due to geometric considerations, it is not possible to place two or more thermocouple close to the mold interface.

(4) the thermocouples in the metal cavity move according to loads applied to them and their stiffness. In this case, the location of the thermocouples is time dependent and almost impossible to measure.

(5) when there is significant metal convection or high pressure applied, the thermocouple may undergo significant deformation and may not survive the process.

(6) in conditions where solidification occurs at a fast rate, the experimental thermocouple data is plagued by effects due to the thermocouple response time. In these conditions, the temperature data for this highly transient phenomenon could be very different from the actual measured temperature, precluding the use of inverse analysis techniques. For high cooling rate conditions, the analysis must take into account the thermocouple response time (Sabau and Viswanathan, 2003).

In order to avoid cumbersome analysis of the data, such as performing inverse heat transfer analysis or accounting for the thermocouple response time, a sensor was used in this study for the direct measurement of heat flux. To the best of our knowledge, this study is the first attempt to use this type of sensors to casting processes. The applicability of this type of sensor to casting processes was assessed.

6.2 CASTING EXPERIMENTS

An HFM-8E/H heat flux sensor, which was supplied by the Vatell Corporation, was used to acquire data on heat flux and surface temperature. The heat flux sensor was embedded in the mold. Information regarding the heat flux sensor was supplied by the manufacturer and was included in Chapter 4 of this report. A data acquisition provided by Dataq Instruments, Inc. was used to obtain data at a sample rate of 60 Hz.

The graphite mold had the following dimensions: 10.5cm height, 7cm width, and 3.8cm. The thickness of the mold wall was 1.4cm. The pouring cup had a height of 2cm and a taper of 150. The plate dimensions, excluding the pouring cup, were approximately 7x4x1 cm. A hole was drilled into the mold wall to mount the sensor in such a way that its surface was flushed with that of the mold (Figure 6.1). The center of the sensor was positioned at approximately 4.8cm from the bottom surface of the mold. A thermocouple was placed in the casting cavity such that after metal pouring it stays on the casting surface and near the sensor. Pictures of the thermocouple and sensor marking on the

casting surface are shown in Figure 6.2. The pictures were magnified such that the area of the sensor surface is approximately the same. Due to surface tension effects, the metal did not wet the thermocouple wires and the thermocouple junction is visible. The pictures show that the thermocouple junction is right at the interface between metal and mold.

(a) 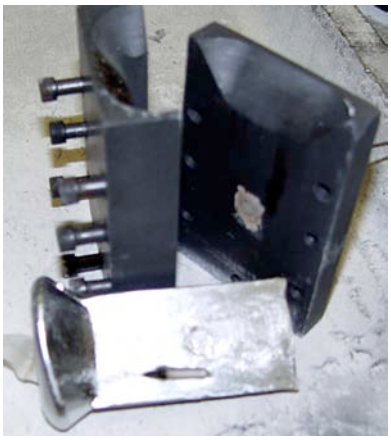 (b) 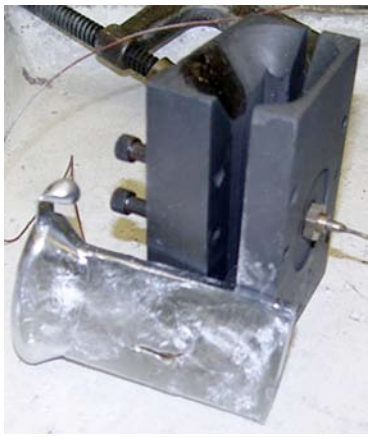

Figure 6.1 Pictures showing casting, graphite mold, placement of thermocouple at casting interface, and heat flux sensor.

(a)  (b)  (c) 

Figure 6.2 Pictures showing the impression of the sensor surface on the casting and thermocouple placement at casting surface.

Five castings were made using the same graphite mold. The position of thermocouple on the casting surface is shown in Table 6.3. The distance between the thermocouple tip and sensor center is approximately the same for all castings, the average distance being around 1cm. The following distances are shown in Table 6.3:

D_{st} - Distance from sensor center to the thermocouple bead,

X_{st} – Horizontal distance from sensor center to the thermocouple bead,

Y_{st} – Vertical distance from sensor center to the thermocouple bead, and

X_{et} - Distance from casting edge to the thermocouple bead.

Table 6.3 Position of thermocouple on the surface of the castings in the graphite mold.

Experiment	Id	Coating	D_{st} [cm]	X_{st} [cm]	Y_{st} [cm]	X_{et} [cm]
1	g_1	none	0.9	0.8	0.6	1.2
2	g_g2	dry graphite	1.0	1.0	0.2	1.1
3*	g_g3	dry graphite				
4	g_bn4	Boron Nitride	1.1	1.1	0.0	0.9
5	g_bn5	Boron Nitride	1.3	1.3	0.3	0.7

*Thermocouple placement is consistent with the other castings but was not measured.

6.3 EXPERIMENTAL RESULTS

The temperature and heat flux data acquired for each casting experiment are presented in this section. The sensor body is fabricated from an alloy. It is thus expected that there would be systematic measurement errors due to the different mold and sensor materials. The ratio between the sensor surface area to the mold face area, where the sensor was mounted, was 0.01. The sensor mass was 3.9g and the ratio between the sensor mass to the mold mass was 0.0088. Since the sensor surface is small enough compared to the mold surface, the temperature of the sensor thermocouple is assumed to be the surface mold temperature (T_M). The mold temperature is shown in Figure 6.3. The two parts of the mold were clamped manually. The data was acquired for approximately 180s since the onset of metal pouring. After the mold was opened, the part was ejected and the mold was held open for approximately 180 to 360s, allowing sufficient time for proper coating application. Thus, the time interval between consecutive castings was different for each case. For all cases, the mold temperature reaches a peak value of 250-270 ^{o}C at approximately 50-70 s.

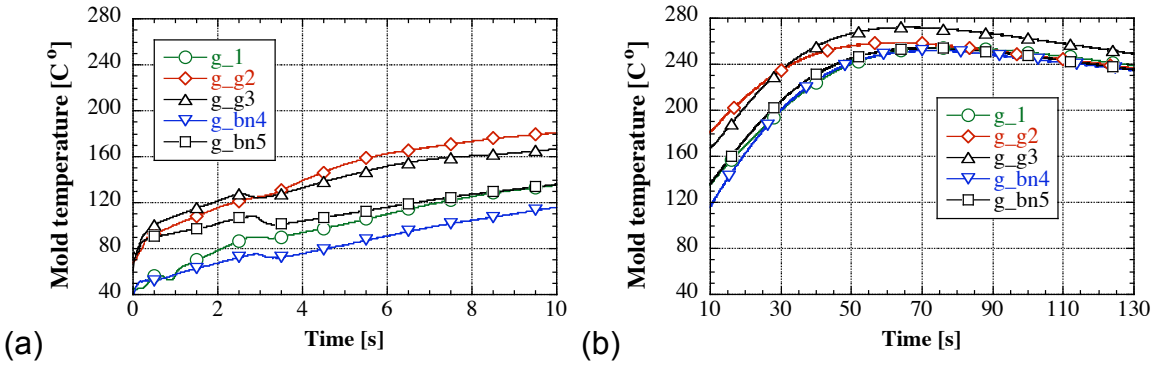

Figure 6.3 Temperature of the mold surface (a) t=0:10s and (b) t=10:130s.

The temperature of the thermocouple embedded at the metal surface is referred to as casting temperature at mold interface (T_C). T_C exhibits a variation similar to that expected for the A356 alloy (Figure 6.4). However, the cooling curves exhibit a eutectic

plateau at different temperatures. These eutectic temperature variations from different casting runs indicating that the temperature at thermocouple junction was different than that of the casting temperature.

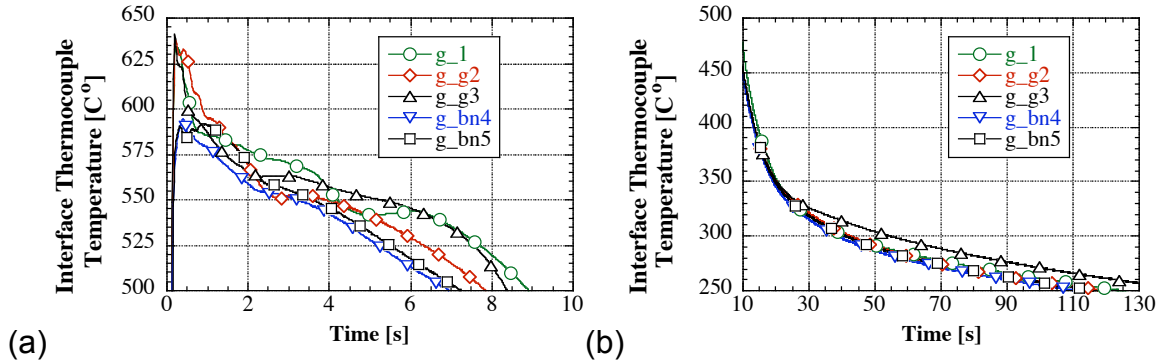

Figure 6.4 Thermocouple temperature at the casting surface (a) t=0:10s and (b) t=10:130s.

As seen in Figure 6.2, the thermocouple junction is not surrounded by liquid metal, being in contact with both the liquid metal and mold. Moreover, photographs indicate that the liquid metal did not wet either the thermocouple junction or the wires due to surface tension effects. For clarity, a sketch of the thermocouple position at the casting interface is depicted in Figure 6.5.

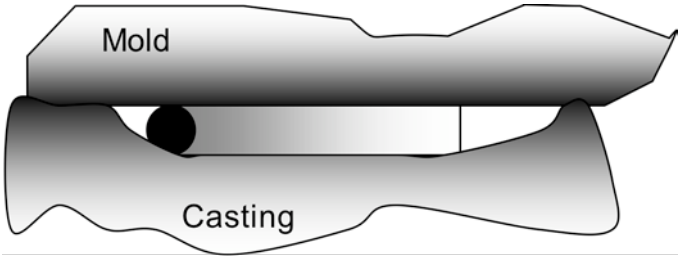

Figure 6.5 Sketch of the thermocouple bead position at casting interface.

Thus, due to incomplete contact of the thermocouple bead with the metal, the thermocouple will measure an average temperature between that of the mold and casting. Assuming that the temperature is proportional to the contact area, and neglecting the time response of the thermocouple, the bead temperature, T_b, is given by the following equation:

$$A_b T_b = A_c T_c + A_m T_m + A_a T_a, \tag{6.3}$$

where A_c, A_m, A_a are the bead areas in contact the casting, mold, and air. The bead area in contact with the thermocouple wires was included in the casting area, such that the total bead area is given as, $A_b = A_c + A_m + A_a$. Assuming that the air gap temperature depends linearly on the mold and casting temperature, the casting temperature can be determined using the following linear relationship:

$$T_c = \left[T_b - T_m(1-f)\right]/f \tag{6.4}$$

where f is an interpolation factor which needs to be determined for each case such that the eutectic plateau is at 555 °C. The factor f is shown in Table 6.4. The interpolation factor values for all cases indicate the casting temperature represents an overall

contribution of 93-96% to the thermocouple temperature. The method employed here for obtaining the actual casting surface temperature is the simplest and more accurate methods may have to be developed. There are two ways to improve the measurement of casting surface temperature: (1) use a more complex experimental setup than embedding one thermocouple at the casting surface, or (2) develop more accurate correlations for thermocouple junction temperature by taking into account the time response of the thermocouple bead, air conduction, and actual contact surfaces between the bead and air, casting, and mold.

Table 6.4 Temperature interpolation factor.

Case	g_1	g_g2	g_g3	g_bn4	g_bn5
f	0.93	0.947	0.973	0.96	0.96

The results for the computed temperature at the casting surface are shown in Figure 6.6. The results show that similar cooling curves were observed for the (g_g2, g_g3) cases, and (g_bn4, g_bn5), respectively. The first casting experiment, where no coating was used on the graphite mold, indicates a different evolution of surface temperature. This effect is likely due to a different filling pattern of the mold.

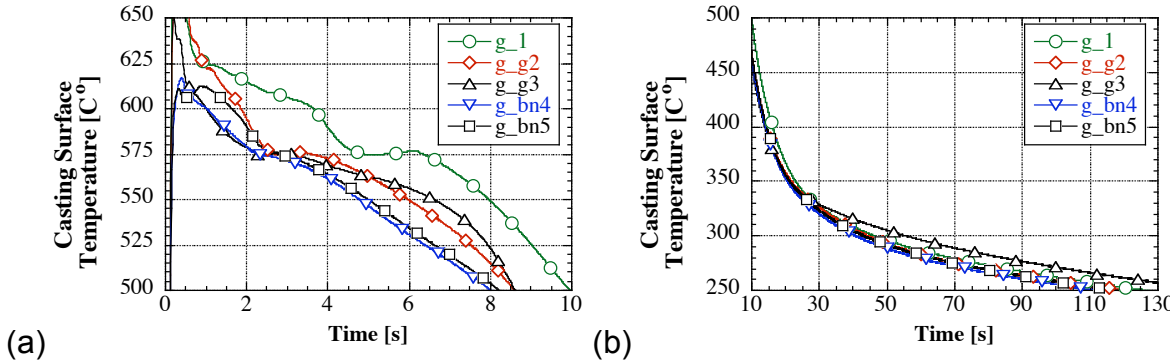

Figure 6.6 Computed temperature at the casting surface (a) t=0:10s and (b) t=10:130s.

The results for the measured heat flux are shown in Figure 6.7. The time origin is the instant at which the heat flux channel exhibits a sudden raise. Four distinct domains can be observed in the evolution of the heat flux. In the first domain, from t=0-2.5s, the heat flux exhibits either a plateau or small decrease at high values with average heat flux ranging from 1MW/m^2 to 2MW/m^2. In domain II, the heat flux drops sharply from a maximum value to a minimum value (Table 6.5). The time, t_{II}, is shown in Table 6.5 over which this sharp transition occurs. These results illustrate that similar heat flux evolutions were observed for the (g_g2, g_g3) cases, and (g_bn4, g_bn5), respectively. For the graphite coating cases (g_g2, g_g3), the heat flux transition to lower values was smoother, occurring over a larger time interval, in contrast to the BN coating cases. Domain III, is characterized by a plateau-like variation of the heat flux. For the graphite coating cases, the duration of this phase was approximately 2s, while for the BN coating it was approximately 4s, almost twice as large than for the graphite cases. Aside from case g_g2, the heat flux raises by a small amount at the end of domain III. As seen in Figure 6.7, the no-coating case, g_1, exhibited values between those for the graphite coating and BN coating cases. In domain IV, the heat flux decreases monotonically to an asymptotic value. The asymptotic value for the heat flux was 950; 1,100; 900; 800; and 900 W/m^2 for cases g_1, g_g2, g_g3, g_bn4, g_bn5, respectively.

Table 6.5 Maximum and minimum heat flux in domain II .

Case	g_1	g_g2	g_g3	g_bn4	g_bn5
HF1 [MW/m^2]	1.1	1.9	1.8	1.0	1.25
HF2 [MW/m^2]	0.6	1.2	1	0.36	0.36
t_{II} [s]	1.25	1.7	0.6	0.5	0.5

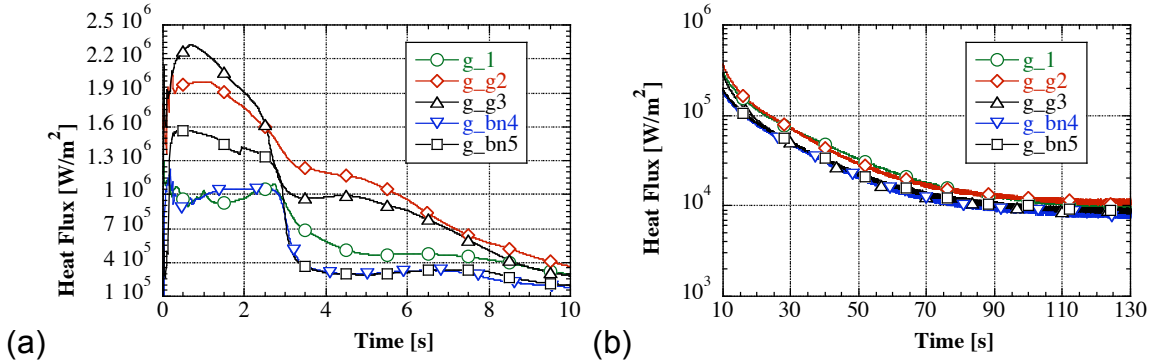

Figure 6.7 Measured heat flux through the casting-mold interface (a) t=0:10s and (b) t=10:130s.

6.3.1 Measurement Errors

In order to quantify uncertainties of the heat flux measurements, standard deviations were estimated from the acquired data and its corresponding average. For the sake of simplicity only the errors for the two measured temperatures and heat flux are given for the g_g3 case. The residual between the smoothed data and raw data was determined. For the three variables considered, the standard deviation was determined from a statistical analysis for the residual data. The standard deviation was noticeably different in the early and later stages. At the early stages, the standard deviation was 0.1and 0.05^{o}C, while at large times it was 0.2 and 0.1 ^{o}C for T_b and T_m, respectively. For the heat flux, the standard deviation was approximately 110 and 190 W/m^2 at the early and later stages, respectively. The smoothed heat flux data was denoted by h_s. The distribution of the residual, $h - h_s$, is shown in Figure 6.8 in percentage units. At times less than 10s, the residual values were less than 0.08%. The pct residual increased to about 4% at 130s. This increase is expected since the magnitude of the heat flux decreased while its standard deviation was almost the same.

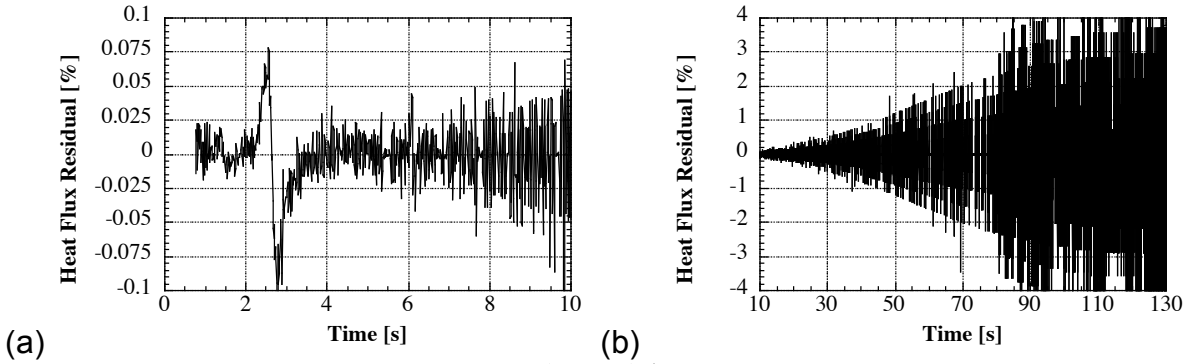

Figure 6.8 Residual for the heat flux, $(h - h_s)/h_s$ [%] (a) t=0:10s and (b) t=10:130s.

6.4 HEAT TRANSFER COEFFICIENT AT METAL-MOLD INTERFACE

The heat transfer coefficient, $h(q'',T_b,T_m)$, which was computed using the measured heat flux and the two temperatures measured, is plotted in Figure 6.9. As a matter of fact, it is possible to determine $h(q'',T_b,T_m)$ in real time, provided the data acquisition has the capability for mathematical manipulation of the scaled signals, such as in Lab View systems. The evolution of the heat transfer coefficient is similar to that of the heat flux, being characterized by four domains. Based on physical considerations, four distinct stages for the evolution of HTC were identified (Trovant and Argyropoulos, 2000) for aluminum alloy A356 castings in graphite molds. Their findings support the differentiation in four time domains observed in Figures 6.7 and 6.9 of this study for the evolution of q'' and HTC.

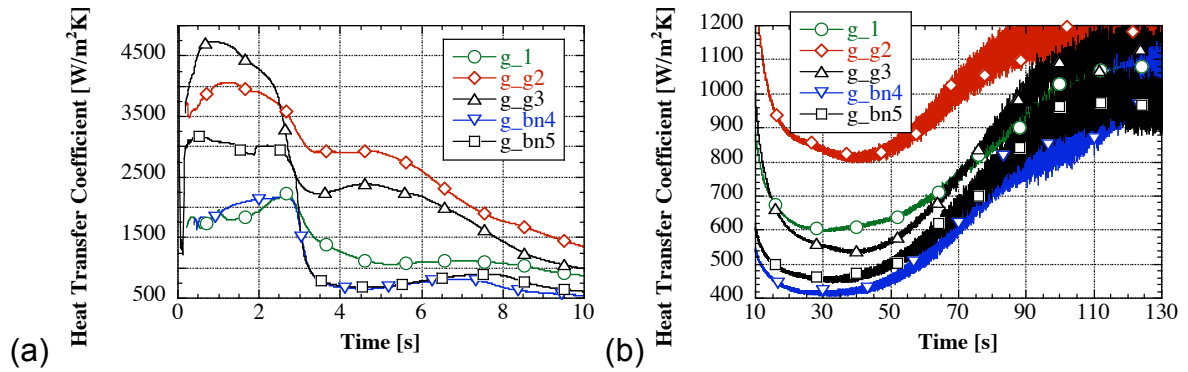

Figure 6.9 Computed heat transfer coefficient based on measured heat flux and two temperature data, $h(q'',T_b,T_m)$ for: (a) t=0:10s and (b) t=10:130s.

Next the HTC values and measurement errors are compared to those obtained in [8]. For all experiments, the maximum HTC had values between 1,800 to 4,700 W/m^{2}K, while the minimum valued ranged from 970 to 1,200 W/m^{2}K. For the HTC, the standard deviation was approximately 0.5 and 30 W/m^{2}K at the early stages and later stages of the experiments, respectively. In [8], HTC values were reported to reached a maximum of 1,700±200 W/m^{2}K and a minimum of 400±200 W/m^2. The HTC standard error is smaller for this study than that estimated from data reported, while the minimum values for HTC are in good agreement with those in Trovant and Argyropoulos (2000).

Additionally, the maximum values in this study are larger than those reported in Trovant and Argyropoulos (2000). Aside from the different geometrical configurations, another reason for these discrepancies could be due to the low frequency of 2Hz at which data was acquired in TA experiments. In addition, the HTC data was available in TA for times larger than approximately 2s since the onset of experiments, while the maximum HTC values reported in this study occurred within these initial stages.

The only difference between the variation of HTC and q'' was observed at large times, where two features were noticed. First, the HTC has a minimum at about 30-40s since the onset of pouring, increasing afterwards by an amount of approximately of 500 W/m^2. In order to rule out systematic errors due to temperature measurements, the HTC was computed using the surface casting temperature, T_c, rather than the measured casting temperature, T_b. The errors between $h(q'',T_b,T_m)$ and $h(q'',T_c,T_m)$ was determined to be approximately constant at 2.8% for the entire duration of the experiment. This increase in HTC could be due to the solidification characteristics in the mold used. For example, an increase in the HTC, from 80 W/m^2 at 35s to 200 W/m^2 at 80 s, was observed in Kim and Lee (1997), for aluminum alloy A356 cast into steel mold with a graphite coating. Another possible explanation of this HTC behavior is related to the use of a sensor material different than the mold material. Additional investigations are necessary to relate the effects of material property differences between the sensor and mold to the accuracy of the measured data. Second, HTC exhibits oscillations of increasing amplitude. As indicated for the heat flux data, the increase in HTC amplitude at longer times was due to the time variation of heat flux and temperature difference across the interface. In our case the measurement errors were constant, while variables used to obtain HTC, temperature difference, $T_b - T_m$, and heat flux, q'', decreased.

6.5 RECOMMENDATION FOR FUTURE WORK

The use of a sensor for the direct measurement of heat flux and surface temperature was successfully demonstrated for casting solidification. The heat flux data was used to obtain the heat transfer coefficient (HTC) at metal-mold interface. The HTC was determined very efficiently using a heat flux sensor and one additional thermocouple, avoiding cumbersome data post-processing and instrumentation arrangements. The variation of heat transfer coefficient agrees well with data from previous studies. Possible limitations of this direct method and measurement errors were also discussed.

6.6 REFERENCES

S. Engler, D. Boenisch, B. Kohler, “Metal and Mold Wall Movements During Solidification of Cast Iron”, AFS Cast Metals Research Journal, pp.20-30, (1973).

K. Ho, R.D. Pehlke, “Mechanisms of Heat Transfer at a Metal-Mold Interface”, *AFS Transactions*, v92, pp.587-598, (1984).

K. Ho, R.D. Pehlke, “Transient Methods for Determination of Metal-Mold Interfacial Heat Transfer”, *AFS Transactions*, v91, pp.689-698, (1983).

J.-C. Hwang, H.-T. Chuang, S.-H. Jong, W.-S. Hwang, “Measurement of Heat Transfer Coefficient at Metal/Mold Interface During Casting”, *AFS Transactions*, v102, pp.877-883, (1994).

T.-G. Kim and Z-H. Lee, “Time varying Heat Transfer Coefficients Between Tube-shaped Casting and Metal Mold”, *Int. J. Heat Mass Transfer*, v40, pp.3513-3525, (1997).

M. Krishnan and D.G.R. Sharma, Determination of the interfacial heat transfer coefficients h in unidirectional heat flow by Beck’s nonlinear estimation procedure. International Communications on Heat Mass Transfer, v.23, p.203, (1996).

Z.-H. Lee, T.-G Kim, Y.-S. Choi, “The Movement of the Concave Casting Surface during Mush-Type Solidification and Its Effect on the Heat-Transfer Coefficient”, *Metallurgical and Materials Transactions B*, v29B, pp.1051-1056, (1998).

A.S. Sabau and S. Viswanathan, "Temperature Measurements In Wax Patterns And Wax-Die Interfacial Heat Transfer Coefficients In Investment Casting," *AFS Trans.*, v111, paper 03-026, pp. 411-417, (2003).

C.A. Santos, J.M.V. Quaresma and A. Garcia, Determination of transient interfacial heat transfer coefficients in chill mold castings. *Journal of Alloys and Compounds*, v.319, n.1-2, p.174, (2001).

Souza, E.N.; Cheung, N.; Santos, C.A.; Garcia, A., “The Variation of the Metal/Mold Heat Transfer Coefficient along the Cross Section of Cylindrical Shaped Castings” In: Inverse Problems: Design and Optimization Symposium - IPDO, 2004, Rio de Janeiro.

M. Trovant and S. Argylopoulos, Finding boundary conditions: A coupling strategy for the modeling of metal casting process: part I. experimental study and correlation development. Metallurgical and Materials Transactions B, Vol. 31, pp. 75-86, 2000

SUBJECT INVENTIONS

No inventions were made or reported regarding this CRADA. The direct heat flux method, developed for this project, is ready for use in commercial environments. However, the measured data and the methods for data acquisition models developed in this program were shared with CRADA partners.

COMMERCIALIZATION POSSIBILITIES

The methods for data acquisition, which include the use of heat flux sensors, that were developed in this CRADA are well suited for application to commercial casting production. It is expected that the property data on lubricants obtained in this program will significantly enhance the design of structural safety-critical Mg alloy castings. In fact, the unit for the measurement of heat flux during lubricant applications was already manufactured to the ORNL specifications at Chem-Trend Inc.

PLANS FOR FUTURE COLLABORATION

Due to the success of this CRADA project, new projects on Mg are being developed with USCAR/USAMP, partners from this project and new parties.

CONCLUSIONS

This CRADA was very successful in reaching the goals envisioned. Lubricant spray experiments were conducted for various conditions that were never studied before. The data shown in this study validate the use of a sensor for the direct measurement of heat fluxes. The type of data obtained in this study can be used in the development of new lubricants and the selection of appropriate lubricant application techniques. The use of a sensor for the direct measurement of heat flux and surface temperature was demonstrated for casting solidification. The heat flux data was used to obtain the heat transfer coefficient at metal-mold interface. It was found that the heat transfer coefficient was determined very efficiently using a heat flux sensor and one additional thermocouple, avoiding cumbersome data post-processing and instrumentation arrangements. The direct heat flux method is ready for use in commercial environments.

ACKNOWLEDGEMENTS

This work was mainly conducted at the ORNL. Most of the work described in Chapter 5 was conducted at the University of Kentucky (UKY), Lexington. The project team members include the following:

- Ralph B. Dinwiddie, ORNL, infrared data aquisition.
- Mohamed I. Hassan, UKY, open die experiments,
- Ed C. Hatfield, ORNL, die lubricant experiments and casting experiments,

- Kazunori Kuwana, UKY, scale analysis and computer simulation of jet breakup, atomization model
- Adrian S. Sabau, ORNL, PI, die lubrication experiments, data acquisition, and measurement of heat fluxes at metal-mold interfaces, experiment design of open-die configurations, Free-surface flows,
- Kozo Saito, UKY, UKY-PI, scale analysis,
- Valerio Viti, UKY, computer simulation of jet break-up.

The authors would like to thank Dick Osborne, Don Penrod, Bruce Cox, and Naiyi Li for their efforts to coordinate the efforts at multiple sites, organize visits at participating companies, and disseminate the knowledge from this project to participating companies.

This work was performed under a Cooperative Research and Development Agreement (CRADA) with the United States Advanced Materials Partnership (USAMP), United States Council for Automotive Research (USCAR) for the project on Structural Cast Magnesium Development. This research was sponsored by the U.S. Department of Energy, Assistant Secretary for Energy Efficiency and Renewable Energy, Office of Transportation Technologies, Lightweight Vehicle Materials Program, under contract DE-AC05-00OR22725 with UT-Battelle, LLC. The authors acknowledge that this research was supported in whole by Department of Energy Cooperative Agreement No. DE-FC05-02OR22910. Such support does not constitute an endorsement by the Department of Energy of the views expressed herein. The authors would also like to thank Srinath Viswanathan, University of Alabama, Tuscaloosa, AL with whom we collaborated on past projects, and Anoop Samant, University of Tennessee, Knoxville, TN for his assistance in preparing the final report.

INTERNAL DISTRIBUTION

1. S. J. Zinkle
2. R. B. Dinwiddie
3. E. C. Hatfield
4. W. D. Porter
5. T. M. Rosseel
6-7. A. S. Sabau
8. C. A. Blue
9. P. S. Sklad
10. P. J. Wenzel
11. ORNL Technology Transfer Office, 4500N, 6196
12. Office of Technical Information and Classification, 4500N, 6254

EXTERNAL DISTRIBUTION

13. DOE/ORO, 4500N, 6269
14. R. J. Osborne, General Motors Corporation, 30001 Van Dyke Road, Warren, MI 48090-9020.
15. D. E. Penrod, Manufacturing Services and Development, Inc., 4665 Arlington Drive, Cape Haze, FL 33946.
16. R. Wrobleski, USAMP, 1000 Town Center, Suite 300, Southfield, MI 48075.
17. DOE/Work for Others, MS G209
18. K. Saito, Department of Mechanical Engineering, 151 Ralph G. Anderson Building, University of Kentucky, Lexington, KY 40506
19. K. Kuwana, Department of Mechanical Engineering, 151 Ralph G. Anderson Building, University of Kentucky, Lexington, KY 40506
20. M.I. Hassan, Department of Mechanical Engineering, 151 Ralph G. Anderson Building, University of Kentucky, Lexington, KY 40506
21. B. M. Cox, Daimler-Chrysler Co., 800 Chrysler Drive, Auburn Hills, MI 48326-2757

Final Report Certification
for
CRADA Number 0596

Between

UT-Battelle, LLC

and

USAMP
(Participant)

Instructions:

Mark the appropriate statement in 1a or 1b below with an 'IX." Refer to the articles in the CRADA terms and conditions governing the identification and marking of Protected CRADA Information (PCI).

If no PCI is identified, the report will be distributed without restriction. If PCI is identified, the report distribution will be limited in accordance with the CRADA terms and conditions governing release of data. In all cases items 2 and 3 must be true. That is, the report cannot contain Proprietary Information and a disclosure must be filed prior to release of the report.

This certification may either be made by using this form or may be made on company letterhead if the Participant desires. A faxed copy of this completed form is acceptable.

The following certification is made for the subject final report:

1. (a) ☐ The final report contains information that qualifies as "Protected CRADA Information" (PCI). The PCI legend is printed on the report cover, and the PCI is clearly identified.

OR

(b) ☒ The final report does not contain "Protected CRADA Information." The "Approved for Public Release" legend is printed on the report cover.

2. The final report does not contain Proprietary Information.

3. By the signature below, the Participant has no objection to the public distribution of the final report due to patentable information.

For the Participant:

Richard J. Osborne
(Name)

GM-Staff Dev. Engineer
(Title)

10-11-07
(Date)